

TENSILE PROPERTIES AND WORK HARDENING BEHAVIOUR OF BORON ADDED P91 STEEL

By

D PRASADARAO PALAPARTI

Enrollment No: ENGG02201505017

Indira Gandhi Centre for Atomic Research, Kalpakkam, India

A dissertation submitted to the

Board of Studies in Engineering Sciences

In the partial fulfillment of requirements

For the degree of

MASTER OF SCIENCE (ENGINEERING)

Of

HOMI BHABHA NATIONAL INSTITUTE



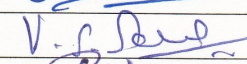
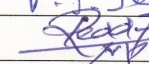
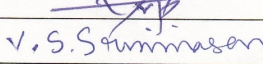
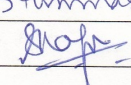


JULY 2019

Homi Bhabha National Institute

Recommendations of the Thesis Examining Committee

As members of the Thesis examining Committee, we recommend that the thesis prepared by Mr. **D PRASADARAO PALAPARTI** entitled **TENSILE PROPERTIES AND WORK HARDENING BEHAVIOUR OF BORON ADDED P91 STEEL** be accepted as fulfilling the thesis requirement for the Degree of Master of Science (Engineering).

Thesis Committee	Name	Signature
Mamber-1	Dr. Arup Dasgupta	
Member-2	Dr. Nagesha	
Member-3	Prof. V.S. Sharma-IITM	
Co-guide	Dr. G.V. Prasad Reddy	
Guide/Convener	Dr. V.S. Srinivasan	
Chairman	Dr. Shaju K. Albert	

Final approval and acceptance of this thesis is contingent upon the candidate's submission of the final copies of the thesis to HBNI.

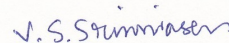
I/We hereby certify that I/we have read this thesis prepared under my/our direction and recommend that it may be accepted as fulfilling the thesis requirement.

Date:

Place: KALPAKKAM



Co-guide (if applicable)



Guide

DECLARATION

I, hereby declare that the investigation presented in the thesis has been carried out by me. The work is original and has not been submitted earlier as a whole or in part for a degree / diploma at this or any other Institution / University.



D PRASADARAO PALAPARTI

Version approved during the meeting of Standing Committee of Deans held during 29-30 Nov 2013

LIST OF PUBLICATIONS

Tensile flow and work hardening behaviour of Boron added P91 steel,

D.P. Rao Palaparti, J. Christopher, M. Nandagopal, G.V. Prasad Reddy, V.S. Srinivasan and B.K. Choudhary, Proceedings of ICONS2018, Dec 14–17 IIT, Chennai.

DEDICATION

I dedicate this work to Almighty God, who gave Life, Strength, Wisdom and Knowledge.

To my beloved parents **Shri. P. Nagendram (Late)** and **Smt. P. Venkata Ratnam**, who gave spirit, inspiration and scarified their lives towards my happiness, education and growth,

To my dearest wife **Gowri**, lovely son **Rahul**, and little daughter **Yamini**, for their unconditional love, affection and continuous support to fulfill my carrier achievements.

ACKNOWLEDGEMENTS

I take this opportunity to express my sincere gratitude to my guide, Dr. V.S. Srinivasan, Head, LIMS/ SIRD, and Co-guide Dr. G.V. Prasad Reddy, Head, Creep Studies Section (CSS), who gave an opportunity, encouragement and inspiration to take up this project for my M.Sc., degree under their esteemed supervision, and also would like to express my sincere thanks to my previous guide Dr. B.K. Choudhary, Head, Deformation and Damage Modeling Section, who have encouraged me to initiate this work.

I am very thankful to my Doctoral Committee Chairman, Dr. Shaju K. Albert, Director, MMG & MSG, and DC members Dr. Arup Dasgupta, Head, Structural and Analytical Microscopy Section (SAMS), Dr. Nagesha, Head, Fatigue Studies Section (FSS), Dr. Subramaniya Sharma, Professor, IIT Madras, for their continuous support and evaluation of my progress pertaining to this work and extended their valuable suggestions, feedbacks and encouragement throughout this project to accomplish successfully.

I express my sincere thanks to Dr. Anish Kumar, Head, UMS/NDED and Dean, Engineering Sciences HBNI, Dr. Lakshmi Narsimhan, Convener of HBNI (Engineering Sciences) Dr. Vidya Sundararajan, Head, SPHRDD, and Dr. Madurai Meenachi Head BARC Training School IGCAR campus and their Staff, for their constant academic support and encouragement.

I am extremely thankful to my colleagues, Dr. Isaac Samuel, Dr. J. Christopher, Dr. G. Sainath, and Research Scholars, HBNI IGCAR, Mr. C. Praveen, Mr. Rohith, Mr. V. Shiva, Mr. T. Suresh Kumar for their encouragement and support during the course of this work. Special thanks to my family members for their unconditional love, support and encouragement to the accomplishment of this project.

Last but not the least; I extend special thanks to all my colleagues friends and well-wishers in Material Development and Technology Division (MDTD) for their moral support throughout this project work.

D PRASADARAO PALAPARTI

Version approved during the meeting of Standing Committee of Deans held during 29-30 Nov 2013

CONTENTS

CONTENTS	v
SYNOPSIS	vii
LIST OF FIGURES	xii
LIST OF TABLES	xvi
NOMENCLATURE	xvii
LIST OF PUBLICATIONS	xviii
Chapter 1 : INTRODUCTION	1
1.0 Material	1
1.1 Steam Generator—A critical component for PFBR	3
1.2 Selection of Structural Materials for Steam Generators	3
1.3 Ferritic Steels—An inevitable choice of structural material	5
1.4 Outline of project thesis	6
Chapter 2 : LITERATURE REVIEW	7
2.0 Introduction	7
2.1 Ferritic steels	7
2.1.1 Evolution of 9% Chromium steels	8
2.1.1.1 $2\frac{1}{4}Cr-1Mo$ Steel (Grade 22)	9
2.1.1.2 9Cr-1Mo Steel (P9)	11
2.1.1.3 Modified 9Cr-1Mo Steel (P91)	12
2.1.1.4 Boron added P91 Steel (P91B)	13
2.1.1.5 9Cr-0.5Mo-1.8W-V-Nb Steel (P92)	14
2.2 Tensile deformation behaviour of engineering materials	15
2.2.1 Classification of stress-strain curves	15
2.2.1.1 Elastic response: Type-I	16
2.2.1.2 Elastic—Homogenous Plastic response: Type-II	18
2.2.1.3 Elastic—Heterogeneous Plastic response: Type-III	21
2.2.1.4 Elastic—Heterogeneous Plastic— Homogeneous Plastic response: Type-IV	22
2.2.1.5 Elastic—Heterogeneous Plastic—Homogeneous Plastic response: Type-V	22
2.2.2 Engineering stress-strain curve	23
2.2.3 True stress—true strain curve	24
2.2.4 Instability in tension	26
2.2.5 Effect of strain rate on tensile properties	27
2.2.6 Effect of temperature on tensile flow properties	29
2.2.7 Tensile fractures	30
2.2.8 Dynamic strain ageing (DSA)	32
2.2.9 Strain or Work hardening behaviour	34
2.2.10 Tensile constitutive material modeling	35
2.3 Analytical Frame work	38
2.4 Motivation of the study	42

Chapter 3 : EXPERIMENTAL DETAILS	43
3.0 Material Composition and Heat Treatment.....	43
3.1 Tensile specimen geometry and test conditions	43
3.2 Tensile testing equipment	44
3.3 Metallographic examination.....	45
3.4 Sample preparation for optical microscopic studies.....	45
3.5 Sample preparation for scanning electron microscopic (SEM) studies.....	46
Chapter 4 : RESULTS AND DISCUSSION	47
4.0 Introduction	47
4.1 Tensile true stress and true plastic strain behaviour	48
4.2 Variations of tensile properties with temperature and strain rate.....	50
4.3 Modeling tensile flow behaviour of boron added P91 steel.....	54
4.4 Variations of Ludwigson parameters with temperature and strain rate.....	56
4.5 Variations of Voce and Kocks–Mecking parameters with temperature and strain rate	61
4.6 Activation energy measurement for dynamic recovery.....	69
4.7 Comparison of work hardening parameters obtained using K–M approach and Voce equation.....	72
4.8 Influence of temperature and strain rate on the variations of instantaneous work hardening rate with stress.....	75
4.9 Fracture surface examination of boron added P91 steel.....	79
Chapter 5 : COMPARISON OF BORON ADDED P91 AND GRADE P91 STEELS.....	83
5.1 Introduction.....	83
5.2 Microstructure of boron added P91 steel and Grade P91 steel.....	84
5.3 Mechanical properties	86
5.4 Ludwigson derived work hardening parameters	88
5.5 Voce derived work hardening parameters	89
Chapter 6 : CONCLUSIONS AND FUTURE WORK.....	92
6.1 Conclusions	92
6.2 Future work	83
REFERENCES	94

LIST OF FIGURES

CHAPTER-1

Fig. 1.1: A schematic diagram of Prototype Fast Breeder Reactor (PFBR).....	2
Fig. 1.2: A schematic representation of PFBR Steam Generator component.....	4

CHAPTER-2

Fig. 2.1: Evolution of ferritic steels as a function of allowable stress for 10^5 hr creep rupture life at 600 °C.....	9
Fig. 2.2: Schematic representation of non-uniform precipitation states in tempered martensitic 9-12% Chromium steels.....	13
Fig. 2.3: Type-I stress-strain behaviour revealing completely elastic response	16
Fig. 2.4: Type-II stress-strain behaviour exhibits elastic behaviour followed by a region of homogenous plastic deformation	18
Fig. 2.5: Comparison of stress-strain curves for high and low toughness materials	20
Fig. 2.6: Type-III stress-strain behaviour reflecting elastic behaviour followed by heterogeneous plastic flow.....	21
Fig. 2.7: Type-IV stress-strain curve shows a narrow heterogeneous deformation regime between initial elastic and final homogeneous flow regimes	22
Fig. 2.8: Type-V stress-strain behaviour usually found in crystalline polymers.....	22
Fig. 2.9: The engineering stress-strain curve	23
Fig. 2.10: Graphical representation of necking criteria.....	27
Fig. 2.11: Considere's construction for the determination of the point of maximum load	27
Fig. 2.12: Variation of yield stress as a function of applied strain rate.....	28
Fig. 2.13: Changes in stress-strain curve with temperature	29
Fig. 2.14: Appearance of (a) ductile and (b) brittle tensile fractures	31
Fig. 2.15: Typical cup-cone fracture appearance of un-notched tensile specimen	31
Fig. 2.16: A schematic representation of shear lip zone, top and side view.....	31
Fig. 2.17: Types of serrations observed during tensile deformation.....	31
Fig. 2.18: Graphical representation of Hollomon equation at $\epsilon=1$	33
Fig. 2.19: Graphical representation of Ludwik equation at $\epsilon=1$	35

Fig. 2.20: Graphical representation of Swift equation at $\epsilon=1$	36
Fig. 2.21: Graphical representation of Ludwigson equation at $\epsilon=1$	37
Fig. 2.22: Graphical representation of Voce equation at $\epsilon=1$	37
Fig. 2.23: Schematic representation of variation of work hardening rate with normalised shear stress shows various stages of work hardening in single crystal and poly crystals. The dotted line represents the stage-III hardening obeying K-M approach. $\theta_{0,K-M}$ is obtained as $\theta = \theta_{0,K-M}$ at $\sigma=0$	42

CHAPTER-3

Fig. 3.1: The Geometry of tensile specimen (all dimensions are in mm).....	44
Fig. 3.2: (a) Hung ta-2402 tensile machine and (b) schematic representation of different parts of screw driven tensile machine.....	44 & 45

CHAPTER-4

Fig. 4.1: True stress (σ)–true plastic strain behaviour of boron added P91 steel at the strain rates of (a) $2.16 \times 10^{-3} \text{ s}^{-1}$ (b) $3.16 \times 10^{-4} \text{ s}^{-1}$ (c) $3.16 \times 10^{-5} \text{ s}^{-1}$ and (d) effect of strain rate on true stress–strain behaviour.....	48
Fig. 4.2: Engineering–stress and Engineering–strain curve of boron added P91 steel at the strain rate of $3.16 \times 10^{-5} \text{ s}^{-1}$ shows different types of serrations.....	50
Fig. 4.3: The variations of (a) yield strength and (b) ultimate tensile strength with temperature for all strain rates of boron added P91 steel.....	51
Fig. 4.4: The variations of (a) percentage elongation to fracture and (b) percentage reduction in area with temperature for all strain rates of boron added P91 steel.....	52
Fig. 4.5: The validation of (a) yield strength and (b) ultimate tensile strength values of boron added P91 steel data with average values of RCC–MR French design data and NIMS design data reported for P91 steel.....	53
Fig. 4.6: True stress–true plastic strain data at temperature 300 K obeyed by (a) Ludwigson and (b) Voce with equal confidence for all strain rates of boron added P91 steel.....	54
Fig. 4.7: The variations of (a) strain hardening exponent (n_1) and (b) normalised strain hardening co-efficient (K_1/μ) with temperature for all strain rates of boron added P91 steel.....	55
Fig. 4.8: The variations of (a) n_2 and (b) $\exp(K_2)$ with temperature for different strain rates of boron added P91 steel.....	57
Fig. 4.9: The variations of (a) transition strain (ϵ_L) and (b) stress (σ_L) with temperature for different strain rates in boron added P91 steel.....	57

- Fig. 4.10:** The variations of (a) normalised initial stress (σ_i/μ), (b) normalised saturation stress (σ_s/μ) and (c) n_V parameter with temperature for different strain rates in boron added P91 steel.....60
- Fig. 4.11:** The variations of (a) normalised saturation stress ($\sigma_{s, K-M}/\mu$), (b) normalised work hardening rate ($\theta_{0, K-M}/\mu$), (c) $n_{V, K-M}$ parameters obtained by K–M concept for boron added P91 steel and (d) K–M Concept has been shown in terms of θ – σ plot63 & 64
- Fig. 4.12:** The variation of dynamic recovery parameter (n_v) with temperature for boron added P91 steel at different strain rates (a) $1.26 \times 10^{-3} \text{ s}^{-1}$ (b) $3.16 \times 10^{-4} \text{ s}^{-1}$ (c) $3.16 \times 10^{-5} \text{ s}^{-1}$ (d) Applicability of Bergström and Hallén model for all strain rates (Symbols: Experimental data, Solid lines: Predicted values)69
- Fig. 4.13:** The variation of true uniform plastic strain with dynamic recovery parameter for all strain rates of boron added P91 steel.....69
- Fig. 4.14:** Comparison of initial work hardening rates evaluated using K–M approach ($\theta_{0, K-M}$) and derivative form of Voce equation ($\theta_{0, Voce}$) at different temperatures and heat treatment conditions in boron added P91 steel. Theoretical $\theta_{0, K-M} = \theta_{0, Voce}$ line is shown as solid line.....69
- Fig. 4.15:** Comparison of saturation stresses evaluated using K–M approach ($\sigma_{s, K-M}$) and Voce equation ($\sigma_{s, Voce}$) at different temperatures and heat treatment conditions in boron added P91 steel. Theoretical $\sigma_{s, K-M} = \sigma_{s, Voce}$ line is shown as a solid line.....70
- Fig. 4.16:** Comparison of rate parameter n_V evaluated using K–M approach ($n_{V, K-M}$) and Voce equation ($n_{V, Voce}$) at different temperatures and heat treatment conditions in boron added P91 steel. Theoretical $n_{V, K-M} = n_{V, Voce}$ line is shown as a solid line.....71
- Fig. 4.17:** The variation of (a) θ vs. σ and (b) $\theta\sigma$ vs. σ for all test temperatures at the strain rate of $1.26 \times 10^{-3} \text{ s}^{-1}$ for boron added P91 steel.....73
- Fig. 4.18:** The variation of θ vs. σ and $\theta\sigma$ vs. σ at 300 K at all strain rates for boron added P91 steel.....73
- Fig. 4.19:** The variation of θ vs. σ at 873 K at all strain rates for boron added P91 steel.....74
- Fig. 4.20:** The variation of instantaneous work hardening rate parameter (θ) with true stress (σ) at selected temperatures of 300, 473, 723, and 873 K at all the strain rates for boron added P91 steel.....75
- Fig. 4.21:** The variation of normalised stress to onset of stage–III with temperature at all the strain rates for boron added P91 steel.....75
- Fig. 4.22:** Fracture surface images of tensile tested boron added P91 steel at 300 K.....77

Fig. 4.23: Fracture surface images of tensile tested boron added P91 steel at 573 K.....	78
Fig. 4.24: Fracture surface images of tensile tested boron added P91 steel at 623 K.....	78
Fig. 4.25: Fracture surface images of tensile tested boron added P91 steel at 873 K.....	78

CHAPTER-5

Fig. 5.1: Composition diagram for boron and nitrogen showing formation of solid solution or boron nitride (BN) at a normalizing temperature of 1323–1423 K.....	84
Fig. 5.2: Microstructure of (a) P91 steel and (b) boron added P91 steel in normalized and tempered condition.....	80
Fig. 5.3: The variations of (a) yield strength and (b) ultimate tensile strength with temperature for boron added P91 steel and P91 steel.....	81
Fig. 5.4: The variations of (a) percentage elongation and (b) percentage reduction in area (c) post necking strain with temperature for both the steels. Fractographic images of (d) P91 steel and (e) boron added P91 steel at 773 K.....	81
Fig. 5.5: The variations of Ludwigson parameters (a) K_1 (b) n_1 (c) K_2 and (d) n_2 with temperature for both boron added P91 steel and P91 steel.....	83
Fig. 5.6: The variations of Voce parameters (a) Initial stress (σ_i) (b) Saturation stress (σ_s) and (c) n_v with temperature for both boron added P91 steel and P91 steel.....	85 & 86
Fig. 5.7: The variations of true uniform plastic with temperature for both boron added P91 steel and P91 steel at the strain rate $1.26 \times 10^{-3} \text{ s}^{-1}$	85 & 86

SYNOPSIS

Boron added P91 steel (P91B) is considered to be futuristic candidate structural material for Commercial Liquid Metal Fast Breeder Reactor (CLMFBR) Steam Generator (SG) applications. Boron is an important interstitial element, having extremely low solubility in α -solid solution ($<0.003\%$). In general, boron addition to heat treatable low carbon steels improves its hardenability, strength and subsequently make the steels less susceptible to quench cracking and distortion during conventional as well as post heat treatment conditions. The beneficial effect of boron addition to the 9% Cr steels is to reduce the coarsening kinetics of $M_{23}C_6$ carbides by enrichment of boron in carbides. This in turn is reported to improve the creep rupture properties and type-IV crack resistance in weld-joints.

Tensile stress-strain and work hardening analysis for engineering materials attract continued scientific and technological interest in understanding deformation and work hardening behaviour of materials for high temperature applications in order to ensure the safe performance of material in working environment. In the present investigation, tensile flow and work hardening behaviour of boron added P91 steel is examined in normalized and tempered condition. Tensile tests were carried out at different temperatures ranging from 300 to 873 K employing three different strain rates of 1.26×10^{-3} , 3.16×10^{-4} and $3.16 \times 10^{-5} \text{ s}^{-1}$. The microstructure and fracture surface examination were carried out by using Optical and Scanning Electron Microscopy (SEM) for all tested samples. The microstructure of as-received samples consists of transformed tempered lath martensite with high dislocation density along with distribution of fine precipitates on lath, packet and prior austenite grain boundaries. The fracture surface of tensile tested specimens showed typical cup and cone fracture with significant shear lip in peripheral region followed by appearance of fibrous surface fracture at the center of the fractured specimens. The width of the shear lip and the size of central fibrous area decreased with increase the test temperature. The overall fracture

appearance showed ductile fracture from surface followed by brittle fibrous nature at the center of samples.

The variation of true stress and true plastic strain behaviour as function of temperature and strain rate was discussed. It was observed that the true stress and true plastic strain decreased with increase in temperature. The decrease in stress and strain values is nominal at room (300 K) temperature and more rapid at high temperature (698–873 K). At intermediate temperature regime (473–698 K) the variations in true stress–strain behaviour is insignificant and data has been appeared to be a narrow band. The variation of shear modulus normalized yield strength and ultimate tensile strength with temperature exhibited a decrease in strength with increase the temperature. The decrease in strength is gradual between 300–473 K, followed by peaks/plateau at intermediate temperature (473–698 K), and sudden decrease at high temperature (698–873 K) for all the strain rates. Strain rate dependence yield and ultimate strengths revealed insignificant influence at room temperature (300 K). However, with decrease in strain rate, strength was varied at intermediate temperature regime followed by rapid decrease at high temperature regime. The variation of percentage total elongation with temperature showed gradual decrease from 300 to 473 K, followed by ductility minima at 473–698 K, and rapid increase at high temperatures (723–873 K). The influence of strain rate on percentage total elongation was totally insignificant for all temperature and strain rate conditions. The variation in percentage reduction in area with temperature exhibited insignificant variations at room (300 K), followed by appearance of peaks/plateau at intermediate temperature regime (473–698 K) and rapid increase at temperature regime (723–873 K). The strength parameters such as yield and ultimate tensile strength related to boron added P91 steel was compared with international test data such as, NIMS, and French design code RCC–MR average data. The boron added P91 steel data exhibited reasonably better yield and ultimate tensile strengths than the NIMS and French design code RCC–MR average data.

Constitutive material modeling is carried out on experimental stress–strain data for understanding the tensile deformation and work hardening behaviour of boron added P91 steel by using various tensile flow relationships. The Ludwigson and Voce equations were exclusively used for this study to describe the true stress–true plastic strain data for all test conditions. The variation of experimental true stress as a function of true plastic strain at different temperature and strain rates exhibited a decrease in true stress with increase in temperature from 300 to 473 K, followed by a marginal decrease in the intermediate temperature regime (473–698 K). Further at this temperature range the flow stress data appeared in the form of band of narrow region. At high temperatures a rapid decrease in flow stress is observed. It is also clearly indicated that the level of true plastic strain that the specimens can be deformed uniformly, decreased with increase in temperature. Uniform plastic strain also decreased from temperature 300 to 473 K followed by a marginal decrease at intermediate regime (473–698 K) and a rapid decrease at high temperatures (>698 K). All these observations strongly indicated that the variation of true stress with true plastic strain demonstrated three distinct temperature regimes of room, intermediate and high. At room and intermediate temperatures, the experimental data exhibited curvilinear behaviour and nearly linear behaviour at high strain and temperatures. The experimental true stress–true plastic strain data was fitted with tensile flow relationships proposed by Ludwigson and Voce using Levenberg–Marquardt (L–M) algorithm with unknown constants as adjustable parameters. The goodness of fit was evaluated using lower χ^2 value, i.e., the sum of square of the deviations of the calculated stress values from the experimental stress values obtained for these relationships at different strain rate and temperature conditions. The variations of instantaneous work hardening rate (θ) with true stress (σ) displayed two stage behaviour characterized by initial transition stage (stage–I) followed by stage–III. The θ – σ plots exhibited rapid decrease of stress in transition stage (stage–I) and gradual decrease in stage–III regime. The stress to onset of stage–III, which is determined as a stress for the transition from stage–I to stage–III, when plotted as a function of temperature, exhibited gradual

decrease from room to intermediate followed by rapid decrease at high temperature. The variations of Ludwigson derived work hardening parameters (K_1 , n_1 , K_2 , n_2) with temperature exhibited a gradual decrease from room temperature followed by peaks/plateau at intermediate and rapid decrease at high temperatures. The description of true stress and true plastic strain data by using Voce equation that usually results in improved predictions is another attractive flow relationship. Voce equation has provided significant attention in view of sound interpretation proposed by the Kocks–Mecking.

In this investigation, a detailed analysis has also been performed to study the work hardening behaviour of boron added P91 steel in the framework of Kocks–Mecking approach and subsequently studied the equivalence between Kocks–Mecking and Voce relationships. Analysis indicated that flow behaviour of boron added P91 steel can be adequately described by both Voce and Kocks–Mecking approaches at all the test conditions. The parameters associated with both approaches displayed three distinct temperature regimes as gradual variations from 300 to 473 K followed by peaks/plateaus at intermediate temperature and rapid variations at high temperature. The observed narrow band regions in true stress–true strain data and θ vs. σ , $\theta\sigma$ vs. σ behaviour, peaks/plateau, ductility minima, and negative strain rate sensitivity in tensile properties, work hardening parameters pertaining to Ludwigson, Voce, and Kocks–Mecking ascribed to anomalous behaviour. The observed anomalous variation in flow behaviour at intermediate temperature is attributed to the occurrence of dynamic strain ageing (DSA). The dynamic strain ageing causes an increased rate of dislocation multiplication and delay in recovery of dislocation structure due to reduced propensity to cross–slip leading to uniform distribution of dislocations or poorly defined cell structure.

The activation energy for dynamic recovery is calculated using model proposed by Bergström and Hallén. The dynamic recovery is governed by cross–slip of screw dislocations at low and intermediate temperature, and dislocation climb dominates over cross–slip mechanism at

high temperatures. The average values of activation energy for cross-slip mechanism at room and intermediate temperature as $Q_c = 3.61 \text{ kJ mol}^{-1}$ ($37.5 \times 10^{-3} \text{ eV/atom}$) and for climb mechanism at high temperature as $Q_m = 182.4 \text{ kJ mol}^{-1}$ have been obtained. It can also be observed that the temperature at which transition take place from cross-slip dominated deformation to climb controlled deformation decreased with decrease in the strain rate. The comparison of respective work hardening parameters obtained using K-M approach and Voce equation indicated attractive equivalence between the two approaches for boron added P91 steel. Finally, in order to demonstrate the role of boron and its influence on mechanical properties and work hardening behaviour after alloying to plain P91 steel, a comparative results of tensile and work hardening parameters of boron added P91 steel and P91 steel have been presented for further scope of understanding.

Chapter 1 : INTRODUCTION

1.0 Material

Boron added P91 steel designated as **P91B** is considered as a candidate structural material for steam generator applications for Future Indian Sodium Cooled Fast Reactors and Generation IV Liquid Metal Fast Breeder Reactors (LMFBRs) [1]. Boron added P91 steel is developed by adding nominal amount of 100 ppm boron to Mod.9Cr–1Mo or P91 steel for improving high temperature mechanical properties, specially to minimize the high tendency of typical Type–IV cracking in weldments of the steel. Mod.9Cr–1Mo or P91 steel is an improved version of plain 9Cr–1Mo (**P9**) steel by adding strong carbide/nitride forming elements like **vanadium** and **niobium** along with controlled addition of **nitrogen** to achieve desired high temperature creep strength properties. It is to be noted that hereafter in this text the Mod.9Cr–1Mo steel will be mentioned P91 steel. It is important to note that the P91 steel is considered as the candidate structural material for steam generator (SG) applications in Prototype Fast Breeder Reactor (PFBR) for all its components like tubes, shell and thick section tube plates [2]. The schematic diagram of PFBR is shown in Fig 1.1. The schematic diagram showed some important components such as reactor, steam generator and turbine systems. The main criteria for selecting P91 steel for steam generator applications is based on its excellent low thermal expansion co-efficient and high resistance to stress corrosion cracking in water–steam systems as compared to austenitic stainless steels and possess better mechanical properties at elevated temperatures than the previous versions of $2^{1/4}\text{Cr}–1\text{Mo}$ and 9Cr–1Mo steels [2]. However, though P91 steel has more favorable aspects as mentioned above, subsequently it also has poor resistance to Type–VI cracking during high temperature creep deformation of weldments considered as significant detrimental aspect for this steel. Type–IV cracking is a specific damage phenomenon generally occurs in ferritic–martensitic steels during creep deformation in heat affected zone (HAZ) of its weldments. Extensive studies

have been carried out to find the exact root cause of this failure and subsequently different alloys have been developed by adding appropriate alloying elements to overcome this problem. Recent studies have proved that **boron** is considered as a best alloying element, makes the steel for high resistance to Type-IV cracking failures in ferritic–martensitic steels [3]. Boron is an interstitial alloying element with minute solubility in α -solid solution ($<0.003\%$), increases hardenability and strength of low carbon heat treatable steels. It is also observed that steels containing reasonable amount of boron showed less susceptibility to quench cracking and distortion during conventional as well as post-weld heat treatment conditions [4]. The main advantage of boron addition to P91 steel is to reduce the coarsening rate of beneficial $M_{23}C_6$ carbides by enriching the boron in carbides, thus improves the creep rupture strength and Type-IV crack resistance in weld-joints [5].

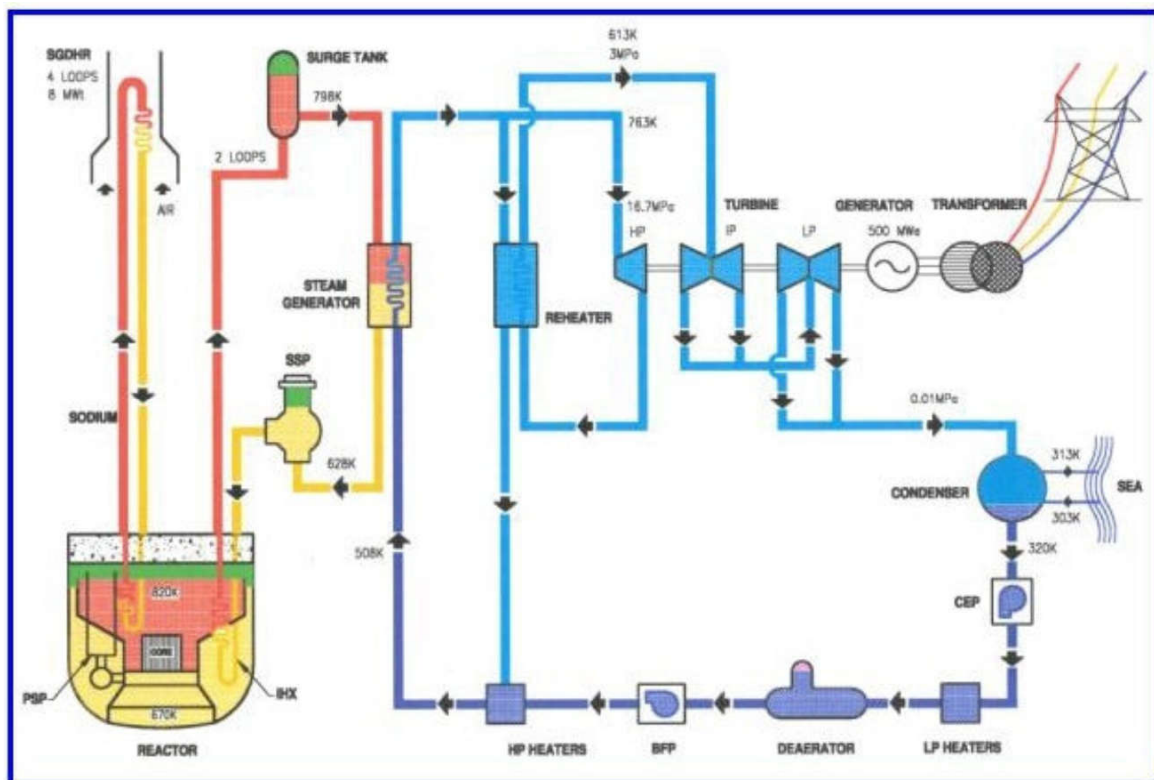


Fig. 1.1: A schematic diagram of Prototype Fast Breeder Reactor (PFBR) [6]

1.1 Steam Generator—A critical component for PFBR

Steam generator in sodium-cooled fast reactors employs a single wall separating the water/steam from the hot sodium. The high reactivity of sodium with water makes the steam generators a critical component in determining the efficient running of the plant and demands high integrity of steam generator components in case of a leak, which leads to sodium–water–steam reactions. The high integrity of these components can be achieved by choosing appropriate material followed by optimized design and fabrication conditions [7]. A schematic diagram of the steam generator is shown in Fig. 1.2. As per as PFBR is concerned, steam generator is manufactured by P91 steel having dimensions of 23 m length and 547 tubes inside. It is a vertical, counter-current shell and tube heat exchanger in which sodium flowing in the shell-side exchanges heat with the water and steam flow in the tubes produce high-pressure super-heated steam. The tubes are placed in triangular pitch and each tube is provided with expansion bend in sodium flow path at the bottom. The tubes are supported at various locations including at the middle of tube expansion bend [8]. Secondary sodium enters steam generator at 798 K and leave at 628 K. Water enter the steam generator at 508 K and leave at a temperature of 766 K and at about 165 atm. pressure. The thermal fluctuations caused by hot sodium and steam in tubes consequences thermal induced expansion and to compensate this expansion a significant bend is given to the tubes [9].

1.2 Selection of Structural Materials for Steam Generators

Selection of suitable materials for structural components for high temperature applications is crucial issue and it is based on considering mainly high temperature mechanical properties and compatibility with severe environmental service conditions. The advance in the steam cycle conditions in the steam generators of fast breeder reactors have created many material degradation problems which have major technological implications with respect to the safe design, operation and performance of reactor and steam generator components [9]. The schematic representation of

steam generator component in PFBR has shown in **Fig. 1.2**. As already mentioned, steam generators are critical components in power generating industries particularly in nuclear power industries, since these are the heat exchangers used to convert water into steam from enormous heat produced in a nuclear reactor core. During reactor operation, the steam generator components face high temperature gradients and experiences thermal stresses apart from the mechanical stress, and therefore, study of tensile behaviour at high temperature applications is essential process in the area of material design. The materials especially selected for steam generator applications in the FBRs should satisfy the necessary requirements of the following [7]:

- High temperature service
- Cyclic thermal loading
- Resistance to loss of carbon to liquid sodium and consequent loss of strength
- Resistance to wastage due to small leaks leading to sodium–water reaction
- Resistance to stress corrosion cracking (SCC) in sodium–water system
- Good thermal conductivity
- Adequate mechanical properties at the operating temperature
- Reasonable wear/erosion resistance

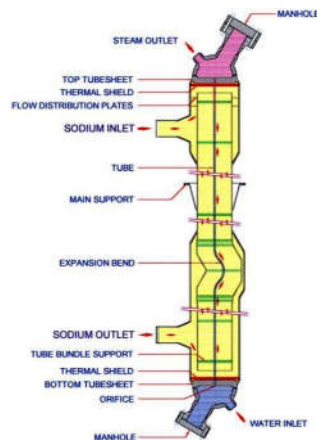


Fig. 1.2: A schematic representation of PFBR Steam Generator component [8]

1.3 Ferritic Steels—An inevitable choice of structural material

Ferritic steels are important materials in the classification of stainless steels and well established structural materials for medium to high temperature process systems. However, selection of the suitable grade for particular set of environmental conditions is challenging task as per materials engineer is concerned. Special consideration has been given to high temperature properties and microstructural stability of the steels, so that selected ferritic steels can be used in the temperatures between 673 K to 923 K. Other major requirements in terms of mechanical properties to be considered before selection of steels includes better creep resistance, adequate fatigue resistance, good thermal shock resistance, reasonable fracture properties, and low ductile to brittle transition temperature (DBTT). Apart from above major properties, the other essential requirement is high resistance to corrosion and oxidation since the material is going to be used in water–steam systems in power generating plants. Different varieties and grades of ferritic steels are being used currently in different industrial applications throughout global and utmost importance has been given to the Cr–Mo based steels which plays pivotal role in numerous applications like steam generator material in fossil fired plants, FBRs, fuel cladding material in advanced gas cooled reactors (AGRs) and oil and petrochemical industries [10]. Ferritic steels containing 9–12% chromium have extensive usage at elevated temperature applications due to balanced combination of mechanical and corrosion properties. Importance in the ferritic steels has been increased recently because of their proposed use in the fast reactor components and in solar central receivers. The physical metallurgy of the recently developed chromium–molybdenum steels focus on the microstructural influence on the Low Cycle Fatigue (LCF) and creep behaviour. This stability in both microstructure and properties are crucial for any alloy used as a structural material intended for 40 years of elevated temperature service [11].

1.4 Outline of project thesis

The current thesis is divided into five chapters and the scope of each chapter is briefly given below. The chapter-4 of the thesis contains the tensile properties and work hardening behaviour of boron added P91 steel based on the experimental results.

Chapter 1: Chapter one presents a brief introduction on boron added P91 steel, selection criteria for structural applications of steam generators, small introduction to ferritic steels for steam generator components of PFBR.

Chapter 2: It contains a brief introduction and evolution of 9% Cr steels including physical metallurgy of various versions of ferritic steels such as 2.25Cr–1Mo (**Grade 22**), 9Cr–1Mo (**P9**), and modified 9Cr–1Mo (**P91**), boron added P91 steel (**P91B**) and P92 steel. In the last phase general description on tensile stress–strain and work hardening behaviour of engineering materials using different constitutive flow equations.

Chapter 3: In this chapter a detailed explanation on material, composition and experimental procedure. A small explanation on type of machine used for tensile test was given including test conditions.

Chapter 4: This chapter mainly consists of results and discussion on temperature and strain rate effects on tensile flow and work hardening behaviour of boron added P91 steel. A detailed explanation has also been given on effect of strain rate and temperature on tensile properties and work hardening parameters predicted by using different constitutive equations.

Chapter 5: A detailed discussion on comparison of tensile properties and work hardening parameters derived from Ludwigson and Voce of boron added P91 steel and P91 steel have been presented.

Chapter 6: Conclusion and future work on boron added P91 steel is presented.

Chapter 2 : LITERATURE REVIEW

2.0 Introduction

This chapter consists two main sub-sections in which one deals with the literature review related to the evolution and metallurgical aspects of 9% Cr ferritic steels and the second sub-section deals with general aspects of tensile flow and work hardening behaviour of engineering materials. In addition to this, various constitutive flow equations available for modeling the tensile flow and work hardening behaviour were also presented. Constitutive flow equations intended to describe the materials behaviour in the region of uniform plastic deformation in the tensile stress-strain curve of materials is clearly explained.

2.1 Ferritic steels

Steels are mainly an alloy of iron and carbon. These are further classified based on their compositional type (e g C-Mn, Cr-Mo), on their end use (Tool steel, Rail steel), on their characteristics (high temperature strain, machinability), on their method of manufacture (Rimmed, Semi-killed, Killed and calcium-treated), on their descriptive or trade name (Maraging, Corten), on their microstructural type (Austenitic, Ferritic, Bainitic, Martensitic, Precipitation hardened) or by a combination of these (Austenitic stainless, Rare-earth-treated C-Mn) etc. [12]. Basically Cr-Mo steels categorized under low-alloy type steel widely used in the petrochemical and power generation industries as pressure vessels, piping, boilers and other structural parts. These steels exhibit usually good resistance to creep and corrosion, high toughness and weldability, and have an excellent cost effective ratio. At the same time, these materials have two important properties for specific applications: a low thermal expansion co-efficient and a high thermal conductivity. All these factors make Cr-Mo steels very attractive to operate at high temperatures and under low stress conditions [13, 14].

2.1.1 Evolution of 9% Chromium steels

Ferritic steels in the present study belongs to the family of Cr and Mo type steel, with nominal carbon content ($<0.2\%$ C) considered as a crucial structural material for high temperature applications. These conventional low-alloy steels simply contain chemical elements of C, Si, Mn, Cr, and Mo, while the creep strength-enhanced ferritic steels contain additional elements from the variety of W, V, Nb, Ti, N, B, etc. The addition of chromium makes steel with good resistance to high temperature oxidation and molybdenum for enhanced creep strength. These steels also have excellent resistance to hydrogen attack at high temperature and pressures. Ferritic steels are extensively used as structural materials in steam generating systems of fossil fired, nuclear power, petro-chemical and other heat transporting industries by considering its good thermo-physical properties, high temperature oxidation resistance and better mechanical properties coupled with cost effectiveness. These are the main reasons for selection of ferritic steels as a structural material for steam generator applications in PFBR at Kalpakkam India, and other fossil power plants and heat transport systems as compared to austenitic stainless steels. The evolution of ferritic steels starts at the advent of power in the early 1950s, and a continuous demand for energy driven the development of heat resistance steel $2\frac{1}{4}\text{Cr}-1\text{Mo}$ designated as ASTM Grade 22 was widely used in fossil power plants as well as in heat transport systems in the early days. Ferritic $2\frac{1}{4}\text{Cr}-1\text{Mo}$ steel is basically low carbon and low alloy steel with initial intention of using as a structural material for conventional and later for ultra-supercritical power plant boiler systems. Subsequently 9Cr-1Mo (ASTM Grade 9) steel was developed to improve high temperature oxidation resistance. The flow chart/sheet as shown in **Fig 2.1** demonstrates the progressive evolution of high temperature ferritic steels with base composition of 2 wt. % Cr, 9 wt. % Cr and 12 wt. % Cr for 10^5 h creep rupture strength at 600°C . Since then, continual drive to increase operating temperature of conventional fossil-fired power plants to increase thermal efficiency and reduce CO_2 emission led to the development of several ferritic steels with improved elevated temperature strengths and

oxidation resistance [15-19]. Evolution of ferritic steels (Fig. 2.1), began with T22 and T9 and 12% Cr steels with 10^5 h creep–rupture strength at 600° C of about 35MPa, has resulted in increasing operating steam temperatures and pressures. The main intension of increase in chromium content was to increase oxidation resistance of the material. Three generations of steels have been introduced since the introduction of T22, T9, T91, 12% Cr steel, and steels of fourth generation are in the development stage (Fig. 2.1). With increasing operating temperatures up to 600° C, emphasis shifted from 2.25 to 9 and 12 wt. % Cr for better oxidation and corrosion resistance. Chromium is a ferrite stabilizer, and with increase from 9 to 12, it was necessary to add austenite stabilizers to achieve complete austenitisation to obtain 100% martensitic structure.

The development progresses of ferritic steels are given below.

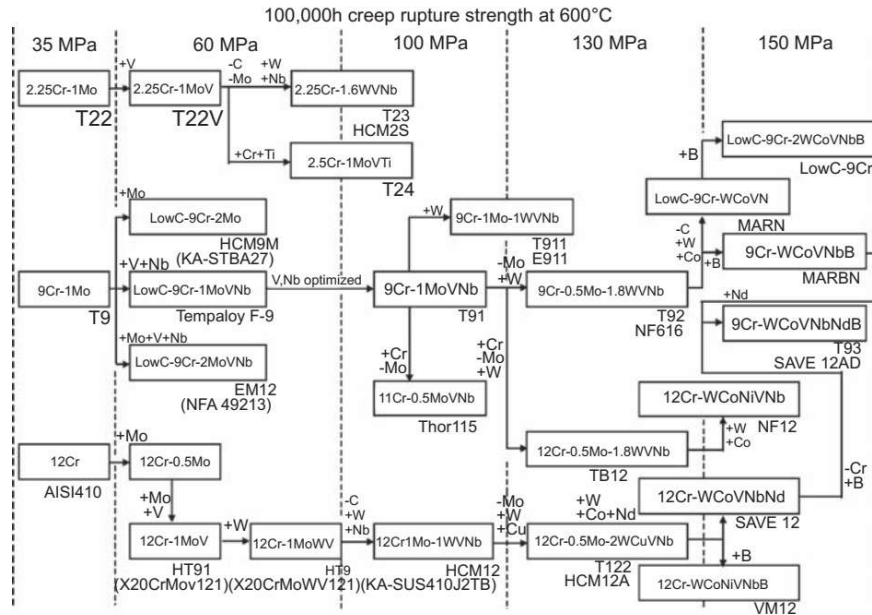


Fig. 2.1: Evolution of ferritic steels as a function of allowable stress for 10^5 hr. creep rupture life at 600° C [13]

2.1.1.1 $2\frac{1}{4}$ Cr–1Mo Steel (Grade 22)

The $2\frac{1}{4}$ Cr–1Mo steel designated as ASTM Grade 22 is considered as potential candidate structural material for pressure vessel applications in future light water reactors. Two main important reasons for selecting this material for above application are its good fracture

toughness (in particular low temperature value of the start of the upper shelf) and good resistance to radiation-induced embrittlement as compared to usual pressure vessel steels. Moreover, it has good weldability for manufacturing of thick-walled pressure vessel. The microstructure of any ferritic steel usually formed by continuous cooling from austenite phase to required phase is given by its time-temperature-transformation diagram. The $2\frac{1}{4}\text{Cr}-1\text{Mo}$ steel is used in various conditions including annealed, normalised + tempered and quenched + tempered. The microstructure of annealed steel is predominantly ferrite with some gross carbide area (that sometimes appears as pearlite) and possibly bainite. Normalized $2\frac{1}{4}\text{Cr}-1\text{Mo}$ steel contains ferrite and bainite and the amount of bainite increase with carbon to nearly 100% of the structure for carbon levels greater than about 0.12 wt. %. Quenched $2\frac{1}{4}\text{Cr}-1\text{Mo}$ steel has the potential to contain full martensite. The mechanical properties of $2\frac{1}{4}\text{Cr}-1\text{Mo}$ steel depend primarily on the carbide type, size, morphology and distribution. Baker and Nutting [20] have described the general sequence of carbides formed in $2\frac{1}{4}\text{Cr}-1\text{Mo}$ steel during tempering heat treatment. Prior to tempering, the microstructure contains epsilon (ϵ) carbides which can be described as $\text{Fe}_{2.4}\text{C}$. These precipitates appears alone in the martensitic structure but is accompanied by cementite formed homogeneously from diffuse zones. Mo_2C has considerable solubility for other alloying elements, especially chromium, and should probably be referred to as M_2C . At this point, the carbide sequence splits with the formation of Cr_7C_3 (generally denoted as M_7C_3) and M_{23}C_6 (chromium rich carbide). The M_7C_3 probably nucleates at the M_2C / matrix interface while the M_{23}C_6 nucleates and grows at grain boundaries as large spheroidal particles. The last carbide to form M_6C grows at the expense of all other carbides and is believed to be the equilibrium precipitates in $2\frac{1}{4}\text{Cr}-1\text{Mo}$ steel. After normalizing, the ferrite is free of any carbide. The first precipitate to appear in the ferrite during tempering is acicular M_2C particles which develop from diffuse zones in the matrix similar to those observed in the bainite. These carbides present in the ferrite, showing no tendency

to transform to any of the other metastable carbides observed in the other micro-constituents. Eventually, M_6C forms in the ferrite and the M_2C begins to dissolve. The limitations of this material include a potential for higher hydrogen embrittlement and hydrogen attack susceptibility as well as a maximum design temperature limitation of 454° C. Considering above limitations, this alloy has found limited acceptance.

2.1.1.2 9Cr–1Mo steel (P9)

9Cr–1Mo steel is the improved version of $2\frac{1}{4}Cr-1Mo$ (ASTM Grade 22 steel) by increase in **chromium** content and become a crucial structural material for the power generating industries over the present generation of steels. Good creep properties combined with adequate oxidation and corrosion resistance have derived this material to use at the temperatures of 550° C and above [14]. High chromium martensitic steels show superior mechanical properties in irradiation field in terms of void swelling, thermal and irradiation creep and thermal fatigue properties as compared to austenitic steels. The material is commonly used in normalized and tempered condition and after tempering material shows tempered martensitic microstructure with a high density of dislocations. Normalizing and tempering heat treatments produce tempered martensitic structure with carbides decorating both on the prior austenitic grain boundaries and martensitic lath boundaries. The general sequence of carbide formation in 9Cr–1Mo steel has been reported [21] as $Fe_3C \rightarrow M_7C_3 \rightarrow M_{23}C_6$. M_2X types of carbides/nitrides are also reported in the intragranular region. Senior et al. [22] from their extensive TEM studies have indicated that the population of these precipitates on the prior austenite grain boundaries and on the martensitic lath boundaries are almost $M_{23}C_6$ and the population of other precipitates within the laths consists of appreciable quantities of both $M_{23}C_6$ and Cr_2N particles.

2.1.1.3 Modified 9Cr–1Mo steel (P91)

Mod.9Cr–1Mo steel (**P91**) is a modified version of high chromium plain P9 steel modified by alloying with **niobium** and **vanadium** elements. It is extensively used as structural material at elevated temperature applications in fossil-fired as well as nuclear power plants [18]. Interest in this steel arises primarily due to its proposed use for tubing in the re-heater and super-heater portions and as a thick-section tube plate material in the steam generators of LMFBRs [2, 3, 8,]. The selection of P91 steel for steam generator application in LMFBR is based on its high thermal conductivity and low thermal expansion coefficient, coupled with a good resistance to stress corrosion cracking (SCC) in water-steam systems compared to austenitic stainless steels and better monotonic tensile and creep strength at elevated temperatures compared with the P9 steel [2, 7, 8, 9, 19]. The good microstructural stability over long periods of exposure to high temperature service conditions and consequent improvements in the creep strength are other attractive features that favored the P91 steel to select for steam generator applications. This steel is normally used in the normalized and tempered heat treated condition. The normalizing treatment is carried out at 1060° C for 25 min. followed by air cooling, while tempering is at 750° C for 1 hr. followed by air cooling. Austenisation during the normalizing dissolves all most all secondary phases (carbides/nitrides/carbo-nitrides) and the austenite transforms into martensite with lath morphology during the cooling. During tempering of martensite phase the precipitation of $M_{23}C_6$ carbides on lath boundaries as well as on prior austenite grain (PAG) boundaries would takes place [18-20]. The microstructure of this class of steels is therefore made up of several scales (**Fig. 2.2**), the most predominant of which is the PAG structure that forms during the normalizing treatment. Depending on the heat treatment, the size of the PAG varies between 10 and 50 μm . Inside each PAG boundary, packets of laths form during the martensitic transformation associated with air cooling following austenisation and sub-grains form inside the lath during the tempering treatment. The dominant precipitates in the alloy are large (**60–150 nm**) $M_{23}C_6$ particles that are mainly on

lath boundaries and prior-austenite grain boundaries. The V and Nb give rise to a fine distribution of small (20–80 nm) MX type precipitates (V, Nb) (C, N) [21, 22]. Addition of Nb also help in improving the properties by promoting nucleation of finely distributed $M_{23}C_6$ carbides and by aiding grain refinement, whereas V enters the carbide particles and retards its growth. The alloy derives its strength in normalized and tempered condition, from carbides like NbC, VC and $M_{23}C_6$ on sub-boundaries and from the tempered martensitic laths with high dislocation densities. In addition, C and Cr could also form fine precipitates of nitrides within the ferrite matrix contributing to further strengthening [23-26]. Molybdenum is a strong solid solution strengthener and acts as a retardant for dislocation recovery/recrystallization.

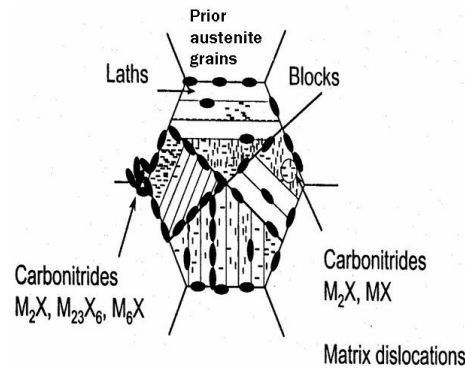


Fig. 2.2: Schematic representation of non-uniform precipitation states in tempered martensitic 9–12% Chromium steels [17]

2.1.1.4 Boron added P91 steel (P91B)

As already discussed above, 9Cr–1Mo steel modified with alloying additions of niobium and vanadium is favored candidate structural material for high temperature applications, such as boiler and turbine components in power plants due to their excellent combination of high-temperature creep and oxidation-resistant properties [10, 13, 14, 17, 19]. However, it has been reported that these steels have been suffering with lower Type-IV cracking resistance during creep deformation at high temperature application of weldments. However, recent studies proven that small and controlled addition of boron to these steels exhibits tremendous improvement in resistance to Type-IV cracking for short as well as long term creep rupture behaviour [1, 3, 4].

Boron stabilizes martensitic microstructure in the vicinity of prior austenite grain boundaries (PAGBs) for the improvement of long-term creep strength of tempered martensitic 9Cr steel at 650° C [3, 4]. On the other hand, the controlled addition of nitrogen causes the precipitation of fine MX carbo-nitrides with vanadium and niobium in 9–12% Cr steels, which contributes to the improvement of creep strength. Boron has strong affinity towards nitrogen and the relationship between boron and nitrogen concentrations encourage for forming boron nitrides than boron carbides which results higher creep rupture strength than conventional steels T91 and P92 at 650° C. Formation of boron nitrides (BN) type precipitates is more beneficial than boron carbides (BC) type precipitates as BC precipitates easily dissolve in matrix for upon long exposure to high temperature. Ultimately it is concluded and well proved that boron added P91 steel has significant beneficial effect for high temperature properties particularly high resistance to Type-IV cracking than ancestor 9% Chromium steels [1, 3, 4].

2.1.1.5 9Cr–0.5Mo –1.8W–V–Nb Steel (P92)

The improved version of P91 steel designated as P92 steel according to ASTM standards [27] is also known as NF616 steel. P92 steel has been developed by the addition of 1.8 wt. % **tungsten** with reduced **molybdenum** in the P91 steel which is already modified by the addition of strong carbide/nitride forming elements such as niobium and vanadium along with controlled nitrogen. P92 ferritic steel is an important structural material developed for steam generator applications in the ultra-super critical (USC) power plants with increased operating steam temperatures and pressures in order to achieve higher efficiency and better environmental protection [28]. The choice of P92 steel for steam generator applications is based on the low thermal expansion co-efficient and high resistance to stress corrosion cracking in water-steam systems compared to austenitic steels, in addition to that better mechanical properties at elevated temperatures than the alternate P9 and P91 steels [29]. The microstructure of P92 steel in the normalized and tempered condition consists of tempered lath martensite with hierarchical

microstructure comprising of prior austenite grains (PAGs), packets, blocks, sub-blocks and laths along with precipitates such as $M_{23}C_6$ carbides at the boundaries, and Nb and V-rich MX-type carbo-nitrides/nitrides in the intra-lath matrix regions/sub-grain interiors. The superior elevated temperature mechanical properties of P92 steel is derived mainly from higher solid solution strengthening due to the addition of **tungsten**, with initial high dislocation density accumulated from austenite to martensitic transformation, hardening due to hierarchical boundaries and precipitation hardening from $M_{23}C_6$ carbides and MX-type carbo-nitrides/nitrides. It has been reported that the presence of tungsten improves the stability of primary and secondary precipitates along with dislocation sub-structure with lower rate of recovery [30].

2.2 Tensile deformation behaviour of engineering materials

The tensile stress-strain behaviour of engineering materials generally studied to understand the basic deformation behaviour, control of processing parameters during fabrication and prediction of performance during operation. Determination of tensile plastic deformation behaviour is influenced by several factors that include metallurgical/material variables, test methods, and the nature of the applied stresses. The main factors affecting shape and magnitude of stress-strain behaviour are composition, heat treatment, prior history of plastic deformation, strain rate, temperature and state of stress [31, 32].

2.2.1 Classification of stress-strain curves

The tensile test data is basically used to obtain basic design information on the strength of materials and as an acceptance characterization test for the specification of materials. Tensile test involves a specimen is subjected to continuously applying uniaxial load (force) and simultaneous elongation of the specimen can be recorded. In tensile test, the test specimen experiences two modes of deformation; they are **initial recoverable elastic deformation** and **final unrecoverable plastic deformation**. Initial elastic deformation in materials is reversible and regains its original shape upon unloading, whereas plastic deformation is irreversible and causes

permanent deformation even if load is removed [32-35]. The parameters obtained from the stress–strain behaviour of a metal are the **yield strength** or **yield point**, **tensile strength**, **percent elongation**, and **reduction in area**. The first two are related to strength parameters and the last two indicates ductility. Based on shape of the flow behaviour the tensile stress–strain curves are classified in five different types:

2.2.1.1 Elastic response: Type–I

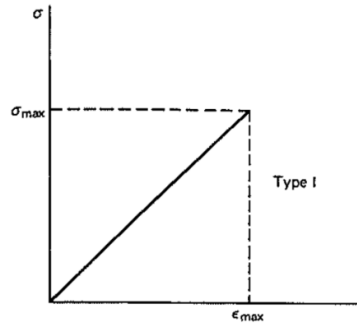


Fig. 2.3: Type–I stress–strain behaviour revealing completely elastic response [36]

Type–I stress–strain behaviour completely related to elastic response of the material. It is represented basically by Hooks law.

$$F = kx \quad (2.1)$$

where F = applied force,

x = associated displacement,

k = proportionality factor or constant

when the force acts on the cross–sectional area ‘A’ and the displacement ‘x’ related to some reference gauge length ‘l’, then $F = kx$ can be re written as

$$\sigma = E\varepsilon \quad (2.2)$$

Where $\sigma = F/A =$ stress,

$\varepsilon = x/l =$ strain,

and E= proportionality constant (often referred to as Young’s modulus or modulus of elasticity)

The parameters derived from Elastic response of stress–strain diagram are explained below in detail.

Young's modulus

The slope of the initial linear portion of the stress–strain curve represents the modulus of elasticity or Young's modulus (**Fig. 2.3**). The modulus of elasticity (E) represents the stiffness of the material. The modulus of elasticity is the structure–insensitive mechanical property. It is slightly affected by alloying additions, heat treatment, or mechanical work **[31-36]**. Typical values of modulus of elasticity for various alloys at different temperatures are given in **Table-2.1** below;

Table-2.1: Typical values of modulus of elasticity for various alloys at different temperatures

Material	Modulus of elasticity, GPa				
	Room temp.	477 K	700 K	810 K	922 K
Carbon steel	207	186	155	134	124
Austenitic stainless steel	193	176	159	155	145
Titanium alloys	114	97	74	70	
Aluminum alloys	72	66	54		

Courtesy: Mechanical Metallurgy by G.E. Dieter **[34]**

Resilience

It is material ability to absorb energy when deformed elastically and retains original shape when unloaded is called resilience. Modulus of resilience characterized by the strain energy per unit volume required to stress the materials from zero stress to yield stress σ_0 , the strain energy per unit volume for uniaxial tension is;

$$U_0 = \frac{1}{2} \sigma_x e_x \quad (2.3)$$

$$\text{The modulus of resilience is } U_R = \frac{1}{2} \sigma_0 e_0 = \frac{1}{2} \sigma_0 \frac{\sigma_0}{E} = \frac{\sigma_0^2}{2E} \quad (2.4)$$

In other words, the area under elastic region in the engineering stress–strain curve represents the resilience of material. Different materials have different values of modulus of resilience has shown in **Table-2.2** below:

Table-2.2: Modulus of resilience for various materials [34]

Material	E , GPa	s_0 , MPa	Modulus of resilience, U_R , kPa
Medium-carbon steel	207	310	232
High-carbon spring steel	207	965	2250
Duralumin	72	124	107
Copper	110	28	3.5
Rubber	0.0010	2.1	2140
Acrylic polymer	3.4	14	28

Courtesy: Mechanical Metallurgy by G.E. Dieter [34]

2.2.1.2 Elastic–Homogenous Plastic response: Type–II

When the materials experience plastic deformation–irreversible flow–the stress–strain curve often assumes the shape of following curve,

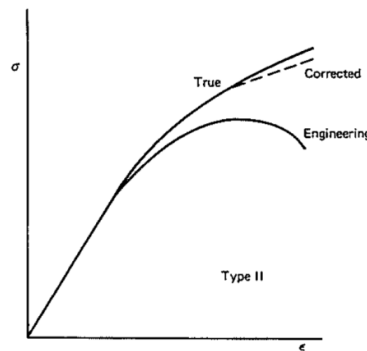


Fig. 2.4: Type–II stress–strain behaviour exhibits elastic behaviour followed by a region of homogenous plastic deformation [36]

It has been clearly observed from **Fig. 2.4** that represent **Type–II** stress–strain curve has shown both engineering and true components of stress–strain curves, in both cases curves shows single elastic region at small strains followed by a two smooth parabolic portion of the engineering and true stress–strain curves associated with homogenous plastic deformation processes, such as the

irreversible movement of dislocations in materials. The true stress–strain curve continuous to rise to a maximum stress level with respect to engineering stress–strain curve that reflects an increase in resistance on the part of the material to further plastic deformation—a process known as strain hardening. The parameters can be estimated from **Type–II** stress–strain behaviours are;

Proportionality limit: it is a finite stress at zero strain, below which stress is exactly proportional to strain.

Elastic limit: it is the stress level below which the deformation strains are fully reversible.

Yield strength: The yield strength or offset yield strength (S_o) is the stress at which strain deviates from the elastic region to plastic region and it depends on sensitivity of strain measurement.

$$s_o = \frac{P_{(\text{strain offset} = 0.002)}}{A_0} \quad (2.5)$$

Tensile strength: The tensile strength or ultimate tensile strength (S_u) is the maximum load without fracture. Mathematically it is represented as;

$$s_u = \frac{P_{\max}}{A_0} \quad (2.6)$$

Ductility: Ductility represents the material elongation useful in the material forming operations. Conventionally ductility is measured by two ways (1) measurement of engineering strain up to fracture (e_f) (usually called the elongation) and (2) measurement of reduction in area at fracture (q). Elongation and reduction in area usually are expressed as a percentage and mathematically represented as;

$$e_f = \frac{L_f - L_0}{L_0}$$

$$q = \frac{A_0 - A_f}{A_0} \quad (2.7)$$

where L_0 , A_0 are initial gauge length and cross–sectional area and L_f , A_f are final gauge length and cross- sectional area of the specimen.

Toughness: The toughness is an ability of material to absorb energy in the plastic range. Particularly parts like freight-car couplings, gears, chains, and crane hooks should have ability to with stand occasional stresses above the yield stress without fracturing. One way of looking at toughness is to consider that it is the total area under plastic region in the engineering stress–strain curve.

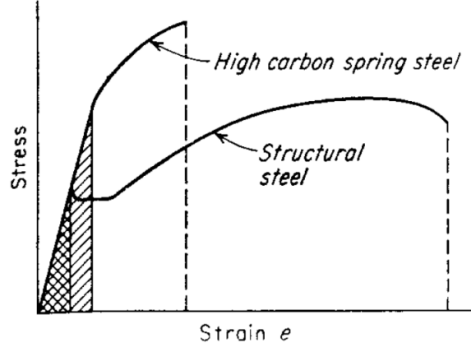


Fig. 2.5: Comparison of stress–strain curves for high and low toughness materials [36]

The total area under plastic region indicates the amount of work per unit volume which can be done on the material without causing it to rupture. **Fig. 2.5** shows the comparison of stress–strain curves for high and low toughness materials. The high carbon spring material shows higher yield strength and tensile strength than the medium carbon structural steel. It can be observed that the structural steel is more ductile with greater total elongation. The total area in plastic region under the stress–strain curve is greater for the structural steel reflects this steel is tougher. Toughness is a parameter which comprises both strength and ductility [31-36]. For ductile materials, the area under the stress–strain curve can be approximated by the following equations;

$$U_T \approx s_u e_f$$

$$U_T \approx \frac{s_0 + s_u}{2} e_f \quad (2.8)$$

For brittle material the approximated equation is $U_T \approx \frac{2}{3} s_u e_f$ all these equations are only approximations to the area under the stress–strain curves.

2.2.1.3 Elastic–Heterogeneous Plastic response: Type–III

Sometimes, occasionally a test specimen produce a stress–strain curve that exhibits a series of serrations superimposed on the parabolic portion of curve after normal range of elastic response. Such behaviour in stress–strain curve reflects non uniform or heterogeneous deformation. Serrated stress–strain response is identified to be happen at least in two different conditions, e.g., (i) when hexagonal close–packed metals are tested over a relatively wide temperature range and (ii) whenever the instantaneous strain rate in the material exceeds the rate of motion of the test machine cross–head that leads to a load drop. A similar stress–strain response is found in BCC metals tested at low temperatures and in FCC metals tested at both low temperature and high strain rates. The schematic diagram of **Type–III** stress–strain curve is shown below in **Fig. 2.6**.

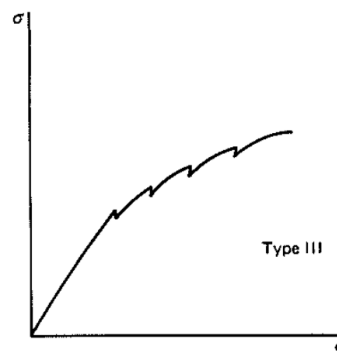


Fig. 2.6: Type–III stress–strain behaviour reflecting elastic behaviour followed by heterogamous plastic flow [36]

Serrated stress–strain curves are also encountered in BCC iron alloys containing carbon in solid solution and in dilute solid solutions of aluminum. It has been argued that the Portevin–Le–Chatelier effect (serrated σ – ϵ curve) is due to solute atom or vacancy interaction with lattice dislocations. When sufficient stress is applied, dislocations can break free from solute clusters and cause load drop. If the solute atoms can diffuse quickly enough to re–trap these dislocations, then more load need to be applied once again to continue the deformation process. This lock and unlock process during deformation responsible for the occurrence of serrations in the stress–strain behaviour of engineering materials

2.2.1.4 Elastic–Heterogeneous Plastic–Homogeneous Plastic response: Type–IV

In many BCC iron based alloys and some non–ferrous alloys, a relatively narrow region of heterogeneous plastic deformation separates the elastic region from the homogeneous plastic flow portion of the stress–strain curve. This segment of curve is caused by the interaction of dislocations and solute atoms. The schematic representation of **Type–IV** has shown in **Fig. 2.7**.

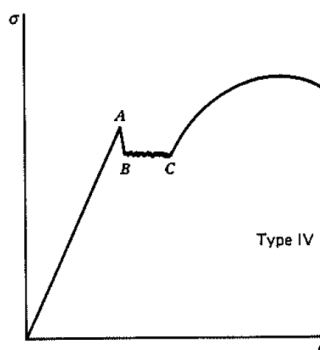


Fig. 2.7: Type–IV stress–strain curve shows a narrow heterogeneous deformation regime between initial elastic and final homogeneous flow regimes [36]

It can be observed from **Fig.2.7**, after being loaded elastically to A, defined as the upper yield point, the material is observed to develop a local deformation band, the sudden onset of plastic deformation associated with this Luder band is responsible for the initial load drop to B, defined as lower yield point. The yield strength of material exhibiting Type–IV behaviour is usually reported as the lower yield–point value.

2.2.1.5 Elastic–Heterogeneous Plastic–Homogeneous Plastic response: Type–V

Type–V behaviour may be found in the deformation of some crystalline polymers. The representative diagram of Type–V has shown in **Fig. 2.8**. It can be observed from above diagram, that an upper yield point and subsequent load drop similar to that observed in Type–IV response, the final deformation stage is decidedly different. Explanation about Type–V response is irrelevant to the present class of material, hence detailed information is not required to present here.

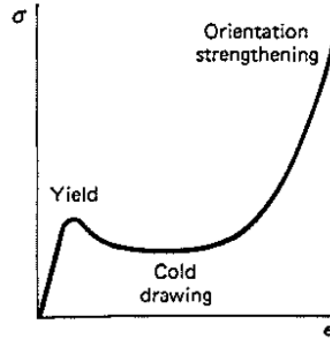


Fig. 2.8: Type-V stress-strain behaviour usually found in crystalline polymers [36]

2.2.2 Engineering stress-strain curve

Engineering stress-strain curve is constructed from the initial load-elongation measurements. The schematic representation of engineering stress-strain diagram has shown in

Fig. 2.9.

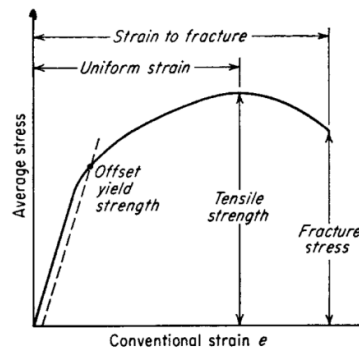


Fig. 2.9: The engineering stress-strain curve [34]

The engineering stress (s) is characterized by the average longitudinal stress in the tensile specimen. It is obtained by dividing the load (P) by the original area of the cross section of the specimen (A_0)

$$s = \frac{P}{A_0} \quad (2.9)$$

where P = applied load, A_0 = original cross-sectional area

The strain (e) used for the engineering stress–strain curve is the average linear strain, which is obtained by dividing the elongation of the gage length of the specimen (δ) by its original length (L_0).

$$e = \frac{\delta}{L_0} = \frac{\Delta L}{L} = \frac{L - L_0}{L_0} \quad (2.10)$$

L_0 = Original gauge length, L = Final gauge length

It is believed that the stress–strain curve shape and magnitude are influence by material composition, heat treatment, prehistory of cold work, applied strain rate, test temperature, and imposed state of stress during the testing [34].

2.2.3 True stress–true strain curve

The engineering stress–strain curve is based entirely on the original dimensions of the specimen and it cannot describe the true indication of deformation behaviour of material because, during deformation the specimen dimensions change continuously during the test. In the true stress–strain curve, an instantaneous dimension change gives true indication of deformation characteristics of material. The average stress based on original area decrease and this produce the fall–off in the stress–strain curve beyond the point of maximum load. In fact, it can be observed that the metal remains strain hardens all the way up to fracture, and then obviously the stress required producing further deformation increases. The true stress–strain curve is also known as the flow curve [31-36].

The true stress (σ) is expressed in terms of engineering stress (s) and engineering strain (e) by,

$$\sigma = \frac{P}{A_0}(e + 1) = s(e + 1) \quad (2.11)$$

The true strain (ϵ) is determined from the engineering strain (e) by the following eq.

$$\epsilon = \ln(e + 1) \quad (2.12)$$

True stress and true strain curve does represent yield point. It also does not show the linear elastic region. The parameters usually determined from the true stress–strain curve are as follows:

True stress at maximum load (σ_u):

It actually represents the true tensile strength. Most of the materials necks at maximum load with a strain where the true stress equals the slope of the flow curve.

σ_u = true stress at maximum load, ϵ_u = true strain at maximum load, and A = cross sectional area

$$s_u = \frac{P_{\max}}{A_0}$$

$$\sigma_u = \frac{P_{\max}}{A_u} \quad \epsilon_u = \ln \frac{A_0}{A_u} \quad (2.13)$$

Eliminating P_{\max} yields

$$\sigma_u = s_u \frac{A_0}{A_u}$$

$$\sigma_u = s_u e^{\epsilon_u} \quad (2.14)$$

True fracture stress (σ_f):

σ_f represents the load at fracture divided by the cross sectional area of the specimen at fracture.

True fracture strain (ϵ_f):

It is the logarithmic ratio of true strain based on the original area A_0 and the area after fracture A_f .

$$\epsilon_f = \ln \frac{A_0}{A_f} \quad (2.15)$$

It represents the maximum true strain the material can with stand up to fracture.

True uniform strain (ϵ_u):

It is true strain up to maximum load, calculated from either the specimen cross–sectional area (A_u) or the gauge length (L_u) at maximum load.

$$\epsilon_u = \ln \frac{A_0}{A_u} \quad (2.16)$$

True local necking strain (ϵ_n):

The local necking strain (ϵ_n) represents the strain from maximum load to fracture.

$$\epsilon_n = \ln \frac{A_u}{A_f} \quad (2.17)$$

2.2.4 Instability in tension

Necking begins at maximum load during the tensile deformation of a ductile metal. An ideal plastic material with no strain hardening would become unstable in tension and begin to neck as soon as yielding starts. In reality material undergoes strain hardening during deformation, because of that the load-carrying capacity of the specimen increase. Necking or localized deformation take place at maximum load, where the cross-sectional area of the specimen decreases more due to increase in stress than the strain hardening induced load-carrying ability of the metal. The instability condition represents the localized deformation is defined by the condition $dP = 0$.

$$\begin{aligned} P &= \sigma A \\ dP &= \sigma dA + A d\sigma = 0 \end{aligned} \quad (2.18)$$

From the constancy of volume relationship

$$\frac{dL}{L} = -\frac{dA}{A} = d\epsilon \quad (2.19)$$

$$-\frac{dA}{A} = \frac{d\sigma}{\sigma} \quad (2.20)$$

So that at a point of tensile instability

$$\frac{d\sigma}{d\epsilon} = \sigma \quad \text{Or} \quad \theta = \sigma \quad (2.21)$$

Therefore, the point of necking at maximum load can be obtained from the true stress–true strain curve by finding the point on the curve having a sub-tangent of unity (**Fig.2.10a**), or the point where the rate of strain hardening equals the stress (**Fig.2.10b**).

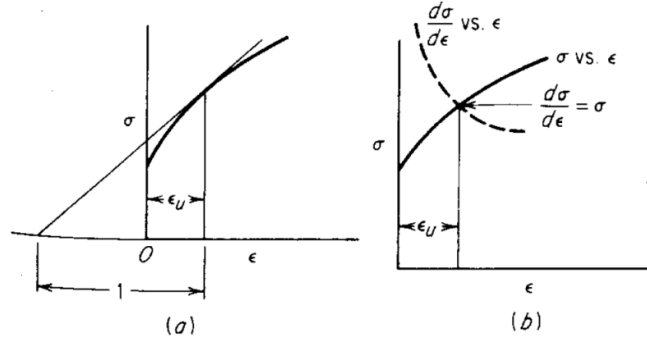


Fig. 2.10: Graphical representation of necking criteria [34]

The necking criteria can be expressed more explicitly if engineering strain is used

$$\frac{d\sigma}{d\epsilon} = \frac{d\sigma}{de} \frac{de}{d\epsilon} = \frac{d\sigma}{de} \frac{dL/L_0}{dL/L} = \frac{d\sigma}{de} \frac{L}{L_0} = \frac{d\sigma}{de} (1 + e) = \sigma \quad (2.22)$$

$$\frac{d\sigma}{de} = \frac{\sigma}{1 + e} \quad (2.23)$$

The above equation represents the **Considere's construction** for the determination of the point of maximum load, and it has been shown in below **Fig 2.11**.

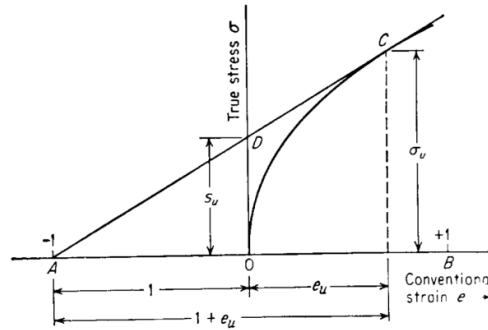


Fig. 2.11: Considere's construction for the determination of the point of maximum load [34]

2.2.5 Effect of strain rate on tensile properties

In tensile test, applied strain rate and temperature changes the stress-strain behaviour of materials. Strain rate ($\dot{\epsilon}$) defined as, $\dot{\epsilon} = d\epsilon / dt$ expressed in unit of s^{-1} . The spectrum of strain rates are given in **Table-2.3**.

Table- 2.3: Spectrum of strain rate [34]

Range of strain rate	Condition or type test
10^{-8} to 10^{-5} s^{-1}	Creep tests at constant load or stress
10^{-5} to 10^{-1} s^{-1}	“Static” tension tests with hydraulic or screw-driven machines
10^{-1} to 10^2 s^{-1}	Dynamic tension or compression tests
10^2 to 10^4 s^{-1}	High-speed testing using impact bars (must consider wave propagation effects)
10^4 to 10^8 s^{-1}	Hypervelocity impact using gas guns or explosively driven projectiles (shock-wave propagation)

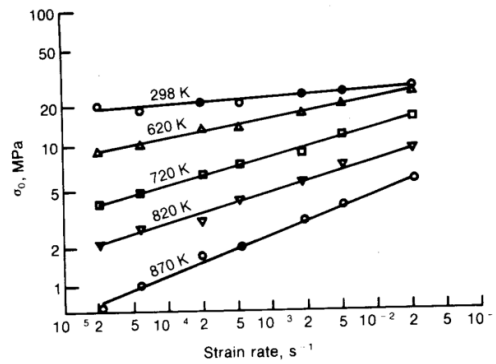


Fig. 2.12: The variation of yield stress as a function of applied strain rate [34]

From the **Fig 2.12**, it can be observed that with increase in strain rate increases the flow stress of material. The strain rate dependence flow stress increases with increasing temperature. The yield stress as well as flow stress at lower plastic strain regime of material is more strain rate dependent than the tensile strength. Higher rate of strain cause the yield point phenomenon in low carbon steels that do not show a yield point under ordinary rates of loading.

The crosshead velocity is $v = dL / dt$,

The strain rate expressed in terms of conventional linear strain is $\dot{\epsilon}$.

$$\dot{\epsilon} = \frac{de}{dt} = \frac{d(L - L_0)/L_0}{dt} = \frac{1}{L_0} \frac{dL}{dt} = \frac{v}{L_0} \quad (2.24)$$

The conventional strain rate is proportional to the cross-head velocity.

The true strain rate $\dot{\epsilon}$ is given by

$$\dot{\epsilon} = \frac{d\epsilon}{dt} = \frac{d[\ln(L/L_0)]}{dt} = \frac{1}{L} \frac{dL}{dt} = \frac{v}{L} \quad (2.25)$$

The true strain rate can be related to the conventional strain rate by the following equation;

$$\dot{\epsilon} = \frac{v}{L} = \frac{L_0}{L} \frac{de}{dt} = \frac{1}{1+e} \frac{de}{dt} = \frac{\dot{e}}{1+e} \quad (2.26)$$

For constant crosshead speed the true strain rate will decrease as the specimen elongates.

A general relationship between flow stress and strain rate, at constant strain and temperature is

$$\sigma = C(\dot{\epsilon})^m|_{\epsilon, T} \quad (2.27)$$

Where **m** is known as **strain rate sensitivity**, the exponent **m** can be obtained from the slop of a plot $\log \sigma$ vs. $\log \dot{\epsilon}$ (**Fig. 2.12**). Strain rate sensitivity is quite low (<0.1) at room temperature for metals, whereas **m** increases with temperature especially at temperature above half of the absolute melting point. In hot-working condition **m** values are around 0.1 to 0.2.

2.2.6 Effect of temperature on tensile flow properties

The stress-strain flow behaviour and fracture properties derived from the tension test are strongly dependent on the temperature. In general, strength decreases and ductility increases as the temperature increased. Certain structural changes such as precipitation, strain aging or recrystallization may occur in certain temperature range to alter this general behaviour. Thermally activated processes influence the deformation and reduce strength at elevated temperatures.

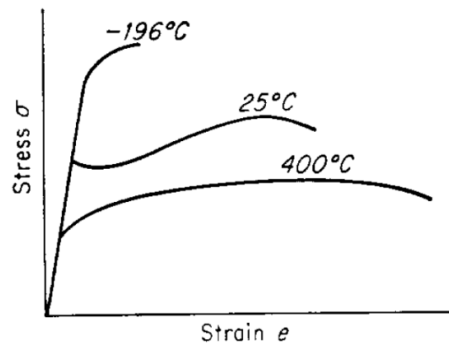


Fig. 2.13: Changes in stress-strain curve with temperature [34]

From **Fig 2.13**, it can be learn that with increase in temperature there is a drastic change in yield stress. The variation of yield stress with temperature is more sensitive in BCC metals than FCC metals, for BCC metals the yield stress increases rapidly with decreasing temperature, whereas for FCC metals the yield stress slightly temperature dependent than ultimate tensile strength. In FCC metals flow stress may not be much dependent on temperature, however strain hardening exponent (n) decreases significantly with increase in temperature. It is also clearly understood that the tensile strength is more temperature dependent than the yield strength.

2.2.7 Tensile fractures

Tensile fracture can be either shear mode of ductile or dimple mode of brittle fractures subjected to applied stress and temperature. Ductile and brittle are terms describe the amount of macroscopic plastic deformation that material experience before fracture. In ductile manner material shows reasonable plastic deformation while fracturing (**Fig 2.14**). Ductile fracture in most materials appears a gray, fibrous and is classified on a macroscopic scale as either fibrous or shear fracture. Brittle fractures are characterized by rapid crack propagation with less expenditure of energy than with ductile fractures and without appreciable gross plastic deformation (**Fig 2.14**). Brittle tensile fracture has a bright, granular appearance and exhibits little or no necking. They are generally of the flat type, that is, perpendicular to the direction of the tensile stress. Microscopic level observation reveals that ductile fractures are those that occur by micro-void formation and coalescence, whereas brittle fractures may occur by either transgranular or intergranular cracking **[31]**.

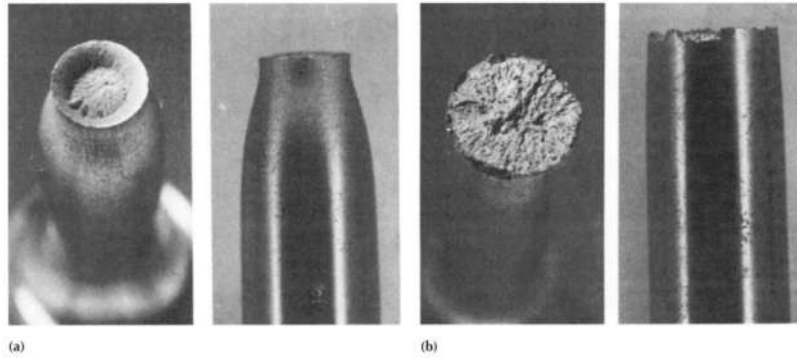


Fig. 2.14: Appearance of (a) ductile and (b) brittle tensile fractures [31]



Fig. 2.15: Typical cup-cone fracture appearance of un-notched tensile specimen [32]

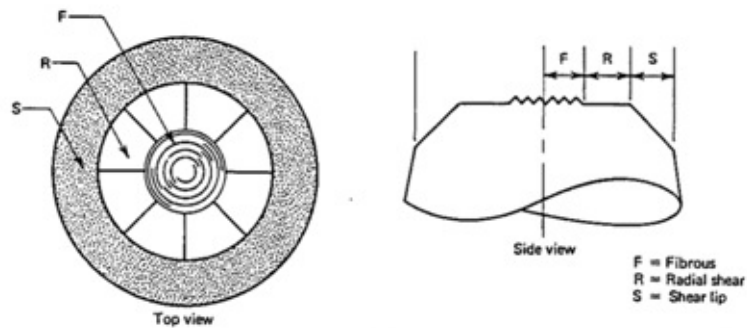


Fig. 2.16: A schematic representation of shear lip zone, top and side view [32]

In general, the tensile tested samples exhibits typical cup and cone type fractures as shown in **Figs. 2.14** and **2.15**, and the cup and cone fracture clearly exhibits three zones: the inner flat fibrous zone where the fracture begins, an intermediate radial zone where fracture propagates, and outer shear lip zone where the fracture terminates. The schematic representation as shown in **Fig. 2.16** clearly reveals shear lip zone from top and side view. The mechanism which is responsible for the

formation of typical cup and cone fracture in tensile tested specimens is based on the tri-axial state of tensile stress within necked region causes initiation of micro-voids near to the small particles within the microstructure. These micro-voids gradually grow and gets coalescence causes an internal, disk shaped crack orientated normal to the applied stress axis. Final fracture then occurs by a shearing-off process along a conical surface oriented 45° to the stress axis. This entire process produces the classical cup-cone fracture surface appearance as shown in **Figs. 2.14** and **2.15**.

2.2.8 Dynamic strain ageing (DSA)

Dynamic strain ageing occurs as a metal is deformed. It is manifested by serrated stress-strain curves and stretcher strains. The serrated stress-strain curves are characterized by sudden load drops that correspond to bursts of plastic deformation, followed by load drops and elastic reloading until another burst of deformation occurs. The phenomenon of dynamic strain ageing arises in many engineering metals and alloys subjected to certain temperature and strain rate conditions. Dynamic strain ageing is the phenomenon occurs due to the interaction of solute atoms with moving dislocations. It is like a static strain ageing in that it takes a greater force to initiate plastic deformation by dislocations breaking free of solutes than to cause them to move once they are free. The difference is that dynamic strain ageing occurs at a certain temperature and a strain rate that allows the solute atoms to pin the dislocations again while the material is deforming. The result is that the stress-strain curve consists of a series of load drops occurring during the deformation followed by elastic reloading until the stress is high enough to reinitiate deformation. Apart from serrated flow, the other manifestation to the occurrence of DSA caused peak/plateaus in flow stress variation with temperature, negative strain rate sensitivity on flow stress, minimum in ductility and change in fracture mode.

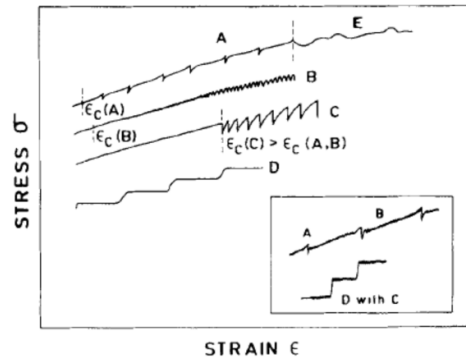


Fig. 2.17: Types of serrations observed during tensile deformation [37]

Five types of serrations are observed in materials due to dynamic strain ageing (DSA) they are classified as Type A, B, C, D and E [37]. Type-A serrations are periodic serrations from repeated deformation bands initiating at the same end of the specimen and propagating in the same direction along the gauge length. These are considered as locking serrations, characterized by an abrupt rise followed by a drop to below the general level of the stress-strain curve. They occur in the low temperature and high strain rate conditions.

Type-B serrations are oscillations about the general level of the stress-strain curve occur in quick succession due to discontinuous band propagation arising from the DSA of the moving dislocations within the band. Type-B serrations often develop from those of Type-A with increase strains (Fig. 2.17) or occurs at the onset of serrated yielding at high temperature and low strain rate conditions.

Type-C serrations are yield drop occurs below the general level of the flow curve and are therefore considered to be due to dislocation unlocking. This type of serrations takes place at higher temperatures and lower strain rates.

Type-D serrations are plateaus in the stress-strain curve due to band propagation similar to Luders band with no work hardening or strain gradient ahead of the moving band front. Like Type-A serrations, they can occur alone or with Type-B serrations during the band propagation (Fig. 2.17).

Type-E serrations are generated from Type-A serrations at high strains. Type-E serrations are similar to Type-A serrations, but with little or no work hardening during band propagation. For

the onset of serrations in substitutional alloys, a critical strain ϵ_C is required. The ϵ_C value is dependent on both strain rate ($\dot{\epsilon}$) and the temperature (T). In general, at high strain rates and low temperatures Type-A or B serration are observed whereas at high temperatures and low strain rates Type-C are observed (Fig. 2.17). Various investigators have reported on dynamic strain ageing in metals and alloys such as austenitic stainless steel, titanium, aluminum alloys and ferritic steel [38-44].

2.2.9 Strain or Work hardening behaviour

Work hardening also known as strain hardening or cold working, is the term used to describe the phenomenon that most metals become stronger and harder when plastically deformed [31-36]. This strengthening process occurs because of multiplication of dislocations by generation and restriction of dislocation movement by interaction of other dislocations as well as particles such as precipitates within the crystal structure of the material. Work hardening may be desirable or undesirable depending on the context. An example of desirable work hardening is that which occurs in metalworking processes that intentionally induce plastic deformation to cause a shape change. These processes are known as cold working or cold forming processes. In other side work hardening process develops undesirable cracks or voids and makes material hard to machining results tool material would break. Certain alloys are more prone to this than the others; super-alloys such as Inconel require machining strategies that takes in to account. Mathematical equations are proposed by various investigators to explain the work hardening behaviour material in the uniform elongation region from engineering stress-strain curve. The parameters derived from these equations can explain microscopic changes during deformation. The various equations are explained below.

2.2.10 Tensile constitutive material modeling

In order to describe plastic behaviour of materials in uniform elongation region, flow curves of metals are usually described by mathematical expressions. Constitutive flow equations have been developed and described by several investigators to predict the experimental true stress–strain curve of materials. The different constitutive equations are explained below.

Hollomon:

Hollomon [50] proposed a simple power law relation interrelating true stress (σ)–true plastic strain (ϵ) in the uniform plastic elongation regime as

$$\sigma = K_H \epsilon^{n_H} \quad (2.28)$$

where n_H is the strain hardening exponent and K_H is the strain hardening coefficient. Hollomon relation provides a measure of uniform elongation and ultimate tensile strength through n_H and K_H , respectively (Fig. 2.18).

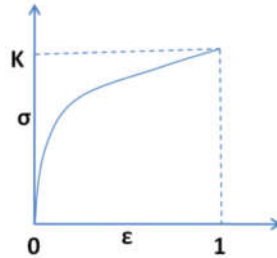


Fig. 2.18: Graphical representation of Hollomon equation at $\epsilon=1$

Ludwik

For materials exhibiting varied yield strength and similar strain hardening behaviour or in case of material exhibiting similar yield strength with different work hardening behaviour, the yield and strain hardening cannot be described by the same process as specified in Eq. (2.19). This invokes the necessity for introducing mechanical history as an additional term to the above power law. The mechanical history mainly comes from material processing and fabrications method such as cold working.

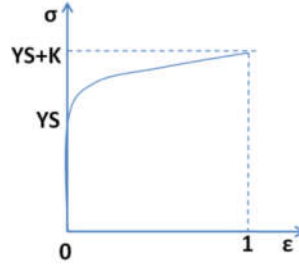


Fig. 2.19: Graphical representation of Ludwik equation at $\varepsilon=1$

In order to account for mechanical history in the flow relationship, a stress term (σ_0) or a strain term (ε_0) was added in **Eq. 2.19**. As shown in **Fig. 2.19** addition of stress term, (σ_0) for accounting the positive stress deviation owing to yielding at low strains was proposed by Ludwik **[45]** as

$$\sigma = \sigma_0 + K_L \varepsilon^{n_L} \quad (2.29)$$

Where n_L is the strain hardening exponent and K_L is the strain hardening co-efficient.

Swift

Swift **[46]** proposed a relationship with the addition of strain term ε_0 accounting for the pre-strain (**Fig. 2.20**) left in the material as

$$\sigma = K_s (\varepsilon_0 + \varepsilon)^{n_s} \quad (2.30)$$

Where n_s and K_s are the strain hardening exponent and co-efficient respectively in Swift relationship

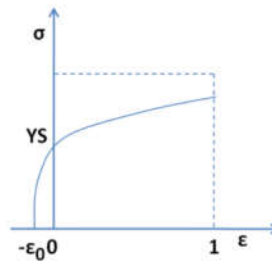


Fig. 2.20: Graphical representation of Swift equation at $\varepsilon=1$

Ludwigson

Ludwigson [47] demonstrated that the true stress–true plastic strain behaviour of many face centered cubic (FCC) metals and alloys having low stacking fault energy cannot be described by simple Hollomon equation alone due to large positive stress deviation at low strains. He proposed that the positive stress deviation at low strains can be overcome by an additional term as (Fig. 2.21)

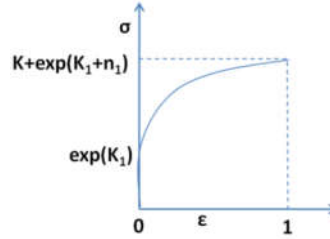


Fig. 2.21: Graphical representation of Ludwigson equation at $\epsilon=1$

$$\sigma = K_1 \epsilon^{n_1} + \exp(K_2 + n_2 \epsilon) \quad (2.31)$$

Where K_1 and n_1 are the same as described in Hollomon equation [2.28], and K_2 and n_2 are additional constants.

Voce

The strain hardening law interrelating true stress (σ) and true plastic strain (ϵ) proposed by Voce is expressed as (Fig. 2.22)

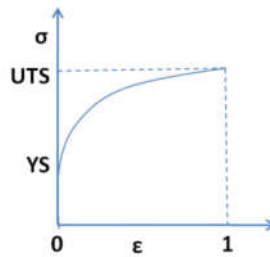


Fig. 2.22: Graphical representation of Voce equation at $\epsilon=1$

$$\sigma = \sigma_s - (\sigma_s - \sigma_l) \exp \left[\frac{-(\epsilon - \epsilon_l)}{\epsilon_c} \right] \quad (2.32)$$

Where σ_s is the saturation stress; σ_i and ε_i are true stress and true plastic strain at the onset of plastic deformation, respectively and ε_c is a constant. Above equation reduce as

$$\sigma = \sigma_s - (\sigma_s - \sigma_i) \exp(n_v \varepsilon) \quad (2.33)$$

For initial plastic strain $\varepsilon_i=0$, with three constants σ_s , σ_i , and $n_v = -1/\varepsilon_c$.

According to Voce [48, 49] the σ_i related to yield stress and saturation stress σ_s is the asymptotic stress value attained after severe deformation. Therefore, σ_s is expected to be close to the value of ultimate tensile strength. The n_v parameter defines the rate at which the stress from its initial value tends to reach steady state value or saturation stress value.

2.3 Analytical Frame work

Ludwigson approach

Several constitutive relationships have been proposed for the description of tensile deformation and work hardening behaviour of materials ranging from pure metals to complex engineering alloys. Among the relationships, a simple power law interrelating true stress (σ)–true plastic strain (ε_p) proposed by Hollomon [50] is represented as

$$\sigma = K_H \varepsilon_p^{n_H} \quad (2.28)$$

Where n_H is the strain hardening exponent and K_H is the strain hardening coefficient. However, as discussed earlier, the deformation behaviour of face centered cubic (FCC) metals and alloys with low stacking fault energy cannot be described completely by single Holloman equation due to a large positive stress deviation at low strains. Ludwigson [47] suggested a simple modification by introducing an additional term ‘ $\exp (K_2 + n_2 \varepsilon_p)$ ’ in the Hollomon relationship in order to account for the positive stress deviation at low strains, as

$$\sigma = K_1 \varepsilon_p^{n_1} + \exp(K_2 + n_2 \varepsilon_p) \quad (2.31)$$

where K_1 and n_1 are equivalent to K_H and n_H in **Eq. (2.28)**, respectively. K_2 and n_2 are the additional constants. It is important to note that the term ‘ $\exp(K_2)$ ’ is a finite true stress at zero plastic strain representing proportional limit of the material. Low stacking fault energy FCC metals and alloys exhibits predominantly planar slip at low strains and this gives rise to large positive stress deviation in stress and plastic strain flow curves. In contrast at high plastic strain the material deforms by multiple slip and cross-slip leading to linear stress-strain behaviour. The description of later can be readily represented by simple Hollomon [**Eq. 2.28**]. However, the description at low plastic strains requires Ludwigson equation [**Eq. 2.31**]. At high temperatures, it must be mentioned that the Ludwigson relation reduces to simple power law i.e., Hollomon equation [**Eq. 2.28**] as a result of the absence of significant stress deviations in σ - ε_p data at low strains.

Voce approach

For materials showing saturation in σ - ε_p data, Voce [48] proposed a relationship in terms of the increase in flow stress from its initial value to the steady-state or saturation value through a rate constant. Voce equation has provided significant attention in view of sound interpretation proposed by the Kocks–Mecking. The true stress (σ) and true plastic strain (ε) behaviour of many metals and alloys are adequately described by the strain hardening power law proposed by Voce [49] as

$$\sigma = \sigma_s - (\sigma_s - \sigma_I) \exp\left[\frac{-(\varepsilon - \varepsilon_I)}{\varepsilon_c}\right] \quad (2.32)$$

Where σ_s is the saturation stress, σ_I and ε_I are the true stress and the true plastic strain at the onset of plastic deformation respectively, and ε_c is the constant. For condition $\varepsilon_I=0$, equation (2.32) reduces to

$$\sigma = \sigma_s - (\sigma_s - \sigma_I) \exp(n_v \varepsilon) \quad (2.33)$$

with constants σ_s , σ_I and $n_v = -1/\varepsilon_c$. n_v is represented as the rate of stress which tends to reach the steady state value.

Kocks–Mecking phenomenological approach

Kocks and Mecking proposed a phenomenological approach to macroscopic plasticity of metals that appears very useful in describing plastic flow in different modes of continuous deformation [51, 52]. Kocks–Mecking (K–M) model is capable of predicting the creep behaviour of a material from its work hardening behaviour. The approach is based on the assumption that the kinetics of plastic flow is determined by a single structural parameter called stress (σ). The dependence of the flow stress on the plastic strain rate $\dot{\epsilon}$, and the absolute temperature T at a given structure of the material is given by the kinetic equation;

$$\sigma = \sigma(\sigma, \dot{\epsilon}, T), \quad (2.34)$$

For a complete description of plastic flow behaviour the kinetic equation is equilibrated with an evolution equation which describes the variation of the structure parameter (σ) with strain (ϵ) at a given strain rate ($\dot{\epsilon}$) and temperature (T);

$$\frac{d\sigma}{d\epsilon} = f(\sigma; \dot{\epsilon}, T) \quad (2.35)$$

According to K–M model as the deformation progress, the structure parameter σ evolves towards saturation value σ_s , since the quantity of σ_s is a function of strain rate ($\dot{\epsilon}$) and temperature (T). In the philosophy of the K–M model the entire stress–strain curve can be viewed as a ‘transient’ of the flow stress from some initial value to the saturation value corresponding to some equilibrium structure at given strain rate ($\dot{\epsilon}$) and temperature (T). In the present K–M model [51, 52], the work hardening behaviour in metals and alloys is conveniently described using the variations of instantaneous work hardening rate ($\theta = d\sigma / d\epsilon$) with the flow stress σ . Accordingly at constant strain rate the evolution of dislocation structure with strain is assumed as a single structural parameter responsible for plastic flow. The work hardening is controlled by the competition between storage and annihilation (rearrangement) of dislocations, which are assumed to

superimpose in an additive manner. Therefore, decrease in instantaneous work hardening rate θ with increasing true stress σ in the linear stage–III work hardening is shows as;

$$\theta = \theta_0 \left(1 - \frac{\sigma}{\sigma_s} \right) \quad (2.36)$$

where θ_0 is the initial work hardening rate and σ_s is the saturation stress at high strains corresponding to condition where instantaneous work hardening rate is equal to zero, i.e. $\theta=0$. In the simplified K–M model [51, 52] the mean free path of gliding dislocations is assumed to be solely determined by localised obstacles associated with dislocations. In the extension of this model, other geometrical obstacles to dislocation glide such as grain boundaries, particles of a second phase, etc. are considered. However, in the present investigation, it is assumed that one internal variable model of total dislocation density evolution is assumed to be the governing structural parameter defining the course of deformation. The slope of θ – σ linear plot (Fig. 2.23) in stage–III is a measure of the rate at which work hardening decreases with stress to steady state or saturation stress value. The value of the slope of θ – σ plot also represents equivalence to constant n_v obtained from the description of true stress–true plastic strain behaviour using Voce equation (Eq. (4.4)). The differential form of Voce relation can be described as

$$\theta = -\sigma_s n_v \left(1 - \frac{\sigma}{\sigma_s} \right) \quad (2.37)$$

From the analogy between equations (2.33) and (2.36), θ_0 can be evaluated from work hardening parameters obtained using Voce equation as

$$\theta_0 = -n_v \sigma_s \quad (2.38)$$

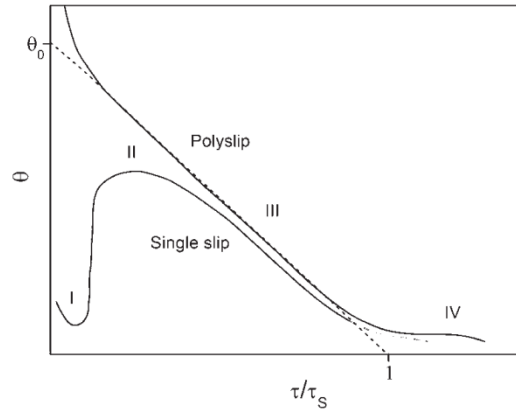


Fig. 2.23: Schematic representation of variation of work hardening rate with normalised shear stress shows various stages of work hardening in single crystal and poly crystals. The dotted line represents the stage-III hardening obeying K–M approach. $\theta_{0,K-M}$ is obtained as $\theta = \theta_{0,K-M}$ at $\sigma = 0$

2.4 Motivation of the study

Most of the Cr–Mo ferritic steels have been used as steam generator pipe and tube applications in thermal and nuclear power plants at different stress and temperature conditions. Ferritic steels have shown superior mechanical properties and good thermal conductivity at high temperature applications as compare to austenitic stainless steel. However, each grade of steel has its own limitations to perform intended responsibilities within the limits of stress and operating temperature range. P91 steel has excellent thermo physical properties as compared with previous versions, whereas it has limited resistance to type-IV cracking in weldments during deformation at high temperature. Studies confirmed that boron added steel has excellent resistance to type-IV cracking. Accordingly boron alloyed P91 steel was developed. The study of the high temperature mechanical behaviour is necessary to understand thermal assisted mechanical and metallurgical changes in the alloy. The tensile flow and work hardening behaviour of boron added P91 steel data has limited availability in the scientific community. All these factors stimulate the enthusiasm to carry out the studies on tensile stress strain and work hardening behaviour of boron added P91 steel.

Chapter 3 : EXPERIMENTAL DETAILS

3.0 Material Composition and Heat Treatment

The material used in this investigation is boron added P91 steel supplied by the M/s. MIDHANI (Mishra Dhatu Nigam Ltd.), Hyderabad, in the form of 12 mm thick rolled plates. This is the first experimental trail heat material developed for the optimization of boron content in P91 steel to study the improvement in type-V cracking resistance in the weldments. The nominal chemical composition of first trail heat boron added P91 steel is shown in **Table-3.1**.

Table-3.1: Nominal chemical composition of boron added P91 steel

Elements (% wt.)	C	Si	Mn	S	P	Ni	Al	Ti	Cr	Mo	V	N	B	Fe
Boron added P91 steel	0.1	0.4	0.3	0.002	0.05	0.02	0.03	0.03	8.5	1.04	0.09	0.0021	0.01	Bal

The steel was obtained in mill annealed condition. Specimen blanks of dimensions $70 \times 12 \times 12$ mm were cut from the 12 mm thick plate in the rolling direction. The specimen blanks were given normalizing and tempering heat treatments. The normalizing was carried out at 1338 K for 2 hr. followed by air cooling. Tempering treatment was done at 1053 K for 2 hour followed by air cooling.

3.1 Tensile specimen geometry and test conditions

The heat treated specimen blanks were machined to 10 mm diameter rods with rolling direction parallel to the length of the rod. The tensile specimens have been fabricated as per **ASTM E8/E8M** standard [53]. **Fig. 3.1** shows the standard geometry of round tensile specimen. Specimens with 25 mm gauge length and 5 mm gauge diameter were used for testing. The tensile tests were conducted at three different strain rates of $1.26 \times 10^{-3} \text{ s}^{-1}$, $3.16 \times 10^{-4} \text{ s}^{-1}$, and $3.16 \times 10^{-5} \text{ s}^{-1}$ in the temperature range of 300 K to 873 K.

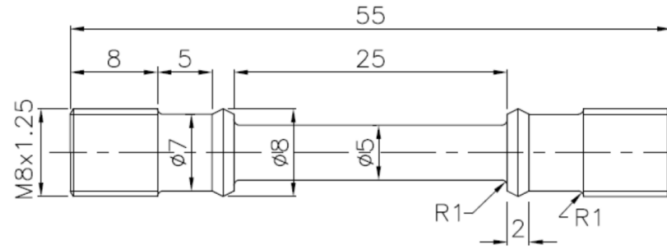


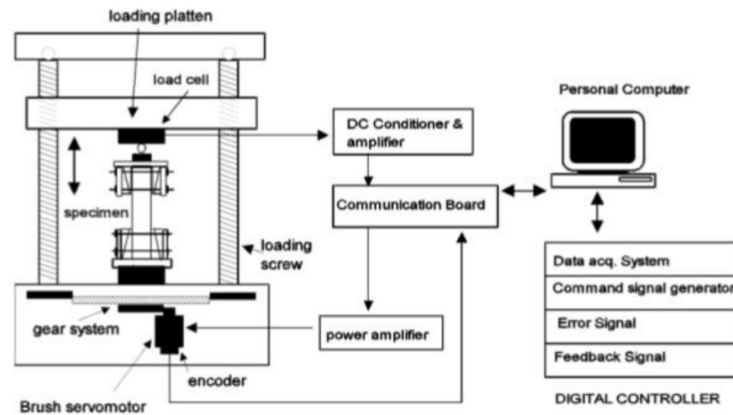
Fig. 3.1: The Geometry of tensile specimen (all dimensions are in mm)

3.2 Tensile testing equipment

The tensile tests were carried out on Hung ta-2402 material testing machine (**Fig. 3.2a**) equipped with a three-zone temperature control furnace and computer to control the testing. Schematic diagram of tensile test machine shows different parts of machine such as load cell, gear system, amplifier and digital controller (**Fig. 3.2b**). Load cell measures the load on specimen and magnitude of load depends on the material. Gear system optimizes the cross head speed of machine. Digital controller takes the feedback and gives the command to the other parts of the machine. Since no strain gauges or extensometers were employed the specimen extension was taken to correspond to the cross head movement. The maximum operating temperature of furnace is 1000° C. K-type thermocouple was used to monitor the exact temperature of the testing specimen. The specimen was held considerable amount of time at test temperature to ensure uniform distribution of temperature along the specimen within $\pm 2^{\circ}$ C.



(a)



(b)

Fig. 3.2: (a) Hung ta-2402 tensile machine and (b) schematic representation of different parts of screw driven tensile machine

3.3 Metallographic examination

The samples of boron added P91 steel in normalized and tempered condition were examined under optical microscope for basic microstructural features and fracture surfaces were observed under scanning electron microscope (SEM).

3.4 Sample preparation for optical microscopic studies

Polishing and Etching:

Samples for optical metallographic examination were prepared from longitudinal section cut along the direction of rolling. The mounted specimen was polished on a series of silicon carbide emery papers (coarse polishing) containing successively finer abrasives (100 to 1200 grade). Fine polishing is then carried out by using diamond particle suspended solutions spread on rotating velvet bed. The final specimen surface possessed scratch free and mirror finish surface.

Etching was done using Villella's reagent (1 gm of picric acid + 5 ml conc. HCl + 100 ml ethyl alcohol) and metallurgical features were examined under Leica optical microscope.

3.5 Sample preparation for scanning electron microscopic (SEM) studies

The scanning electron microscopy is mainly used to

- ❖ Characterize the fracture surface of the failed specimen.
- ❖ Study the mode of fracture.

A thin piece of the specimen containing the fracture surface was cut and cleaned in an ultrasonic vibrator tank containing acetone to remove the oily substance and dust particles deposited on the fracture surface. The specimen was then dried and stored in a clean polythene cover. The fracture surface was then studied using scanning electron microscope.

Chapter 4 : RESULTS AND DISCUSSION

4.0 Introduction

In view of understanding the influence of boron on microstructural stability of 9% Cr steels and type-IV cracking resistance in the weldments, several high temperature tensile and creep data both for base and weldments have been reported for the boron added P91 steel. However, systematic investigation of tensile properties and work hardening behaviour of the boron added P91 steel with the low nitrogen content is yet to be established. In view of the above, in this chapter, the detail investigation pertaining to the effect of strain rate and temperature on tensile properties, and tensile stress–strain and work hardening behaviour of boron added P91 steel has been presented for the temperatures ranging from 300 K to 873 K at three different strain rates of $1.26 \times 10^{-3} \text{ s}^{-1}$, $3.16 \times 10^{-4} \text{ s}^{-1}$ and $3.16 \times 10^{-5} \text{ s}^{-1}$. In addition, the effect of dynamic strain ageing (DSA) on tensile behaviour of the steel has also been discussed elaborately. The experimental flow curves of boron added P91 steel at different temperatures and strain rates have been described using two important constitutive flow relationships proposed by Ludwigson [47] and Voce [48, 49]. The activation energy for dynamic recovery is calculated using the model proposed by Bergström and Hallén. Further, the analogy between Voce relationship and internal–variable model proposed by Kocks–Mecking has been derived. The variation of instantaneous work hardening rate (θ) with true stress (σ) at different temperature and strain rates has been studied in order to see the different stages of work hardening.

4.1 Tensile true stress and true plastic strain behaviour

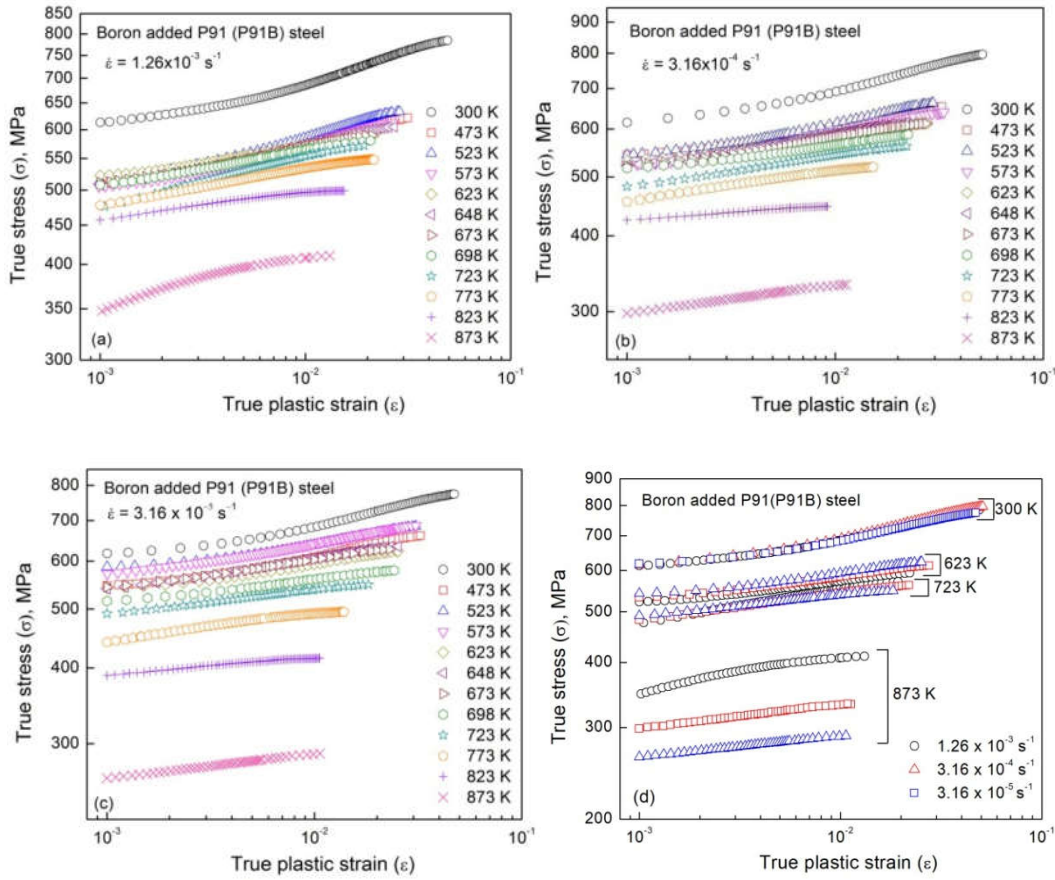


Fig. 4.1: True stress (σ)–true plastic strain behaviour of boron added P91 steel at the strain rates of (a) $2.16 \times 10^{-3} \text{ s}^{-1}$ (b) $3.16 \times 10^{-4} \text{ s}^{-1}$ (c) $3.16 \times 10^{-5} \text{ s}^{-1}$ and (d) effect of strain rate on true stress–strain behaviour.

The true stress and true plastic strain behaviour of boron added P91 steel at different temperature and strain rate conditions are shown in **Figs. 4.1a-d**. At all the experimental conditions the true stress and true plastic strain curves showed curvilinear behaviour at 300 K and intermediate temperature regime (473–698 K). Nearly linear behaviour in log–log plots of true stress–true plastic strain is noticed for the high temperature regime (723–873 K). For all the strain rate conditions, the true plastic strain or total uniform strain up to onset of necking shows a decrease in trend with increase in temperature. Both stress and strain values decrease

from room temperature followed by negligible decrease at intermediate temperature regime. The decrease in the values is more significant and rapid at high temperature regime (**Fig. 4.1a-d**). The effect of strain rate on the flow behaviour of the steel at three distinct temperature regimes can be seen by **Fig. 4.1d**. The true stress and true plastic strain data pertaining to low (300 K), intermediate (623 and 723 K) and high (873 K) temperature regimes were presented at all the strain rate conditions. The influence of strain rate on true stress and true plastic strain data is insignificant at 300 K. At intermediate temperatures, a marginal increase in flow stress values was noticed with decreasing strain rate which confirming the negative strain rate sensitivity in that regime. Systematic and rapid increase in flow stress values with increasing strain rate have been observed for 873 K. Moreover, at intermediate temperatures, serrated deformation behaviour was observed in the steel for the all strain rates. **Figure 4.2** reveals the Type-B and Type-D serrations for the strain rate of $3.16 \times 10^{-5} \text{ s}^{-1}$ at 523, 548 and 573 K. Type-B serrations are oscillations about the general level of the stress and strain curve that occur in quick succession due to discontinuous band propagation arising from the DSA of the moving dislocations within the band. Type B serrations often develop from those of type-A with increasing strain or occur at the onset of serrated yielding at high temperatures and low strain rates. Type-D serrations are plateaus in the σ - ϵ curve due to band propagation similar to Luders band with no work hardening or strain gradient ahead of the moving band front. Like type-A serrations, they can occur alone or with type-B serrations during the band propagation. It is believed that serrations in stress-strain curves are considered as one of the important manifestations of dynamic strain ageing. Other significant manifestations usually observed are (i) a peak in the variation of stress with temperature (ii) a peak in the variation of the work hardening θ with temperature, (iii) a peak in the variation of the Hall-Petch slope K with

temperature (iv) a minimum in the variation of the ductility with temperature and (v) negative strain rate sensitivity etc. [37].

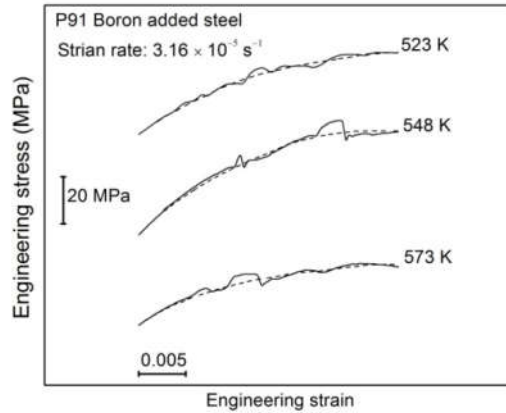


Fig. 4.2: Engineering stress versus Engineering strain curves of boron added P91 steel at the strain rate of $3.16 \times 10^{-5} \text{ s}^{-1}$ shows different types of serrations.

4.2 Variations of tensile properties with temperature and strain rate

The tensile properties such as yield strength, ultimate tensile strength, percentage elongation to fracture and percentage reduction in area have significant considerations in the design of engineering components. It is very important to emphasize that the examination of these basic properties as function of temperature and strain rate is certainly critical in order to qualify the material for intended use. The variation of shear modulus compensated tensile properties with temperature is shown in **Fig. 4.3a-b** and **Fig. 4.4a-b** respectively. The shear modulus (μ) values reported for plain 9Cr-1Mo steel in French nuclear code RCC-MR has been taken directly for boron added P91 steel also [55]. Both normalized strength parameters of yield and ultimate tensile strength with temperature decreased with increase in temperature for all strain rate conditions. The decrease in both the properties is found to be rapid in higher temperature regime (723–873 K) and gradual at lower temperature regime (300–473 K). Whereas, the extent of decrease in yield and tensile strength was found to be significantly lower

in intermediate temperature region (473–698 K) at all the strain rates. The strain rate dependence of yield strength and ultimate tensile strength revealed minor variations at 300 K followed by an increase in values with decreasing strain rate at intermediate temperatures, which is designated as phenomenon of negative strain rate sensitivity. This negative strain rate sensitivity is considered as one of the manifestations of occurrence of dynamic strain ageing (DSA).

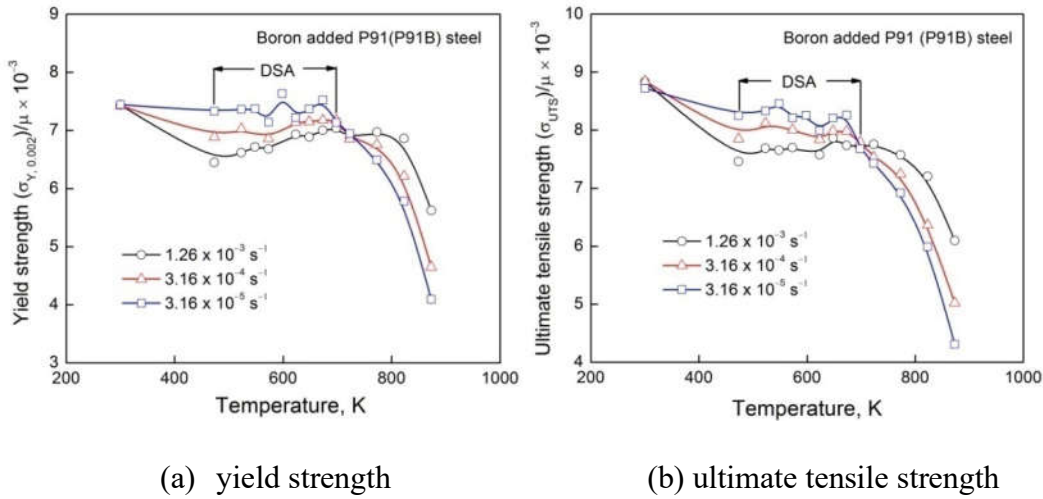


Fig. 4.3: The variation of (a) yield strength and (b) ultimate tensile strength with temperature for all strain rates of boron added P91 steel.

Dynamic strain ageing is an important material phenomenon observed in many metals and alloys at different temperature and strain rate conditions. Dynamic strain ageing occurs due to dynamic interaction of dislocations with solute atoms results temporary arrest of moving dislocations during deformation which causes sudden rise in applied stress required for deformation to progress. Dynamic strain ageing depend mainly on two important parameters i.e., applied strain rate responsible for moving dislocations and temperature responsible for diffusion of solute atoms. The strengthening mechanism accountable for the strength of boron added P91 steel at room temperature is predominantly strain rate induced dislocation–dislocation interaction (DDI). As the temperature is so negligible for diffusion of

solutes for dislocation–solute interactions at room temperature, dislocation–dislocation interaction (DDI) is considered as the predominant strengthening mechanism. When the temperature increases, particularly at intermediate temperature regime the strengthening is due to a combination of dislocation–dislocation and dislocation–solute interactions. Though both interactions contribute to strengthening of material, the predominant strengthening mechanism at intermediate temperature regime is mainly due to dislocation–solute interaction (DSI) than dislocation–dislocation interaction (DDI). This dislocation–solute interaction is termed to be a leading mechanism responsible for the DSA phenomenon. Because of DSI mechanism the strength values are reflected to be high in DSA regime and the solute atoms responsible for DSI mechanism could be either substitutional or interstitial atoms depending on the applied temperature and strain rate conditions. It must be understood that at all temperatures the dislocation–precipitate interaction (DPI) strengthening mechanism is predominant, in which dislocation movement is restricted by precipitate density. The variation of tensile strength parameters with temperature exhibited higher values at room temperature because of DDI mechanism and DPI mechanism. As the temperature increase dislocation–dislocation annihilation (opposite dislocations on same slip plans) would have been taking place and causes decrease in strength values. At intermediate regime, strength values again increases because of DSA effect followed by rapid decrease at high temperature because of dynamic recovery due to either one or more combination of thermally activated dislocation motion by cross slip and climb, dislocation annihilation, coarsening of precipitates, intergranular cracking, sub–structure softening.

The variation of percentage elongation to fracture with temperature as shown in **Fig. 4.4a** that shows a gradual decrease in values from 300 K followed by ductility minima and

significant variations in values at intermediate regime (473–698 K) and rapid raise at high temperatures. Strain rate influence on percentage elongation to fracture observed to be nominal at all temperature regimes.

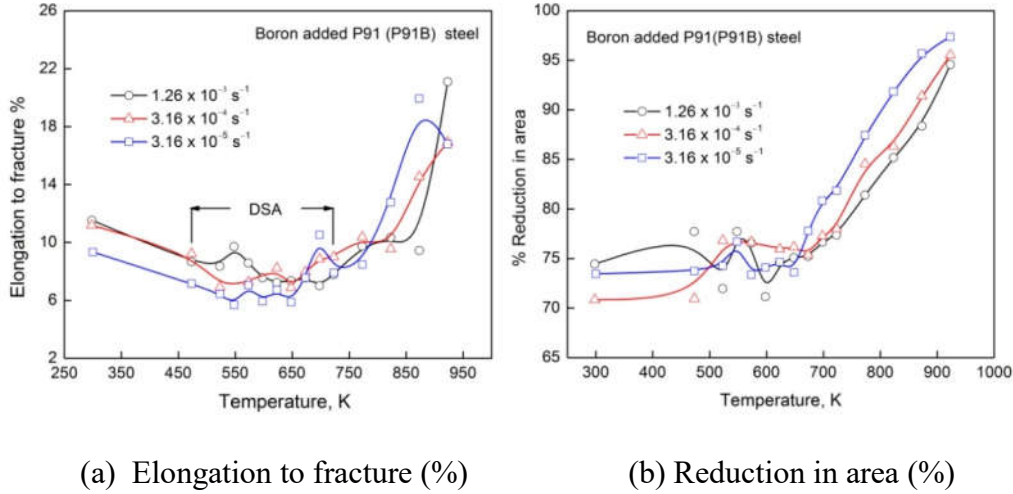


Fig. 4.4: The variation of (a) Elongation to fracture (%), and (b) Reduction in area (%) with temperature for all strain rates of boron added P91 steel.

The variation of percentage reduction in area with temperature shows a gradual rise from 300 K followed by considerable variations at intermediate regime and drastic rise at high temperatures. Strain rate dependence of percentage reduction in area displayed scattered variation at room and intermediate temperatures. At high temperatures, systematic decrease percentage reduction in area with increasing strain rate is noticed (**Fig. 4.4b**). The ductility minima along with the observed peaks/plateaus in the values of yield strength, ultimate tensile strength (**Fig.4.3a-b**) at intermediate temperature regime suggested the occurrence of dynamic strain ageing (DSA) phenomenon. The variations in percentage elongation to fracture and percentage reduction in area with temperature at all regimes (room, intermediate and high) reflected accordingly to the respective strengthening mechanisms operating for this steel.

It is mandatory for design engineers to validate any indigenously developed material by comparing its strength properties with the international data and codified design data in order

to confirm and achieve the confidence. **Figure 4.5a-b** shows the basic strength values of yield and ultimate tensile strength of boron added P91 steel in comparison with RCC–MR average design data as well as Japanese NIMS average design data reported plain P91 steel. As apparent from **Fig. 4.5a-b** that, at all temperature boron added P91 steel shows significantly higher strength values than the international average design data values reported for P91 steel.

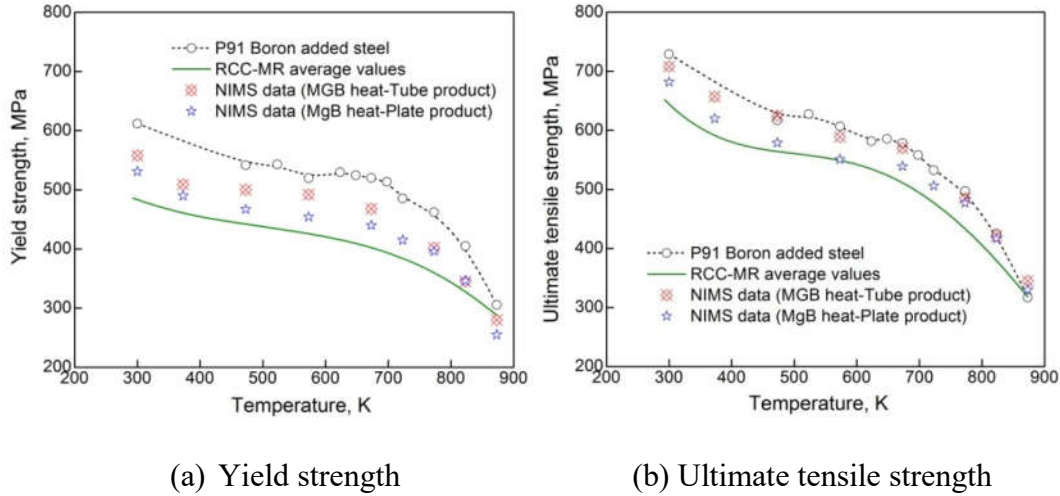


Fig. 4.5: The validation of (a) yield strength and (b) ultimate tensile strength values of boron added P91 steel data with average values of RCC–MR French design data and NIMS design data reported for P91 steel.

4.3 Modeling tensile flow behaviour of boron added P91 steel

In the present investigation, the experimental true stress and true plastic strain curves have been modeled with curve fitting using Ludwигson and Voce constitutive flow relationships presented in Section 2.3. Experimental true stress and true plastic strain data was curve fitted with flow relationship proposed by Ludwигson [47] and Voce [48, 49] through Eq. (2.31 & 2.33) using Levenberg–Marquardt (L–M) algorithm with unknown constants as adjustable parameters. The goodness of fit was evaluated using lower χ^2 value, i.e., the sum of square of

the deviations of the calculated stress values from the experimental stress values obtained for these relationships at different strain rate and temperature conditions.

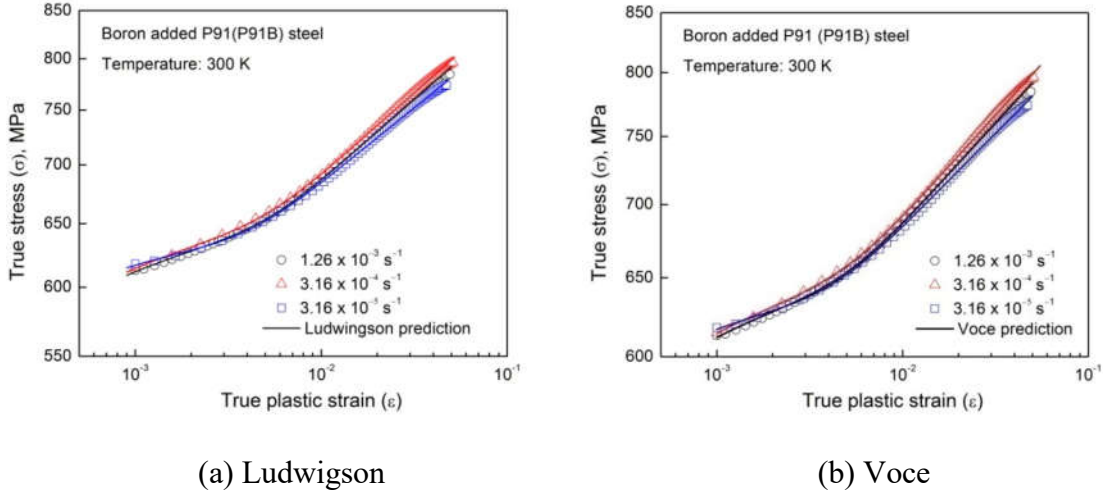


Fig. 4.6: True stress–true plastic strain data at temperature 300 K obeyed by (a) Ludwigson and (b) Voce with equal confidence for all strain rates of boron added P91 steel.

Typical experimental true stress–true plastic strain data long with the fitted Ludwigson and Voce flow relationships were shown at 300 K for all three strain rates in **Fig. 4.6a-b**. It is evident that both equations described the true stress and true plastic strain data adequately with equal confidence at all strain rates at 300 K as shown by perfect solid line. The χ^2 values obtained by both Ludwigson and Voce equation for all temperature and strain rates are shown in below **Table-4.1**. It can be understood clearly from these tables that except one or two temperatures, the remaining all temperatures showed χ^2 values very close to one or zero. It is also observed that by decrease in strain rate the values of χ^2 getting close to minimum value (close to zero) for all temperatures. It can be conclude finally that, both Ludwigson and Voce equations could closely describe the stress–strain behaviour of boron added P91 steel for all temperatures and strain rate conditions.

Table-4.1: Shows typical χ^2 values obtained by fitting experimental true stress and true plastic strain data with Ludwigson and Voce equations for all temperature and strain rate conditions.

Ludwigson			
SR	$1.26 \times 10^{-3} \text{ s}^{-1}$	$3.16 \times 10^{-4} \text{ s}^{-1}$	$3.16 \times 10^{-5} \text{ s}^{-1}$
T K	χ^2	χ^2	χ^2
300	1.734	1.927	2.067
473	0.615	0.801	0.239
523	1.162	0.553	0.325
573	0.571	0.885	1.285
623	0.123	0.278	0.409
648	1.867	0.568	1.143
673	0.371	0.529	0.58
698	0.915	0.101	0.323
723	2.588	1.133	0.523
773	2.168	0.038	0.028
823	0.008	0.068	0.034
873	2.841	0.089	0.042
923	0.007	0.511	0.523

Voce			
SR	$1.26 \times 10^{-3} \text{ s}^{-1}$	$3.16 \times 10^{-4} \text{ s}^{-1}$	$3.16 \times 10^{-5} \text{ s}^{-1}$
T K	χ^2	χ^2	χ^2
300	1.33	2.467	0.402
473	0.48	1.148	0.238
523	1.84	1.013	2.337
573	0.29	1.898	0.944
623	0.68	0.663	0.164
648	1.28	0.928	1.412
673	0.3	1.074	1.123
698	0.74	0.311	0.529
723	3.13	1.614	0.49
773	1.04	1.31	0.51
823	0.29	0.005	0.057
873	1.595	0.18	0.098
923	0.009	0.12	0.12

4.3 Variation of Ludwigson parameters with temperature and strain rate

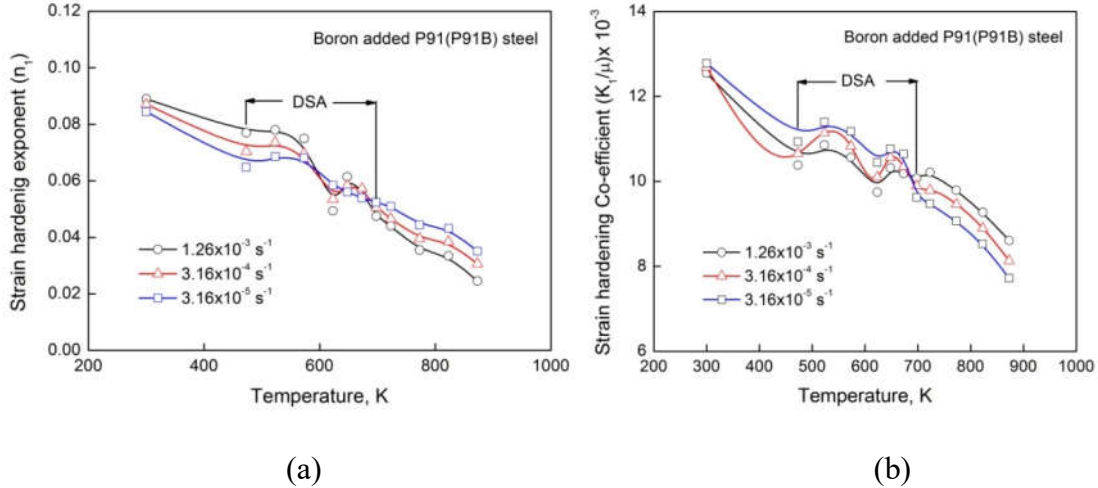


Fig. 4.7: The variation of (a) strain hardening exponent (n_1), and (b) normalized strain hardening co-efficient (K_1/μ) with temperature for all strain rates of boron added P91 steel.

The variations of strain hardening exponent (n_1) with temperature and strain rate is shown in **Fig. 4.7a**. The strain hardening exponent (n_1) represents the material ability to get harden while stressing. It is a structural parameter characterizes the property of uniform elongation. The

variation of strain hardening exponent (n_1) with temperature exhibited a gradual decrease from 300 K to 473 K followed by discernible peaks/plateau at intermediate temperature (473–698 K) and a rapid decrease at high temperatures (723–873 K). Strain rate influence on strain hardening exponent (n_1) at 300 K shows increase in values with increase in strain rate, whereas at intermediate temperatures n_1 displays a combination of plateau and peaks (473–698 K) and increase in the values with increase in strain rate up to 573 K followed by insignificant variations up to 698 K. However at high temperature n_1 values increase with decrease in strain rate. The negative strain rate sensitivity phenomenon on flow parameters at intermediate temperatures is explicitly observed in the variations of normalized strain hardening co-efficient (K_1/μ) with temperature at different strain rates as shown in **Fig. 4.7b**. The parameter K_1 is the strength factor at $\epsilon_p=1$. In order to account for the influence of temperature on the modulus and subsequently to bring out the influence of temperature on the strain hardening coefficient alone, modulus compensated strain hardening coefficient has been used. Temperature dependent shear modulus (μ) values reported for plain P91 steel were taken from French nuclear code RCC–MR [55]. Shear modulus compensated strength co-efficient (K_1/μ) exhibited a gradual decrease from 300 K to 473 K followed by discernible peaks and plateau at intermediate temperatures (473–698 K) and a rapid decrease at high temperatures for all strain rate conditions. Strain rate dependence K_1/μ increase with decrease in strain rate at room and intermediate temperatures, and a systematic decrease in K_1/μ with decreasing strain rate is observed at high temperatures. The additional term n_2 in Ludwigson relation is a constant and an inverse value of n_2 corresponds to the transient stage duration. The variation of additional constant n_2 with temperature exhibited a marginal increase in the value from 300 to 473 K followed by definite plateau at intermediate temperatures and rapid increase at high temperatures (**Fig. 4.8a**).

Influence of strain rate on n_2 has negligible effect at room and intermediate regime, however n_2 increases with increase in strain rate at high temperatures is observed. The term K_2 in Ludwigson relation corresponds to a finite stress at zero strain, and the value of $\exp(K_2)$ represents proportional limit of material. **Figure 4.8b** demonstrated the variations of $\exp(K_2)$ with temperature at different strain rates.

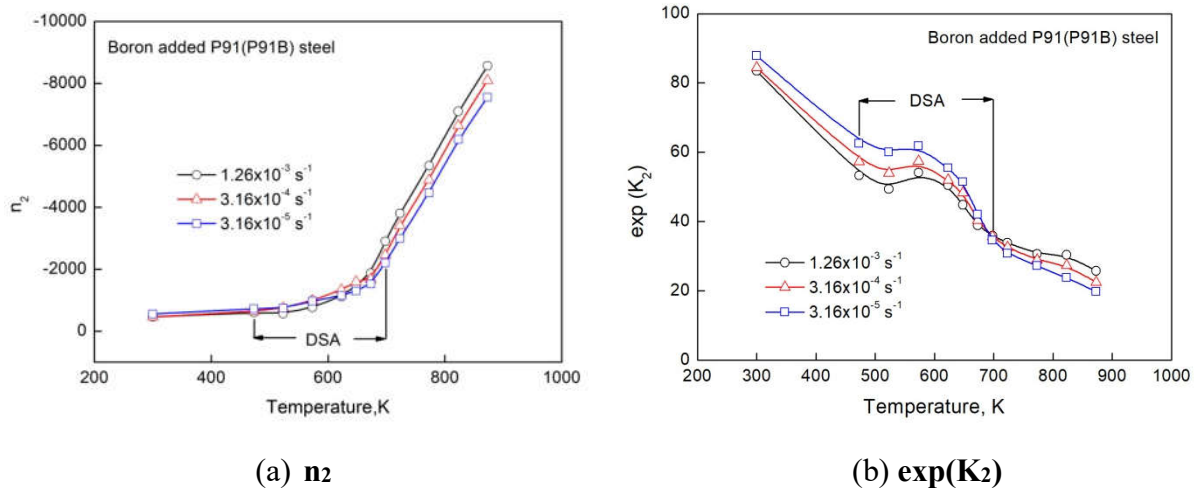


Fig. 4.8: The variation of (a) n_2 and (b) $\exp(K_2)$ with temperature for different strain rates of boron added P91 steel.

The values of $\exp(K_2)$ decrease gradually with increase in temperature from 300 K to 473 K followed by discernible plateau at intermediate temperatures and rapid decrease at high temperatures. Influence of strain rate displayed a decrease in $\exp(K_2)$ with increase in strain rate at room and intermediate regime, and increase in values with increase in strain rate at high temperatures. Ludwigson [47] suggested that deformation at low strains for true stress (σ)–true plastic strain (ϵ) data is predominantly dominated by planar slip in many FCC metals and alloys having low and medium stacking fault energy. At high strains, linear strain (σ)–strain (ϵ) data adequately represented by Hollomon equation [Eq. 2.28] corresponds to deformation dominated by cross-slip supported recovery mechanisms.

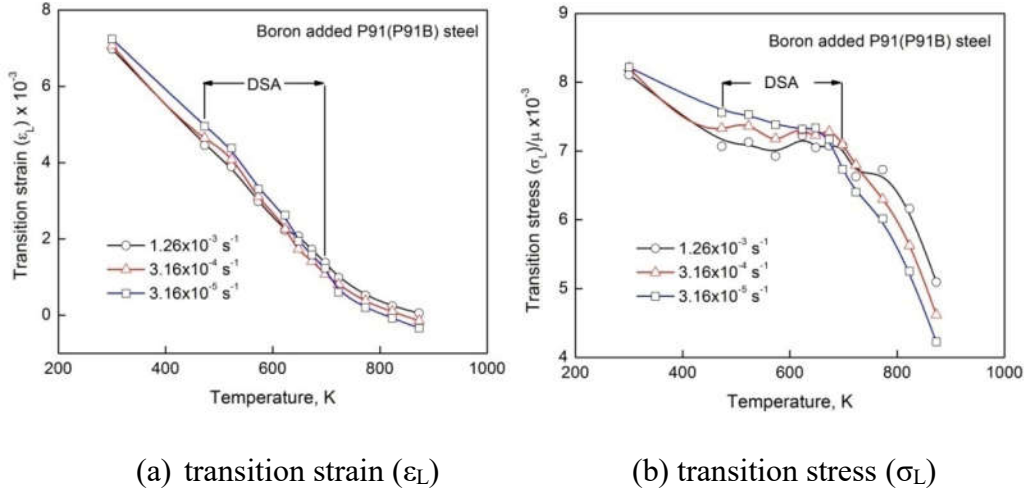


Fig. 4.9: The variations of (a) transition strain (ϵ_L) and (b) stress (σ_L) with temperature for different strain rates in boron added P91 steel.

The transition parameters such as σ_L and ϵ_L are suggests a point corresponding to both flow stress and strain at which a transition in plastic deformation mechanism change over from planar slip of dislocations to the multiple slip of dislocations. The transition strain, ϵ_L below which Holloman equation [Eq. 2.28] failed to represent stress (σ)–strain (ϵ) data at low strains and corresponding transition stress (σ_L) can be evaluated by setting the value of the ratio ‘r’ defined as

$$r = \frac{\exp(K_2 + n_2 \epsilon)}{K_1 \epsilon^{n_1}} = \frac{\Delta}{K_1 \epsilon^{n_1}} \quad (4.1)$$

to an arbitrary small value. In equation [4.1], Δ describes the positive stress deviations from the linear extrapolated Hollomon relationship i.e. $\sigma = K_1 \epsilon^{n_1}$ at low strain levels. For the estimation of ϵ_L values, ‘r’ value remains constant and it is set to 0.002 at all the conditions. The transition stress σ_L corresponding to ϵ_L is then calculated from same Eq. [4.1]. At all strain rates, the variation of transition strain (ϵ_L) with temperature as shown in Fig. 4.9a exhibited a continuous monotonic decrease, rather than peaks/plateau usually observe with increase temperature. It is clearly observed that the strain rate dependence of transition strain (ϵ_L) increase with decrease

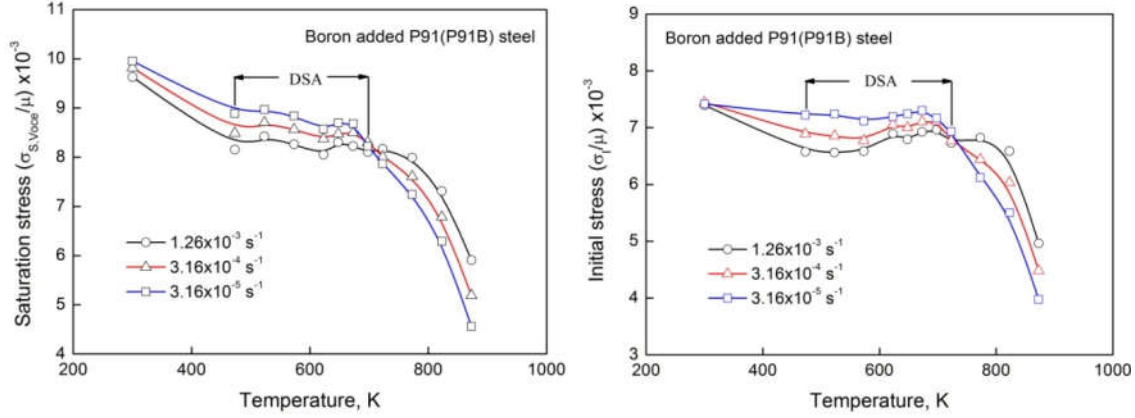
in the strain rate at room and intermediate temperatures and decreases with decreasing strain rate at high temperature. The variations in shear modulus compensated transition stress σ_L/μ , displayed a gradual decrease from 300 K followed by distinct peaks/plateaus at intermediate temperature and rapid decrease at high temperature (**Fig. 4.9b**). The values of σ_L/μ exhibited an increase with decrease strain rate at intermediate temperatures and a decrease with decreasing strain rate at high temperatures. It can be concluded from the observations of variations of Ludwigson parameters (n_1 , K_1/μ , n_2 , K_2/μ , σ_L , ϵ_L) with temperature exhibited three different temperature regimes of room (300K) intermediate (473–773K) and high temperature regimes (773–873K). Choudhary et al observed anomalous behaviour in the variation of Ludwigson parameters for 9Cr–1Mo steel at intermediate temperatures because of DSA effect [56]. In the present study, it is confirmed that most of the Ludwigson parameters derived for boron added P91 steel are closely sensitive to the DSA. Also in many alloy systems, it has been reported that DSA causes an increased rate of dislocation multiplication and a delay in recovery of dislocation structure [57–61]. It is well proven theory and observed in various alloys that DSA encourages the propensity towards uniform distribution of dislocations rather than cell structure formation [62–68]. Kashyap et al reported that uniform distribution of dislocations in the early stage deformation and cell structure having dense and thick cell walls in DSA regime for fine grain 316L SS [66, 68]. All these studies suggested that DSA has major influence in the variation of Ludwigson parameters at intermediate temperature regime and is the cause for reduced dynamic recovery. It has been proposed that the local solute mobility affects the rate of dynamic recovery by pinning dislocations giving rise to uniform dislocation distribution. At high temperatures, the rapid decrease in the flow parameters with decrease in strain rate and increase in temperature manifests the onset of recovery process implying early cross-slip and

climb of dislocations. This is also associated with a rapid decrease in flow stress, work hardening rate and uniform distribution of elongation [68, 69].

4.4 Variations of Voce and Kocks–Mecking parameters with temperature and strain rate

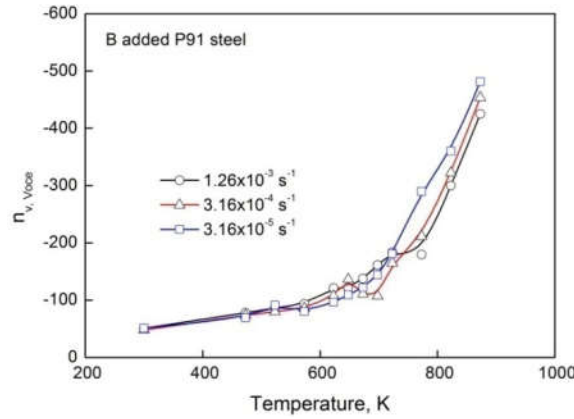
The variations of work hardening parameters, initial stress ($\sigma_{I,Voce}$), saturation stress ($\sigma_{S,Voce}$) and rate parameter $n_{V,Voce}$ obtained by Voce equation for boron added P91 steel with temperature and different strain rate conditions are presented in **Figs. 4.10a-c**. The initial stress ($\sigma_{I,Voce}$) basically represents the yield strength and saturation stress ($\sigma_{S,Voce}$) represents the UTS, and rate parameter $n_{V,Voce}$ represents the rate at which the stress reaches from its initial stress to saturation stress. The subscript ‘Voce’ refers to the work hardening parameters obtained by Voce equation and ‘K–M’ refers to the parameters obtained by Kocks–Mecking approach. Voce parameters such as shear modulus compensated initial stress ($\sigma_{I,Voce}/\mu$) and saturation stress ($\sigma_{S,Voce}/\mu$) exhibited distinct three temperatures regimes; a gradual decrease from 300 K to 473 K followed by clear peaks/plateau at intermediate temperatures (473–698 K) and rapid decrease at high temperatures (723–873 K) for all temperature and strain rate conditions (**Fig. 4.10a-b**). Since modulus and flow stress decreases with an increase in temperature, the modulus compensated initial stress ($\sigma_{I,Voce}/\mu$) and saturation stress ($\sigma_{S,Voce}/\mu$) are considered in order to bring out the influence of temperature on both the stresses. As earlier mentioned, the values of shear modulus (μ) reported for plain P91 steel at various temperatures have been obtained from French nuclear design code, RCC–MR [55] for boron added P91 steel. The variations of $\sigma_{S,Voce}/\mu$ with temperature exhibited three distinct temperature regimes of gradual decrease from 300 K to 473 K followed by well-defined peaks/plateau at intermediate temperatures, 473 K to 698 K and a rapid decrease in $\sigma_{S,Voce}/\mu$ at high temperatures. The influence of strain rate is

reflected to be more pronounced as plateaus/peaks in $\sigma_{S,Voc}/\mu$ at intermediate temperatures and a systematic decrease in $\sigma_{S,Voc}/\mu$ at high temperatures with decrease in strain rate (**Fig. 4.10a**).



(a) Saturation stress ($\sigma_{S,Voc}/\mu$)

(b) Initial stress ($\sigma_{I,Voc}/\mu$)



(c) n_V parameter

Fig. 4.10: The variations of (a) normalized initial stress (σ_I/μ), (b) normalized saturation stress (σ_S/μ) and (c) n_V parameter with temperature for different strain rates in boron added P91 steel.

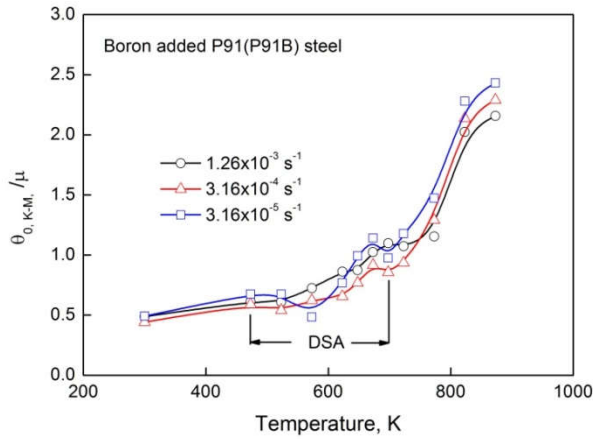
Normalized initial stress ($\sigma_{I,Voc}/\mu$) also been exhibited a gradual decrease from 300 K to 473 K followed by well-defined peaks/plateau in the range of 473 K to 698 K and a rapid decrease at high temperatures (**Fig. 4.11b**). Like $\sigma_{S,Voc}/\mu$, initial stress ($\sigma_{I,Voc}/\mu$) also displayed more pronounced plateaus/peaks and increase in the values with decrease in strain rate at intermediate temperatures. **Fig. 4.10c** shows the variations in n_V with temperature also been

exhibiting distinct three temperature regimes. A marginal increase in the absolute values of $n_{V,V_{oce}}$ at 300 K to 473 K followed by plateaus at intermediate temperatures and a rapid increase at high temperatures have been observed. Strain rate dependence $n_{V,V_{oce}}$ parameter exhibited insignificant variation at room and disorganized at intermediate temperature, followed by increase the values with decrease in strain rate at high temperatures.

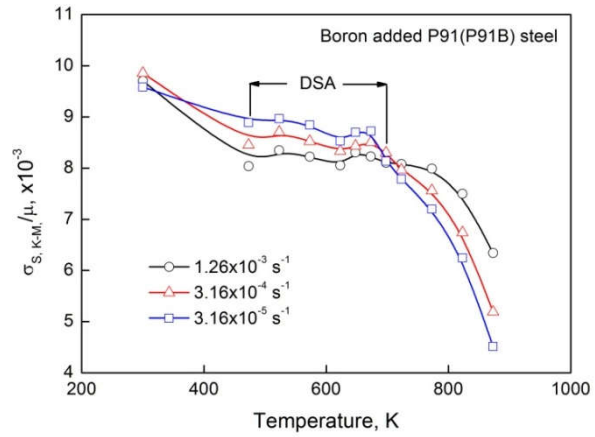
The occurrence of distinct peaks/plateaus rather than a monotonic decrease in $\sigma_{S,V_{oce}}/\mu$ and $\sigma_{I,V_{oce}}/\mu$ with increasing temperature, increase in $\sigma_{S,V_{oce}}/\mu$ and $\sigma_{I,V_{oce}}/\mu$ with decreasing strain rate and a marginal increase in $n_{V,V_{oce}}$ with increase in temperature indicate anomalous variations in work-hardening parameters at intermediate temperatures (**Fig. 4.10a-c**). The grouping of σ - ϵ data in a narrow band observed at intermediate temperatures (**Fig. 4.1a-d**) is exactly reflected in the anomalous variations in work-hardening parameters. This anomalous behaviour can be attributed to dynamic strain aging (DSA) as indicated by the occurrence of serrated flow at intermediate temperatures [70]. An analysis for the strain to onset of serrations in load-elongation curves and its dependence on strain rate and temperature yielded activation energy close to the diffusion of interstitial solute such as carbon in 9 % Cr ferritic steels [70-72]. Based on the value of activation energy, locking of dislocations could be the diffusing carbon suggested to be responsible for DSA in 9Cr-1Mo steel [70, 71]. Other manifestations of DSA obtained for the steel include peaks/plateaus in strength values, average work hardening rate, negative strain rate sensitivity on strength values and work-hardening rate, and ductility minima at intermediate temperatures. The influence of strain rate is reflected in a shift towards lower temperatures for the occurrence of peaks/plateaus in strength values and work-hardening rate and ductility minima with decreasing strain rate [56]. The phenomenon of DSA causes an increased rate of dislocation multiplication and delay in recovery of dislocation structure due

to reduced propensity to cross-slip [38, 57-59, 69]. A significant increase in dislocation density along with increased work-hardening index in the DSA temperature regime in P91 steel has been reported recently [56]. Also, the increased propensity towards uniform distribution of dislocations or poorly defined cell structure rather than well-defined dislocation cells has been reported in the DSA temperature regime for many alloy systems [62, 63, 66, 67]. It has been pointed out elsewhere that DSA tends to interfere with the normal tendency when worked to form dislocation cell structures, and this tendency of interference increases with increased propensity to DSA [56]. All these investigations indicate reduced dynamic recovery in the DSA regime arising from the diffusion of solutes, which affects the rate of dynamic recovery by pinning of dislocations and thereby preventing screw dislocation to cross-slip due to its reduced mobility. A detailed investigation on dislocation substructure indicated only a marginal increase in cell size with increasing temperature from 300 K to DSA temperature regime [66, 69]. A small decrease in $\sigma_{S,V_{0ce}}/\mu$ and $\sigma_{I,V_{0ce}}/\mu$ and a marginal increase in $n_{V,V_{0ce}}$ values from 300 K to those obtained in DSA temperature regime suggest that long range stress field due to dislocation multiplication and its interaction is expected to play a major role at room and intermediate temperatures [73, 74]. Rapid decrease in $\sigma_{S,V_{0ce}}/\mu$ and $\sigma_{I,V_{0ce}}/\mu$ (Figs. 4.10a-b) and a rapid increase in absolute $n_{V,V_{0ce}}$ (Fig. 4.10c) with increasing temperature indicate the acceleration of recovery processes at high temperatures. In addition to this, a systematic decrease in $\sigma_{S,V_{0ce}}/\mu$ and $\sigma_{I,V_{0ce}}/\mu$ and an increase in $n_{V,V_{0ce}}$ with decreasing strain rate also suggest the dominance of recovery processes at high temperatures. The occurrence of saturation stress in a flow curve has been interpreted by Mecking and Kocks [51] as a state of constancy in the dislocation density and its arrangement arising from the equilibrium between dislocation generation and annihilation until instability or necking sets in. A decrease in saturation stress (σ_s) with

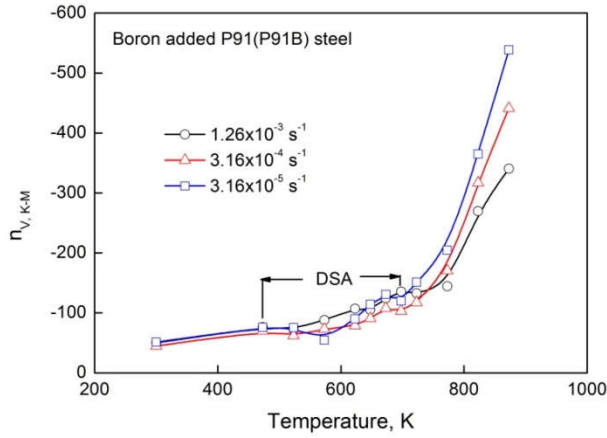
increasing temperature implies that steady state is reached at lower stresses. Apart from rapid decrease in flow stress with increasing temperature (**Figs. 4.1a-d**), the dominance of dynamic recovery at high temperatures has been demonstrated through a decrease in dislocation density, formation of well-defined sub-grains rather than dislocation cells, and rapid increase in the size of dislocation substructure with increasing temperature [66, 69]. A rapid increase in $n_{V,Voce}$ with increasing temperature can be ascribed to change in controlling deformation mechanism from cross-slip to climb of dislocations and sub-boundary migration at high temperatures. It has been reported that at low and intermediate temperatures, where cross-slip is dominant, $n_{V,Voce}$ is expected to have a low absolute value [75, 76]. A change in controlling mechanism from cross-slip to dislocation climb and sub-boundary migration at high temperatures leads to high $n_{V,Voce}$ value.



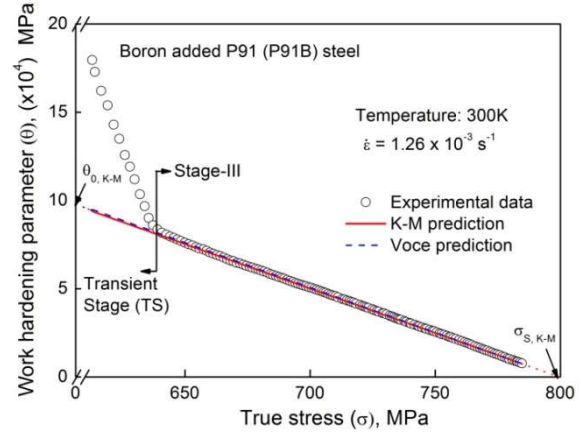
(a) $\theta_0, K-M/\mu$



(b) $\sigma_s, K-M/\mu$



(c) $n_{v, K-M}$



(d) K–M Concept

Fig. 4.11: The variations of (a) normalised saturation stress ($\sigma_{s, K-M}/\mu$), (b) normalised work hardening rate ($\theta_{0, K-M}/\mu$), (c) $n_{v, K-M}$ parameters obtained by K–M concept for boron added P91 steel and (d) K–M Concept has been shown in terms of θ – σ plot

Following the Kocks–Mecking formulation [51] the different work–hardening parameters associated with linear stage–III work hardening were evaluated using Eq. [2.37] as shown in **Fig. 4.11d**. The variation of θ with σ at 300 K showing two stage work hardening behaviour characterized by a rapid decrease in θ at low stresses (transient stage–TS) followed by a gradual decrease at high stresses (stage–III) as shown in **Fig. 4.11d**. The initial work-hardening rate $\theta_{0, K-M}$ is evaluated as the intercept at $\theta = 0$. The subscript “K–M” indicates evaluation of work–hardening parameters using the Kocks–Mecking approach [51]. Saturation stress $\sigma_{s, K-M}$ is obtained as the extrapolated stress value at $\theta = 0$. The values of constant $n_{v, K-M}$ have been evaluated from the slopes of the linear θ vs. σ plots for all temperatures and strain rates examined in this study.

The variations of work hardening parameters, i.e., initial work hardening rate ($\theta_{0, K-M}$), saturation stress ($\sigma_{s, K-M}$) and $n_{v, K-M}$ (the slope of θ versus σ plot in stage–III) obtained by using Kocks–Mecking approach (**Fig. 4.11a–c**) with temperature have been examined for different strain rate conditions in boron added P91 steel. In order to bring out the influence of temperature

alone modulus compensated stress and work hardening values have been considered. The variations in normalized initial work hardening rate ($\theta_{0,K-M}/\mu$) with temperature exhibited a marginal increase from 300 to 473 K followed by pronounced variations at intermediate temperatures in terms of discernable peaks and a rapid increase at high temperatures for all strain rate conditions (**Fig. 4.11a**). Only marginal influence of strain rate on $\theta_{0,K-M}/\mu$ values at room and in distinct influence in intermediate temperatures followed by increase in values with decreasing strain rate has been observed at high temperature. The variations in normalized saturation stress ($\sigma_{S,K-M}/\mu$) with temperature for all strain rate conditions displayed three distinct temperature regimes in terms of a gradual decrease from 300 to 473 K followed by distinct plateaus/peaks at intermediate temperatures and a rapid decrease at high temperatures (**Fig. 4.11b**). A systematic decrease in the saturation stress with increasing at intermediate and increase with decreasing the strain rate at high temperature has been observed. Like $\theta_{0,K-M}/\mu$, the rate parameter $n_{V,K-M}$ (the slope of θ – σ plot in stage–III) also been exhibited a marginal increase in $n_{V,K-M}$ from room to intermediate temperatures followed by a rapid increase at high temperatures for all test conditions (**Fig. 4.11c**). Further, a marginal decrease in $n_{V,K-M}$ with increasing strain rate at room and intermediate temperatures are observed. At high temperatures, significant decrease in $n_{V,K-M}$ with increasing strain rate can be seen in **Fig. 4.11c**.

A state of constancy in stress–strain behaviour represents the saturation stress arising due to equilibrium between dislocation generation and annihilation (arrangement) [51, 52]. Decrease in $\sigma_{S,K-M}/\mu$ with increase in temperature indicates an occurrence of steady state at low stresses (**Fig. 4.11b**). The variations of K–M derived work hardening parameters $\sigma_{S,K-M}/\mu$, $\theta_{0,K-M}/\mu$ and $n_{V,K-M}$ with temperature displayed distinct peaks/plateaus at intermediate temperatures (**Fig. 4.11a-c**). These anomalous variations in work hardening parameters are also reflected in

the grouping of θ – σ and $\theta\sigma$ – σ data in a narrow band at intermediate temperatures (**Fig. 4.17a-b**). This anomalous behaviour can be attributed to the existence of dynamic strain aging (DSA). Based on the measurement of activation energy reported for P91 steel for the onset of serrations, it has been predicted that locking of dislocations by diffusing interstitial solutes such as carbon is responsible for DSA [71, 77]. It is strongly believed that the same DSA mechanism reported for P91 steel could also be considered as a reason for occurrence of DSA in boron added P91 steel. Serrated flow is one of the most important manifestations of DSA. Other manifestations of DSA observed in boron added P91 steel include peaks/plateaus in the flow stress and average work hardening rate and ductility minima at intermediate temperatures. It has been evident in several metals and alloys that DSA causes an increased rate of dislocation multiplication and delay in recovery processes due to delay in cross-slip [57, 59, 60, 62, 63, 66, 67, 69]. Locking of dislocations by diffusing solutes promotes planar slip and uniform distribution of dislocations or ill-defined dislocation substructure rather than well-defined dislocation cells in the DSA regime [38, 60, 62, 66, 67, 78]. Promotion of planar slip due to DSA shifts the required flow stress for cross-slip to higher stresses [49]. Small decrease in $\sigma_{S,K-M}/\mu$ and a marginal increase in $\theta_{0,K-M}/\mu$ and $n_{V,K-M}$ values from 300 K to those at intermediate temperatures indicate that the dislocation sub-structural behaviour in its totality in the two temperature regimes are not very different. This also suggests that long range stress fields due to dislocation multiplication and its interaction play a major role at room and intermediate temperatures [73, 74]. At high temperatures, a rapid decrease in $\sigma_{S,K-M}/\mu$ and a rapid increase in $\theta_{0,K-M}/\mu$ and $n_{V,K-M}$ with increasing temperature (**Fig. 4.11a-c**) indicate acceleration of recovery processes. The dominance of dynamic recovery is also reflected in a rapid shift in θ – σ and $\theta\sigma$ – σ to low stresses with increasing temperature (**Fig. 4.17a-b**). Apart from decrease in flow stress and increase in

total ductility, the dominance of dynamic recovery at high temperatures has been demonstrated through decrease in dislocation density, formation of well-defined sub-grains rather than dislocation cells and rapid increase in the size of dislocation substructure with increasing temperature [66, 69]. Since both $\theta_{0,K-M}/\mu$ and $n_{V,K-M}$ are interrelated, any increase in $n_{V,K-M}$ will result in increased $\theta_{0,K-M}/\mu$ value. The rapid increase in $\theta_{0,K-M}/\mu$ and $n_{V,K-M}$ values can be ascribed to change in controlling deformation mechanism from cross-slip to climb of dislocations and sub-boundary migration at high temperatures. It has been reported that $n_{V,K-M}$ is expected to have a low absolute value at low and intermediate temperatures, where cross-slip is dominant [51, 75, 76]. A change in controlling mechanism from cross-slip to dislocation climb and sub-boundary migration at high temperatures leads to high $n_{V,K-M}$ value.

4.5 Activation energy measurement for dynamic recovery

The activation energy for dynamic recovery is calculated using the model proposed by Bergström and Hallén [77, 78]. According to the model the dynamic recovery is governed by cross-slip of screw dislocations at low and intermediate temperature, and dislocation climb dominates over cross-slip mechanism at high temperatures. The dominance of cross-slip at low and intermediate temperatures and dislocation climb at high temperatures is shown schematically in Fig. 4.12a-d. The model describe the dynamic recovery parameter (k_2) in terms of two components as cross-slip and climb controlled recovery regimes as a function of temperature and it is expressed in generalized form as

$$k_2 = k_{2,Cross-slip} + k_{2,Climb} \quad (4.2)$$

when $k_2 = n_v$, the Equation [4.2] can be rewrite as

$$n_v = n_{v,Cross-slip} + n_{v,Climb} \quad (4.3)$$

The first term $n_{v,Cross-slip}$ is given as

$$n_{v,Cross-slip} = C \exp\left(\frac{-Q_c}{RT}\right), \quad (4.4)$$

where C is a constant, R is the universal gas constant and Q_c is the activation energy for cross-slip. The second term $n_{v,Climb}$ in Equation [4.3] is given as

$$n_{v,Climb} = A \exp\left(\frac{-Q_m}{3RT}\right), \quad (4.5)$$

where A is a constant and Q_m is the activation energy for vacancy diffusion. Assuming that cross-slip dominates at room and intermediate temperatures (300–723 K), the n_v parameter was fitted with Equation [4.3] and the values of C and Q_c was obtained. The values of $n_{v,Climb}$ at high temperature above 723 K were evaluated as $n_{v,Climb} = n_v - n_{v,Cross-slip}$ by appropriately using the extrapolated $n_{v,Cross-slip}$ values for different temperatures. Subsequently, the values of A and Q_m are calculated from the best fit $n_{v,Climb}$ vs. T using Equation (4.5). The values for C , Q_c , A and Q_m for all strain rate conditions are listed in **Table-4.2**.

Table-4.2: The calculated values of constants and activation energy for dynamic recovery model proposed by Bergström and Hallén [77, 78]

Strain rate ($\dot{\epsilon}$)	C	Q_c kJ mol ⁻¹	A	Q_m kJ mol ⁻¹
$1.26 \times 10^{-3} \text{ s}^{-1}$	228.15	3.87	5.51×10^5	167.6
$3.16 \times 10^{-4} \text{ s}^{-1}$	212.72	3.86	1.87×10^6	187.8
$3.16 \times 10^{-5} \text{ s}^{-1}$	164.02	3.09	2.76×10^6	191.8

Table-4.3. Transition temperature for onset of climb controlled mechanism for different strain rates of boron added P91 steel.

Strain rate ($\dot{\epsilon}$)	Transition temperature for onset of climb controlled mechanism
$1.26 \times 10^{-3} \text{ s}^{-1}$	804 K
$3.16 \times 10^{-4} \text{ s}^{-1}$	779 K
$3.16 \times 10^{-5} \text{ s}^{-1}$	752 K

The average values of activation energy for cross-slip mechanism as $Q_c = 3.61 \text{ kJ mol}^{-1}$ ($37.5 \times 10^{-3} \text{ eV/atom}$) and for climb mechanism as $Q_m = 182.4 \text{ kJ mol}^{-1}$ have been obtained. The

typical variations of recovery parameter components, i.e. $n_{v,Cross-slip}$ and $n_{v,Climb}$ with temperature for three different strain rates of $1.26 \times 10^{-3} \text{ s}^{-1}$, $3.16 \times 10^{-4} \text{ s}^{-1}$ and $3.16 \times 10^{-5} \text{ s}^{-1}$ are shown in **Fig. 4.12a-c**. A transition in the controlling deformation mechanism from cross-slip at room and intermediate temperatures to climb mechanism at high temperatures can be clearly seen in **Fig. 4.12a-c (arrow marks)**. It can also be observed that the temperature at which transition take place from cross-slip dominated deformation to climb controlled deformation decreases with decreasing the strain rate (**See in Table-4.3**). The predicted dynamic recovery parameter values using Bergström and Hallén [77, 78] approach for different temperatures and strain rates are superimposed as solid lines in **Fig. 4.12d**.

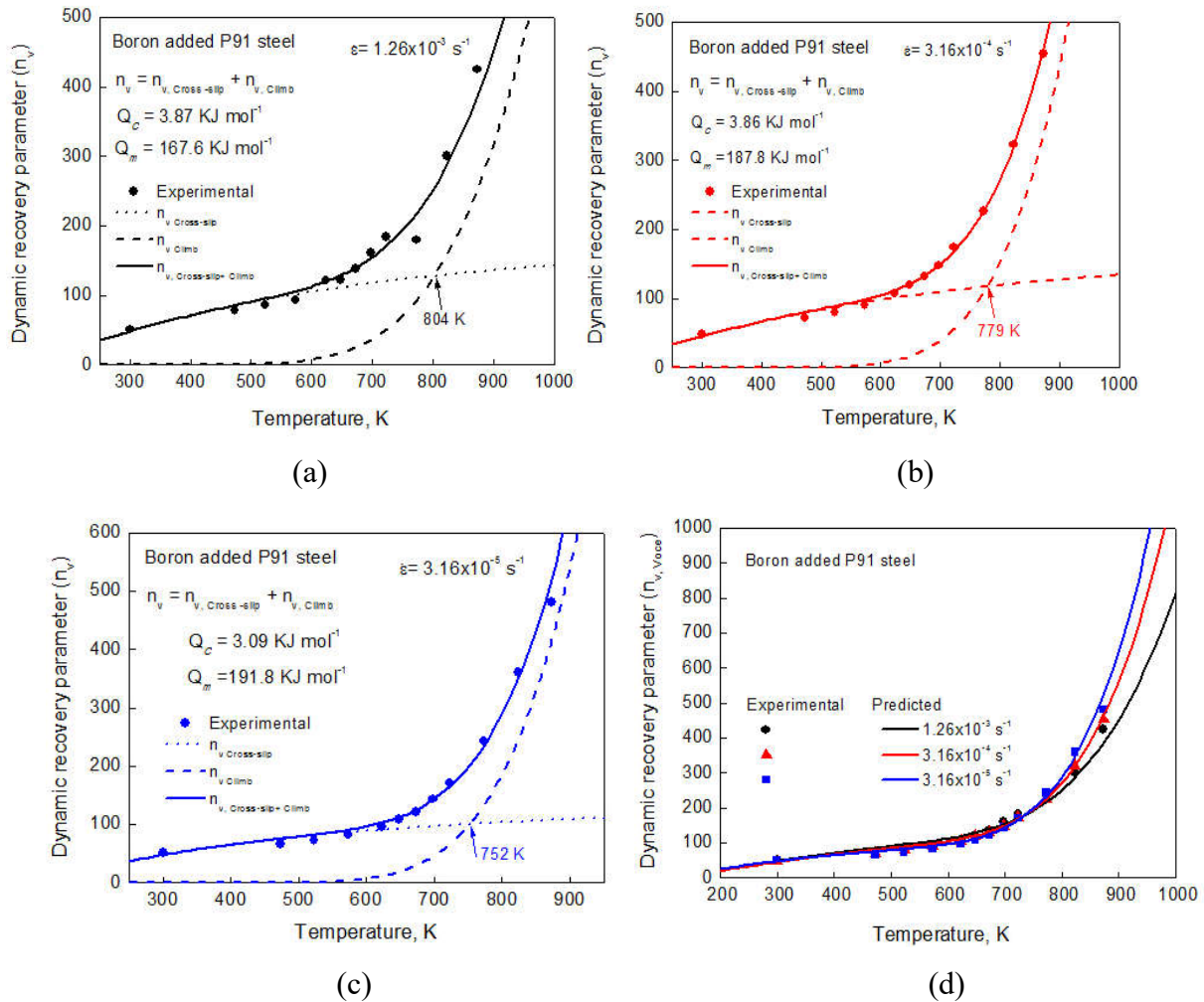


Fig. 4.12: The variation of dynamic recovery parameter (n_v) with temperature for boron added P91 steel at different strain rates (a) $1.26 \times 10^{-3} \text{ s}^{-1}$ (b) $3.16 \times 10^{-4} \text{ s}^{-1}$ (c) $3.16 \times 10^{-5} \text{ s}^{-1}$ (d) Applicability of Bergström and Hallén model for all strain rates (**Symbols:** Experimental data, **Solid lines:** Predicted values).

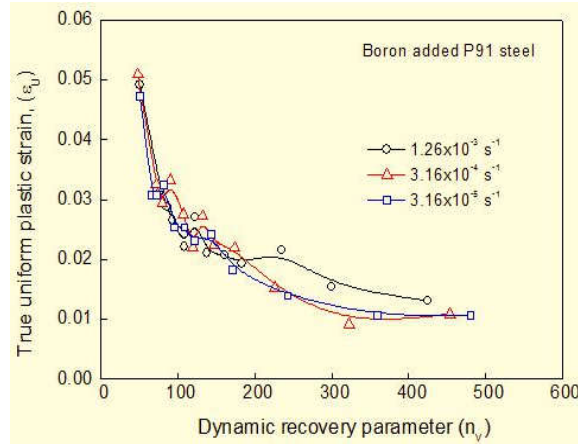
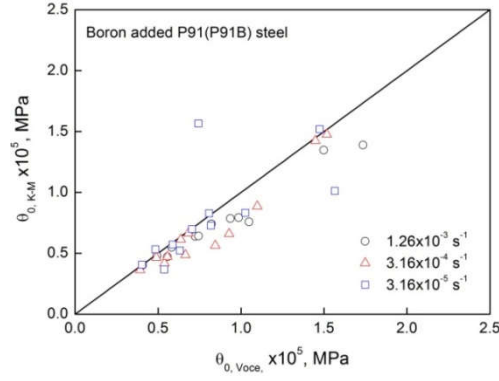


Fig. 4.13: The variation of true uniform plastic strain with dynamic recovery parameter for all strain rates of boron added P91 steel.

The variation of true uniform plastic strain with dynamic recovery parameter exhibited that true uniform plastic strain (ϵ_u) strongly depends on dynamic recovery parameter in 9% Cr steels. With increase in dynamic recovery parameter, decrease in true uniform plastic strain for all the strain rates has been noticed (**Fig. 4.13**).

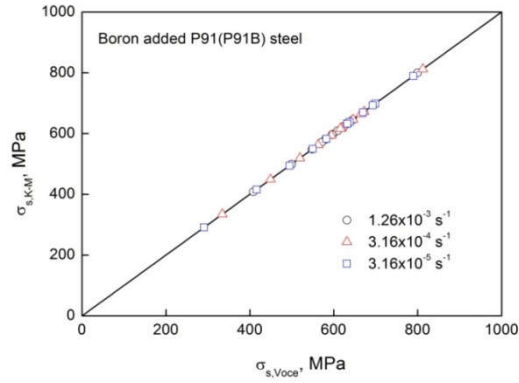
4.7 Comparison of work hardening parameters obtained using K–M approach and Voce equation

The work hardening parameters such as initial work hardening rate ($\theta_{0,K-M}$), saturation stress ($\sigma_{S,K-M}$) and the slope of θ – σ plots in stage–III ($n_{V,K-M}$) obtained using K–M approach have been compared with the respective parameters evaluated using Voce equation and its derivative form in **Fig. 4.14** to **Fig. 4.16**.



$\theta_{0, K-M}$ VS. $\theta_{0, \text{Voce}}$

Fig. 4.14: Comparison of initial work hardening rates evaluated using K–M approach ($\theta_{0, K-M}$) and derivative form of Voce equation ($\theta_{0, \text{Voce}}$) at different temperatures and heat treatment conditions in boron added P91 steel. Theoretical $\theta_{0, K-M} = \theta_{0, \text{Voce}}$ line is shown as solid line.



$\sigma_{s, K-M}$ VS. $\sigma_{s, \text{Voce}}$

Fig. 4.15: Comparison of saturation stresses evaluated using K–M approach ($\sigma_{s, K-M}$) and Voce equation ($\sigma_{s, \text{Voce}}$) at different temperatures and heat treatment conditions in boron added P91 steel. Theoretical $\sigma_{s, K-M} = \sigma_{s, \text{Voce}}$ line is shown as a solid line.

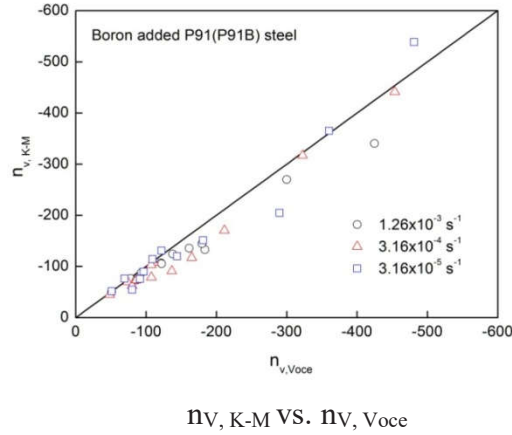


Fig. 4.16: Comparison of rate parameter n_V evaluated using K–M approach ($n_{V,K-M}$) and Voce equation ($n_{V,Voce}$) at different temperatures and heat treatment conditions in boron added P91 steel. Theoretical $n_{V,K-M} = n_{V,Voce}$ line is shown as a solid line.

Figure 4.14 shows a comparison between $\theta_{0,K-M}$ and $\theta_{0,Voce}$ along with $\theta_{0,K-M} = \theta_{0,Voce}$ equivalence line for different temperature and strain rate conditions in boron added P91 steel. The values of $\theta_{0,Voce}$ at various test conditions have been evaluated as $\theta_{0,Voce} = -n_{V,Voce} \times \sigma_{S,Voce}$ following **Eq. 2.38**. At all the temperatures and strain rate conditions, a reasonable correlation between $\theta_{0,K-M}$ and $\theta_{0,Voce}$ is obtained. The saturation stress ($\sigma_{S,K-M}$) values evaluated using K–M approach have been compared with the saturation stress ($\sigma_{S,Voce}$) values obtained by Voce equation (**Fig. 4.15**). Theoretical $\sigma_{S,K-M} = \sigma_{S,Voce}$ is superimposed as a solid line in **Fig. 4.15**. At all the temperature and strain rates, an excellent match between $\sigma_{S,K-M}$ and $\sigma_{S,Voce}$ is observed in boron added P91 steel. The equivalence between $\sigma_{S,K-M}$ and $\sigma_{S,Voce}$ obtained for boron added P91 steel is in perfect order. $\sigma_{S,K-M}$ is determined as the extrapolated flow stress at $\theta = 0$, whereas $\sigma_{S,Voce}$ is obtained as the asymptotic stress value from the best fit σ – ϵ data. Therefore, $\sigma_{S,Voce}$ is expected to be lower than $\sigma_{S,K-M}$. However, $\theta = \sigma$ line lying close to stress axis as shown in **Fig. 4.15** indicates only marginal difference between $\sigma_{S,K-M}$ and $\sigma_{S,Voce}$. Even small difference between $\sigma_{S,K-M}$ and $\sigma_{S,Voce}$ is not expected to be visible in the $\sigma_{S,K-M}$ versus $\sigma_{S,Voce}$ plot and will be absorbed within the scatter of experimental data. The variations of $n_{V,K-M}$ with $n_{V,Voce}$ along

with $n_{V,K-M} = n_{V,Voce}$ solid line are shown in **Fig. 4.16** for all strain rate conditions in the temperature range 300–873 K. A reasonable correlation between $n_{V,K-M}$ and $n_{V,Voce}$ is observed at all the temperatures and strain rate conditions for this steel. Marginally higher values obtained for $\theta_{0,Voce}$ and $n_{V,Voce}$ than the respective values of work hardening parameters evaluated using K–M approach results from the averaging nature of the best fit obtained for the Voce equation describing full range of σ – ϵ data. All these observations suggest a good correlation between the respective work hardening parameters obtained using K–M approach and Voce equation, and demonstrate a reasonable analogy between the two approaches for describing tensile work hardening behaviour in boron added P91 steel.

4.8 Influence of temperature and strain rate on the variations of instantaneous work hardening rate (θ) with stress (σ)

The tensile work hardening behaviour of many metals and alloys can be described satisfactorily using macroscopic term, the instantaneous work hardening rate (θ) and its variation with true stress (σ). The network hardening of material results from mutual competition between hardening and dynamic recovery associated with generation, multiplication and annihilation (re-arrangement) of dislocations [51,79]. The main intention of demonstration this θ – σ and $\theta\sigma$ – σ plots are to identify the different stages of work hardening present in the material. It is very difficult to notice different work hardening stages operating in the materials with help of single θ – σ plots. It is easy to classify stages of work hardening with help of $\theta\sigma$ – σ plots. Accordingly, the variations of θ and $\theta\sigma$ obtained from σ – ϵ data as a function of true stress (σ) have been considered to understand the work hardening behaviour in boron added P91 steel. Typical plots of θ vs. σ and $\theta\sigma$ vs. σ for all temperatures at the strain rate of $1.26 \times 10^{-3} \text{ s}^{-1}$ are given in **Fig. 4.17a-b** respectively. The influence of temperature on θ vs. σ and $\theta\sigma$

vs. σ at the strain rate of $1.26 \times 10^{-3} \text{ s}^{-1}$ for boron added P91 steel can be seen in **Fig. 4.17a-b**.

In general, θ vs. σ plots shift towards lower stress with increase in temperature. At intermediate temperatures (473-698 K), insignificant influence of temperature on θ - σ shift is observed and all θ - σ data become bunch together in a narrow band (**Fig. 4.17a-b**). Beyond 723 K, a rapid shift in θ vs. σ towards lower stresses is noticed with increasing in temperature. This is in consistent with the σ - ϵ behaviour at high temperatures displaying rapid decrease in flow stress with increasing temperature (**Fig. 4.1a-c**). The above stated observations indicate three distinct temperature regimes of work hardening behaviour; low, intermediate and high temperatures. The temperature range for each regime remains similar for both σ - ϵ response (**Fig. 4.1a-c**) θ - σ and $\theta\sigma$ - σ (**Fig. 4.17a-b**).

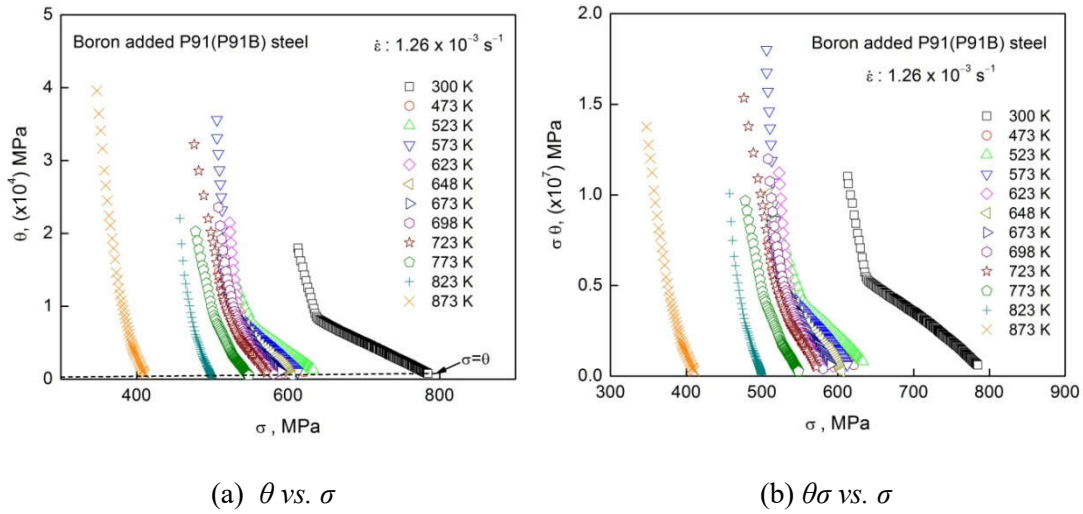


Fig. 4.17: The variation of (a) θ vs. σ and (b) $\theta\sigma$ vs. σ for all test temperatures at the strain rate of $1.26 \times 10^{-3} \text{ s}^{-1}$ for boron added P91 steel.

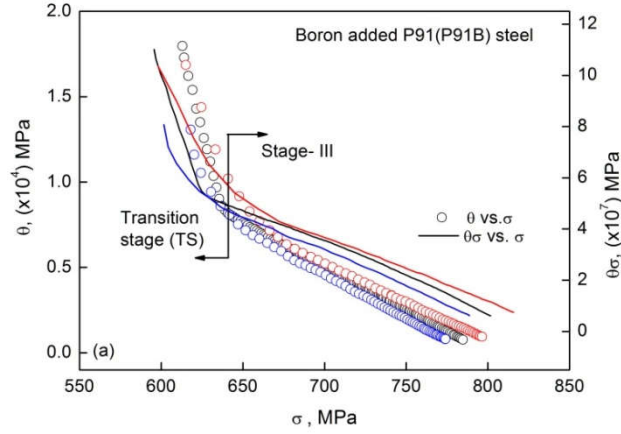


Fig. 4.18: The variation of θ vs. σ and $\theta\sigma$ vs. σ at 300 K at all strain rates for boron added P91 steel.

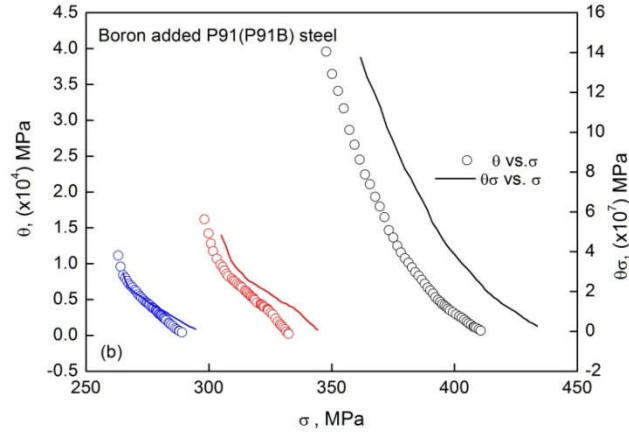


Fig. 4.19: The variation of θ vs. σ at 873 K at all strain rates for boron added P91 steel.

Subsequently, at all temperatures and strain rate conditions, θ vs. σ and $\theta\sigma$ vs. σ plots exhibited an initial rapid decrease in θ and $\theta\sigma$ at low stresses followed by a gradual decrease in θ and $\theta\sigma$ with σ at high stresses. The initial rapid decrease in θ and $\theta\sigma$ is designated as transient stage or TS, whereas the gradual decrease region typically represents stage–III work hardening. For room temperature, the distinction between these two stages is clearly witnessed as shown in **Fig. 4.18**. In contrast, at high temperature (873 K), there is an absence of a sharp division between the two stages is noticed as shown in **Fig. 4.19**. The observed transient stage is different from stage–I in single crystal (**Fig. 2.23**), wherein the value of θ lies much lower than that in stage–III unlike several metals and alloys including 316LN stainless steels [56, 70, 82]. It is clearly

noticed that both θ vs. σ and $\theta\sigma$ vs. σ plots failed to resolve athermal stage–II work hardening in boron added P91 steel. Based on the work hardening behaviour of single and polycrystals it has been suggested that there is no solid reason for the absence of three stages of work hardening but experimentally all the three stages together has not been reported in work hardening plots of polycrystalline BCC metals and alloys [83]. The observed two–stage work hardening is in agreement with those reported for 9% Cr steels, recently [82, 84, 85, 86, 87, 88].

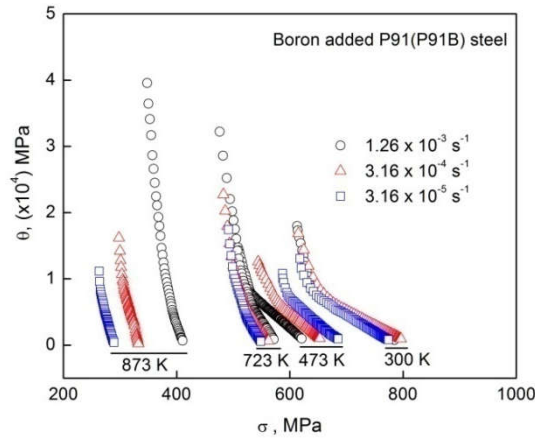


Fig. 4.20: The variation of instantaneous work hardening rate parameter (θ) with true stress (σ) at selected temperatures of 300, 473, 723, and 873 K at all the strain rates for boron added P91 steel.

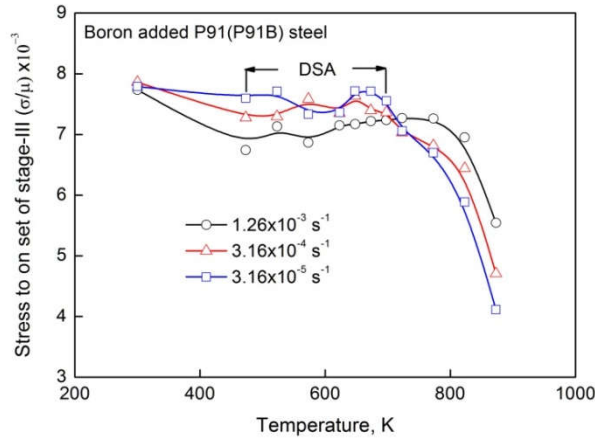


Fig. 4.21: The variation of normalized stress to onset of stage–III with temperature at all the strain rates for boron added P91 steel.

The influence of strain rate on θ – σ work hardening behaviour has been examined for the variations of instantaneous work hardening rate (θ) with true stress (σ) in **Fig. 4.20**. The strain rate is found to show insignificant influence on θ – σ behaviour at 300 K, increases θ – σ values with decrease in strain rate at 473 K, followed by marginally higher θ – σ values with decrease in strain rate at 723 K. At high temperature (873 K), θ – σ data appears to be more scatter and rapid shift in θ – σ towards low stresses has been observed with decrease in strain rate. The influence of strain rate and temperature on the stress to onset of stage–III (σ_{III}) is presented in **Fig. 4.21**. The stress (σ_{III}) values have been determined as the stress for the transition from transient stage to stage–III as shown in **Fig. 4.18**. At high temperatures, σ_{III} is obtained as the stress for the intersection of the straight lines representing low and high stress regimes. At all strain rates, the variations of σ_{III} also exhibited three temperature regimes, i.e., a gradual decrease up to 473 K followed by plateaus at intermediate temperatures and a rapid decrease at high temperatures (**Fig. 4.21**). It may be noted that the material showed a marginal increase in σ_{III} with decrease in strain rate at intermediate temperatures followed by decreases systematically with decreasing strain rate at high temperatures. The occurrence of peaks/plateaus in $\sigma_{III/\mu}$ at intermediate temperature suggests that the onset of stage–III is athermal in the DSA temperature domain. In the recovery–dominant high temperature regime, a systematic decrease in $\sigma_{III/\mu}$ with decrease in strain rate has been observed.

4.9 Fracture surface examination of boron added P91 steel

Fracture surface examination of tensile tested boron added P91 samples were carried with Scanning Electron Microscope for all the samples tested at different temperatures and strain rate conditions. However, the samples at 300, 573, 623 and 873 K temperature tested samples images are only presented for this investigation as shown in **Fig. 4.22-4.25**. Scanning Electron

Microscopic examinations of fracture surfaces of tensile tested specimens revealed typical fracture mode that remains transgranular in boron added P91 steel. The fracture surfaces at low magnifications displayed flat fracture with some shear regions at room temperature (**Fig. 4.22a**) and typical cup and cone fracture along with distinct shear lip zone at intermediate and high temperatures (**Fig. 4.23a, 4.24a & 4.25a**). SEM examination exposed large amount of chisel tip appearance with distinct dimples at 300 K as shown in **Fig. 4.22a-b**. At intermediate and high temperatures, the fracture was dominated mainly by the presence of ductile dimples. Insignificant variations in the size of dimples with respect to temperature were observed at intermediate temperatures in the range 473–723 K (**Fig. 4.23b, 4.24b**). At high temperatures, an increase in dimple size with increase in temperature in the range 773–873 K can be seen in **Fig. 4.25b**. The detailed fracture surface examination clearly indicated that the fracture mode remain transgranular for the range of temperatures and strain rates examined (**Fig. 4.23-4.25**). At room temperature, the observed chisel tip appearance occurs due to de-cohesion and split in the martensite lath boundaries are in agreement with the reported observations in 9% chromium steels [70, 79, 86, 87, 88]. At intermediate and high temperatures, the fracture mode was dominated by the presence of ductile dimples resulting from micro-void coalescence. The observed insignificant variation in the reduction in area is well supported by the insignificant variations in necking (**Fig. 4.4b**) as well as the dimple size (**Fig. 4.23b and 4.24b**) with respect to temperature in the region 473–723 K. Significant increase in tensile ductility in regime-773–873 K (**Fig. 4.25b**) is reflected in the extensive necking (**Fig. 4.25a**) and increase in dimple size (**Fig. 4.25b**) with increase in temperature. This suggests that the growth process of voids dominates over nucleation at high temperatures. Therefore, the observed transgranular fracture

rules out intergranular cracking causing reduction in strength values at high temperatures in Boron added P91 steel.

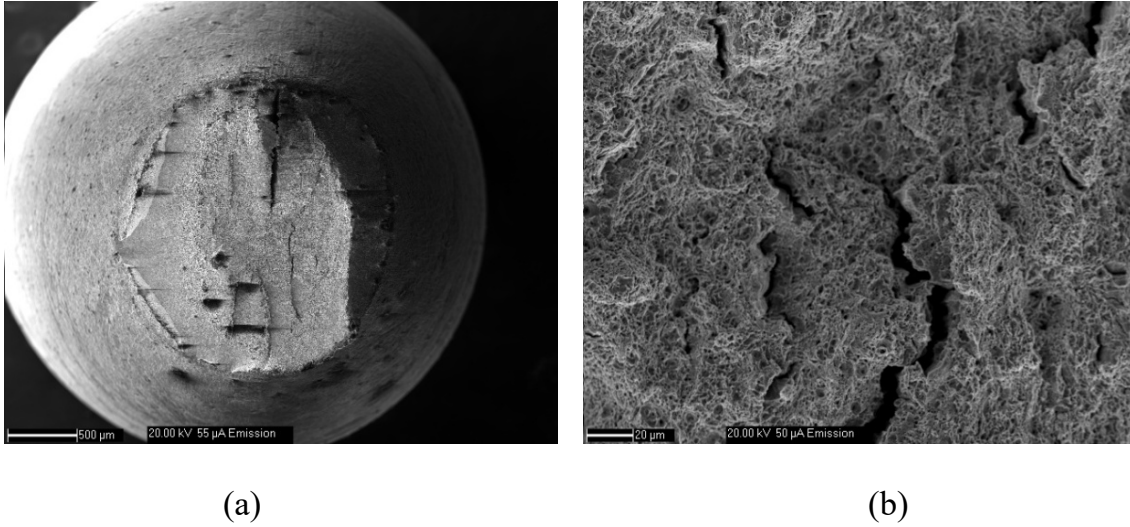


Fig. 4.22: Fracture surface images of tensile tested boron added P91 steel at 300 K.

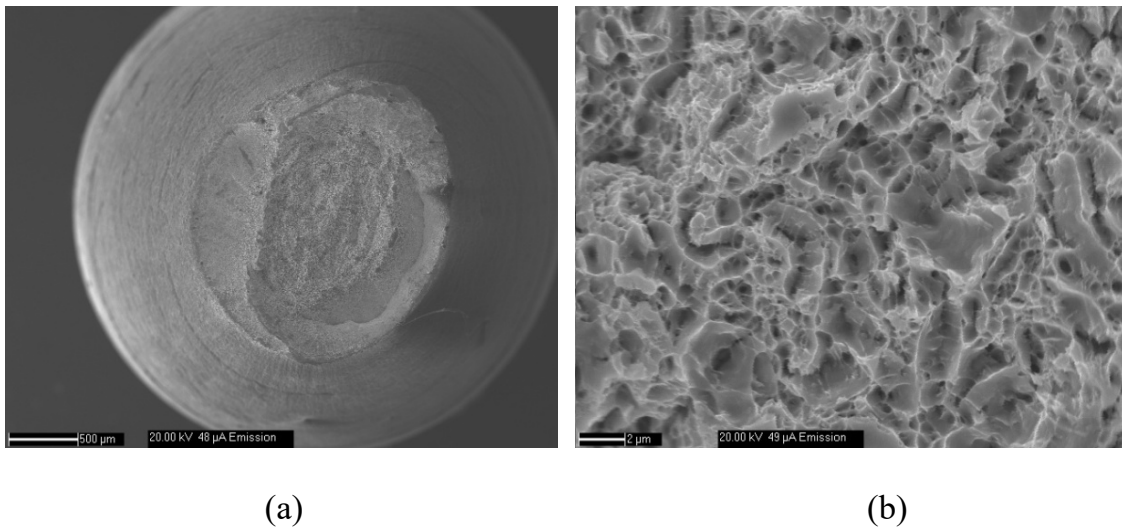
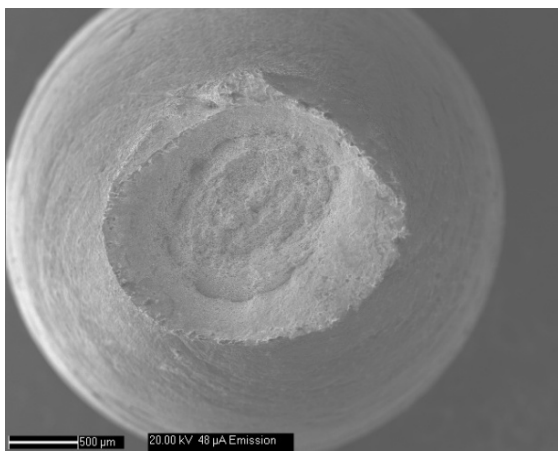
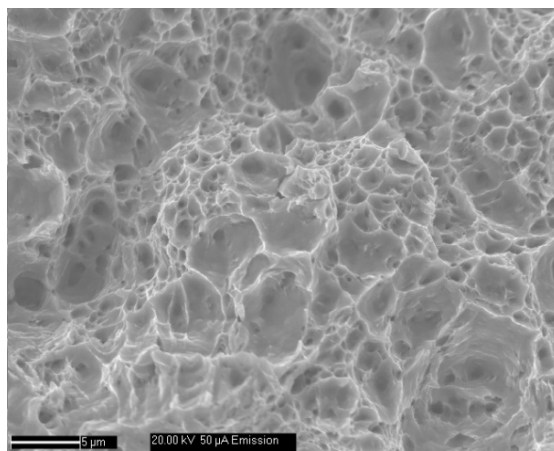


Fig. 4.23: Fracture surface images of tensile tested boron added P91 steel at 573 K.

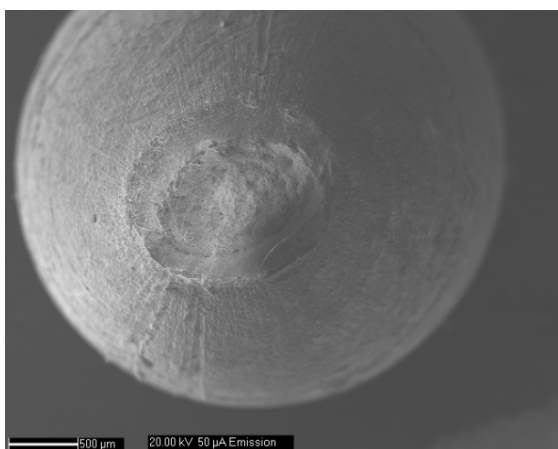


(a)

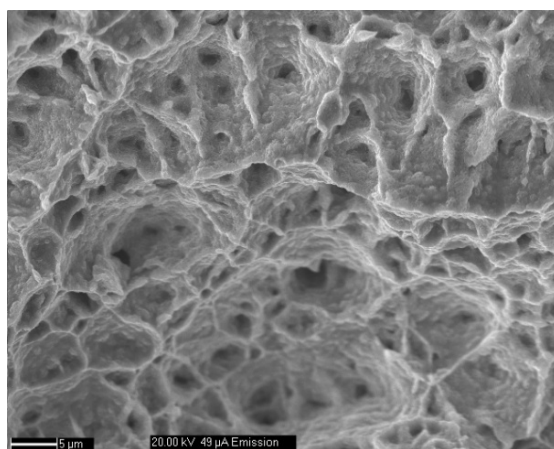


(b)

Fig. 4.24: Fracture surface images of tensile tested boron added P91 steel at 623 K.



(a)



(b)

Fig. 4.25: Fracture surface images of tensile tested boron added P91 steel at 873 K.

Chapter 5: COMPARATIVE EVALUATION OF MICROSTRUCTURE AND TENSILE FLOW BEHAVIOUR OF BORON ADDED P91 AND P91 STEELS

5.1 Introduction

The chemical composition of the boron added P91 steel given in **Table-1** showed that nitrogen content is significantly lower compared to P91 (ASME P91) steel which is having N in the range of 0.03–0.07 wt. %. For the initial alloy design, the chemical composition of the experimental heat was chosen for boron added P91 steel in such a way that there should not be a formation of boron nitride (BN) during processing and heat treatment conditions as depicted in **Fig. 5.1** [89, 90, 91]. It is well known that the stability of $M_{23}C_6$ precipitates enhanced due to the presence of boron in carbide sub-lattice as $M_{23}(B,C)_6$ which is possible by avoiding the formation of boron nitride precipitates in the steel.

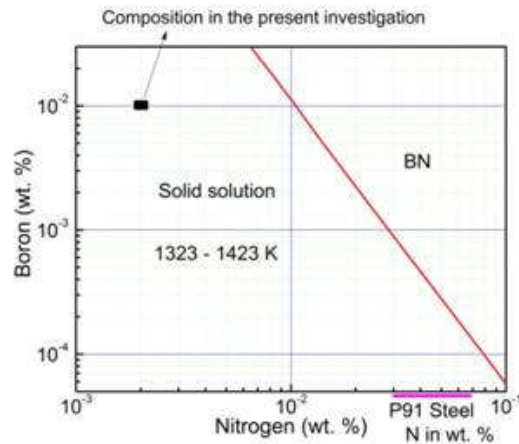


Fig. 5.1: Composition diagram for boron and nitrogen showing formation of solid solution or boron nitride (BN) at a normalizing temperature of 1323–1423 K.

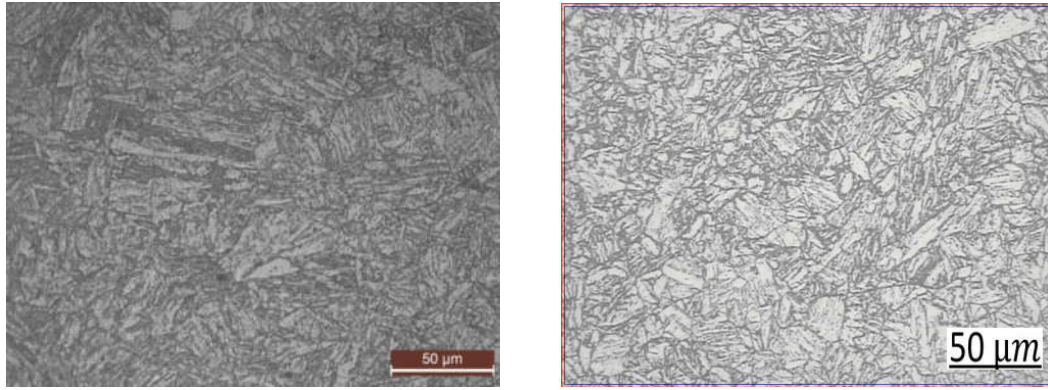
In view of above, nitrogen level in this steel was deliberately lowered to avoid formation of boron nitride as boron has a strong affinity for nitrogen. Boron added P91 steel supplied in the

form of 12 mm plates and normalizing was done at 1338 K for 2 h followed by air cooling and tempering at 1053 K for 2 h followed by air cooling was used in the present investigation. However, the comparative evaluation of microstructure and tensile flow behaviour between boron added P91 and P91 steel is recommended for the further optimization of chemical composition of the steel in future applications. The in-house tensile data obtained on the normalised and tempered (N+T) P91 steel was used for the comparison purpose [2]. For P91 steel, normalizing was carried at 1333 K for 25 min followed by air cooling and tempering at 1023 K for 2 h followed by air cooling.

5.2 Microstructure of boron added P91 and P91 steel

The microstructure of both steels in normalized and tempered condition revealed tempered martensite with $M_{23}C_6$ precipitates decorated along the prior austenitic grain boundaries and MX precipitates in intra-lath matrix regions [2, 54] as shown by Fig. 5.2a-b. It is well known that the morphology of tempered martensitic microstructure is greatly influenced by prior austenitic grain size which in turn is affected by the heating rate, austenitizing temperature and soaking duration at austenitizing temperature [92, 93]. Increase in prior austenite grain size with increase in the austenitizing temperature and/or soaking duration results in the increased size of packets and blocks in the martensitic microstructure [92, 93]. It has been shown that the slow cooling from austenitizing temperature leads to the development of coarse packets and blocks size in lath martensitic structure [94]. In the present investigation, the extended austenitizing given on the boron added P91 steel resulted in an increase in the prior austenite grain size compared to N+T P91 steel (Fig. 5.2 a-b). In addition to the extended austenitizing treatment, boron added P91 steel was subjected to prolonged tempering treatment

which resulted in the observed coarser martensitic packets and blocks than those in N+T P91 steel.



(a) P91 steel

(b) Boron added P91 steel

Fig. 5.2: Microstructure of (a) P91 steel and (b) Boron added P91 steel in normalized and tempered condition.

Further, the weight and volume fraction of $M_{23}C_6$ and MX precipitates in P91 steel and boron added P91 steel have been calculated using thermo–Calc software with TCFE6 Steels/ Fe-alloy data base [95]. The results are summarized in the below **Table- 5.1**. It has been observed that the calculated weight and volume fraction of $M_{23}C_6$ precipitates in boron added P91 steel is well comparable with P91 steel. However, the weight and volume fraction of MX precipitates in boron added P91 steel is 3 times lower than that in P91 steel. The **table–5.1** results clearly indicated that boron added P91 steel exhibited softened microstructure with reduced weight and volume fraction of MX precipitates over P91 steel.

Table-5.1: The weight and volume fraction of $M_{23}C_6$ and MX precipitates in P91 steel and boron added P91 steel have been calculated using thermo-Calc software with TCFE6 Steels/ Fe-alloy data base [95].

Steel	$M_{23}C_6$		MX	
	Weight fraction	Volume fraction	Weight fraction	Volume fraction
P91B steel	0.017	0.016	0.0011	0.0011
P91 steel	0.018	0.018	0.0035	0.0031

5.2 Mechanical properties

The variations in the tensile properties with temperature have been shown in **Fig. 5.3a-b** and **Fig. 5.4a-c** for both the steels. It is evident from the **Fig. 5.3** that the tensile strength (YS and UTS) values of both the steels as a function of temperature exhibited a decrease from room to intermediate temperature followed by rapid decrease at high temperature. P91 steel has shown reasonably higher strength values than boron added P91 in terms of yield strength (**Fig. 5.3a**) and ultimate tensile strength (**Fig. 5.3b**) for all the temperatures for the strain rate $1.26 \times 10^{-3} \text{ s}^{-1}$.

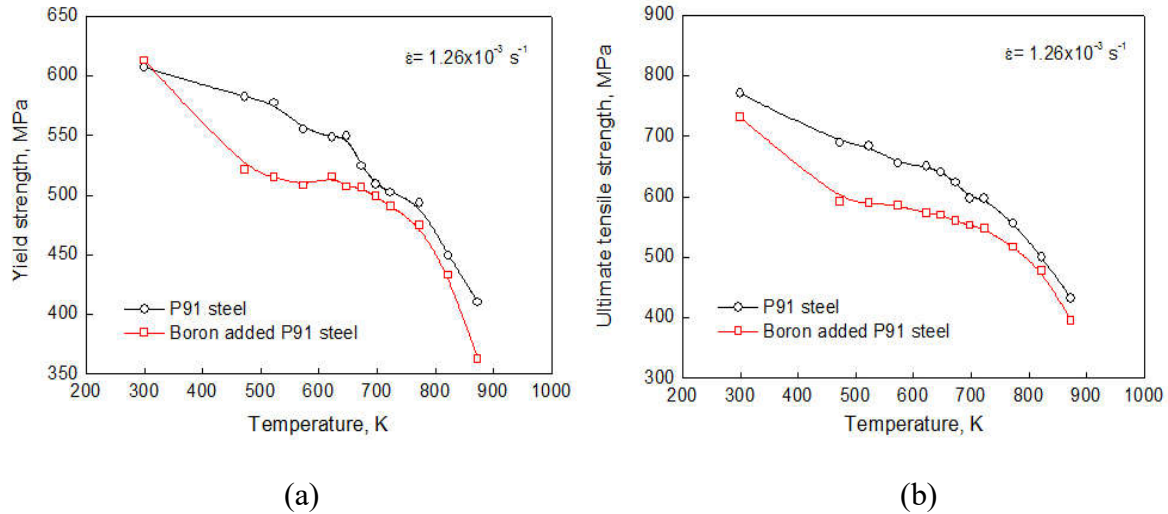
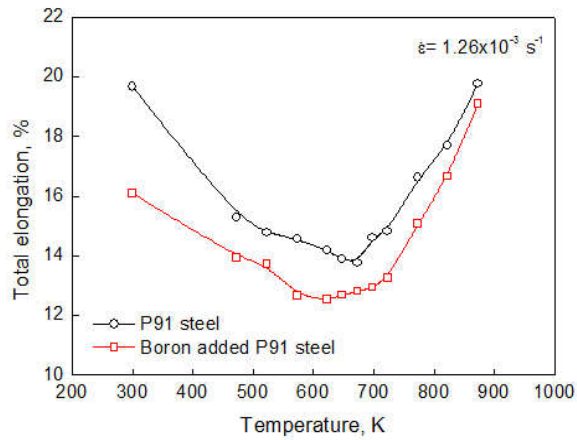


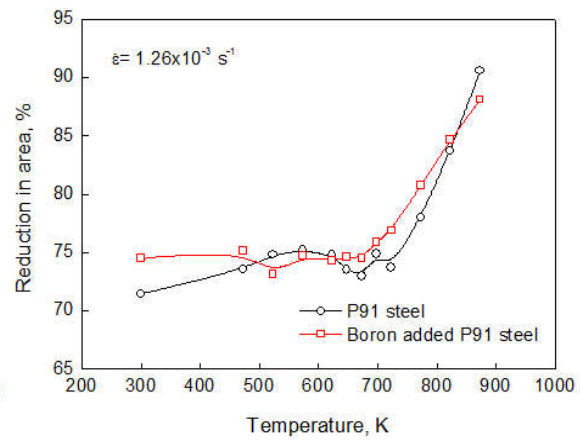
Fig. 5.3: The variations of (a) yield strength and (b) ultimate tensile strength with temperature for boron added P91 steel and P91 steel.

The variations of ductility parameters in terms of percentage of total elongation and reduction in area, and post necking strain with temperature for boron added P91 and P91 steel have been shown in **Fig. 5.4a-c**. The variation of percentage of total elongation with temperature for both the steels exhibited decrease in values from room, ductility minima at intermediate temperature regime followed by rapid increase at high temperatures. P91 steel has shown better ductility than boron added P91 steel for all temperatures (**Fig. 5.4a**). However, the percentage of reduction in area and

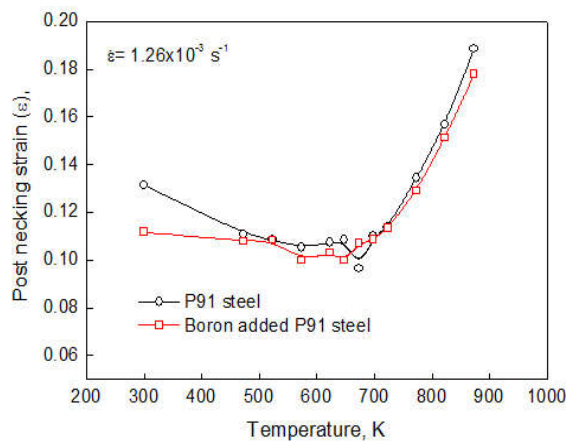
post-necking strain with temperature exhibited a closely comparable values at all temperatures for both the steels. Though the total elongation of P91 steel exhibited higher values than boron added P91 steel, post-necking elongation of the steel is comparable to P91 steel (**Fig. 5.4a-c**) which is also reflected in the large numbers of fine dimples in boron added P91 steel as shown in **Fig. 5.4e-d**.



(a)



(b)



(c)

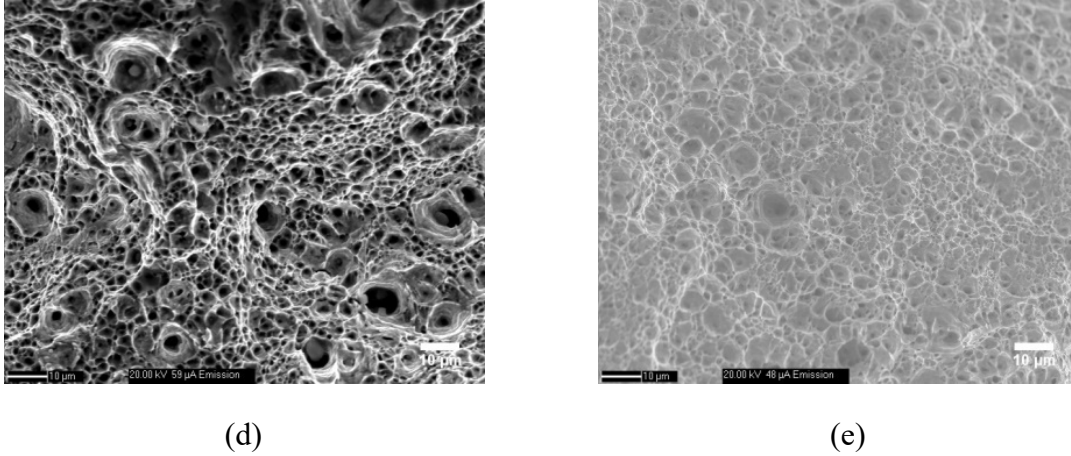


Fig. 5.4: The variations of (a) percentage elongation and (b) percentage reduction in area (c) post necking strain with temperature for both the steels. Fractography images of (d) P91 steel and (e) boron added P91 steel at 773 K.

5.3 Ludwigson derived work hardening parameters

Tensile work hardening behaviour P91 and boron added P91 steel was examined in terms of variations of work hardening parameters obtained by using Ludwigson and Voce flow relationships with temperature. The work hardening parameters associated with Ludwigson relationship such as K_1 , n_1 , K_2 and n_2 pertaining to both the steels as function of temperature has been presented in **Fig. 5.5a-d**. The variations of both strain hardening co-efficient (K_1), exponent (n_1) and $\exp(K_2)$ as function of temperature as shown in **Fig. 5.5a-c** exhibited a continual decrease with increase in temperature for both the steels. For boron added P91 steel, the variation of n_2 with temperature as shown in **Fig. 5.5d** displayed gradual increase (in terms of negative value) from 300 to 673 K followed by rapid increase from 673 to 823 K. However, for P91 steel, the predicted n_2 was obtained up to 723 K. It is suggested that the Ludwigson relationship is applicable for the entire temperature for the case of boron added P91 steel, whereas, for P91 steel, Ludwigson relationship reduced to Hollomon equation at high temperatures.

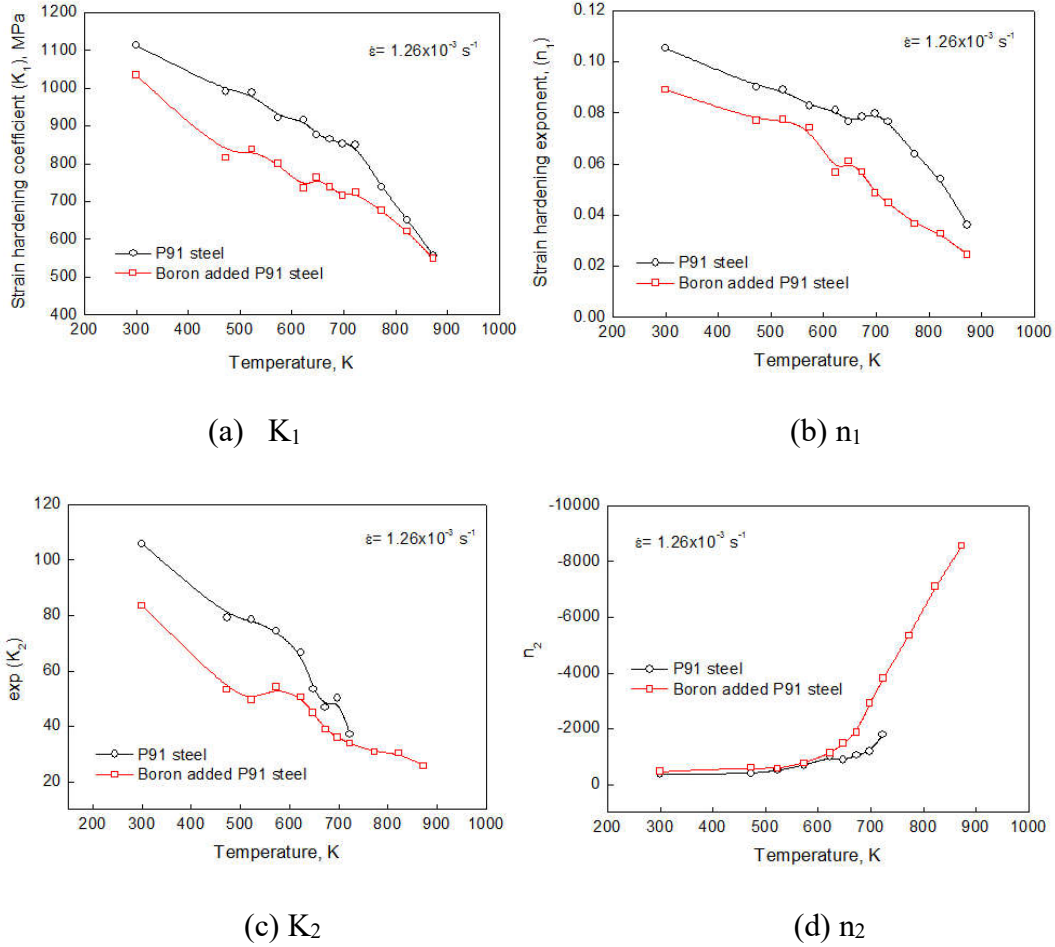


Fig. 5.5: The variations of Ludwigson parameters (a) K_1 (b) n_1 (c) $\exp(K_2)$ and (d) n_2 with temperature for both boron added P91 steel and P91 steel

5.4 Voce derived work hardening parameters

The variation of work hardening parameters pertaining to Voce equation with temperature of both P91 and boron added P91 steel as shown in **Fig. 5.6a-b**. The variation of initial stress and saturation stress with temperature showed a decrease in value with increase in temperature. The rate parameter n_v with temperature displayed continues increase from 300 to 673 K with insignificant peaks at intermediate temperature regime followed by rapid increase at high temperature (673–823 K) (**Fig. 5.6c**). Like Ludwigson parameters (K_1 , n_1 and $\exp(K_2)$), the work hardening parameters associated with the Voce relationship of P91 steel has shown reasonably

higher initial and saturation stress values for entire temperatures than that of boron added P91 steel. Contrary to this, rate parameter (n_v) exhibited lower values for P91 steel compared boron added P91 steel.

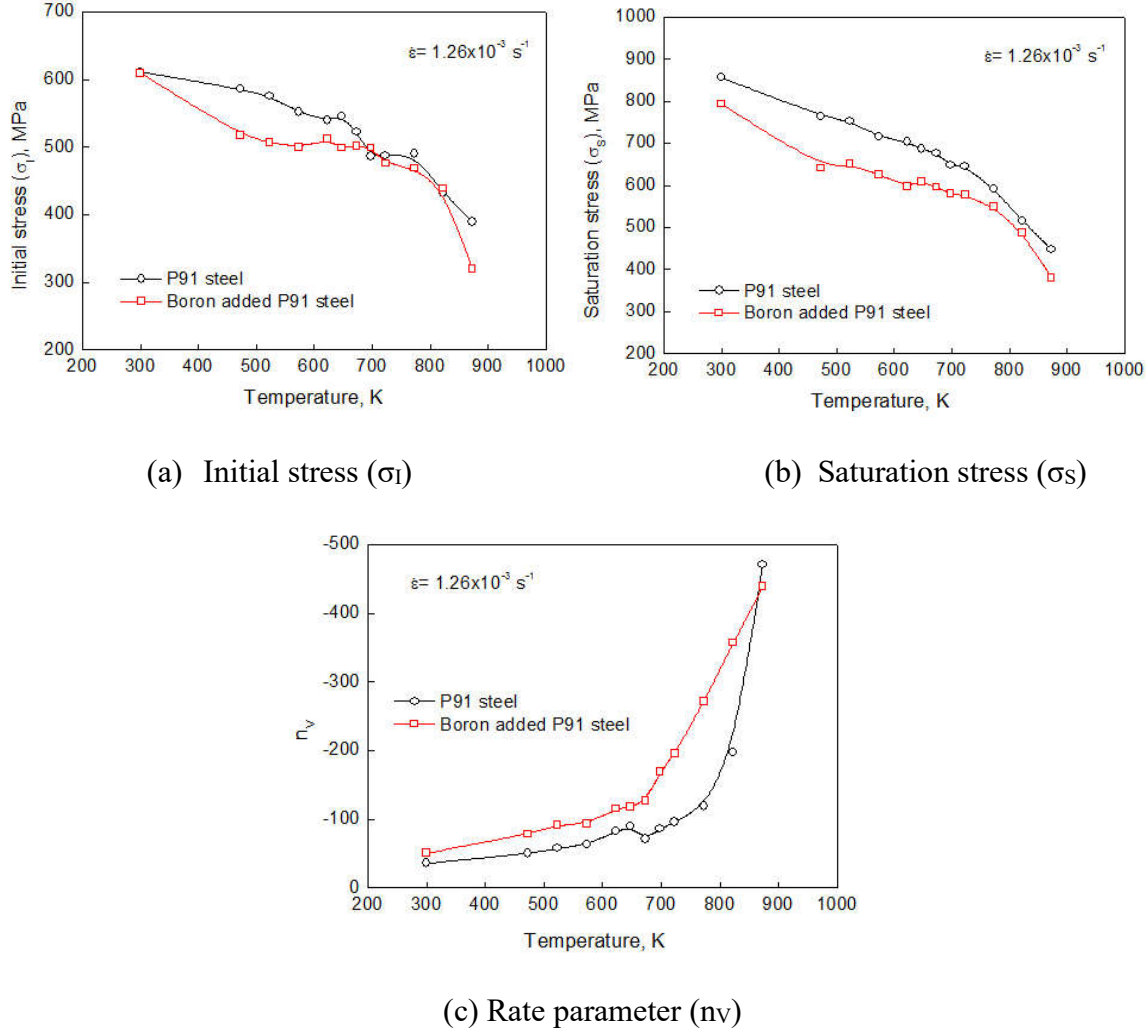


Fig. 5.6: The variations of Voce parameters (a) initial stress (σ_I) (b) saturation stress (σ_S) and (c) n_v with temperature for both boron added P91 steel and P91 steel

From the higher n_v value for boron added P91 steel, it can be discernible that the enhanced dynamic recovery was expected for the steel compared to that P91 steel. The reduce weight and volume fraction of MX precipitates as well as coarser hierarchical boundaries resulting in higher dynamic recovery for boron added P91 steel than the P91 steel. Since the indirect

interrelationship exists between n_v and uniform plastic strain [54], the lower uniform plastic strain was expected for boron added P91 steel compared to P91 steel as shown in Fig. 5.7.

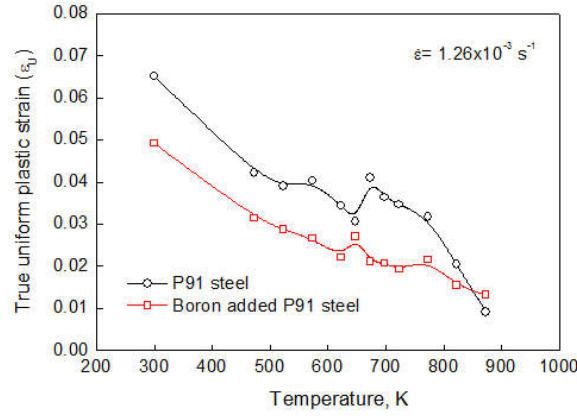



Fig. 5.7: The variations of true uniform plastic with temperature for both boron added P91 steel and P91 steel at the strain rate $1.26 \times 10^{-3} \text{ s}^{-1}$

Softened microstructure of boron added P91 steel is also responsible for the observed low values in the strength values such as YS, UTS, K_1 , $\exp(K_2)$, σ_I and σ_S . In recent studies by C. R. Das et al [96, 97] concluded that uniform yield and tensile strengths along with ductility of boron added P91 steel as function of peak simulated heat treatment temperatures has insensitive to the simulated heat treatments as compared to P91 steel. Accordingly in the present investigation revealed that the tensile and work hardening properties of boron added P91 steel are more sensitive to initial heat treatment conditions (Normalizing and Tempering). The normalizing treatment has more detrimental effect in reducing the properties of boron added P91 steel than tempering treatment. The comparative evaluation of boron added P91 steel and P91 steel concluded that the heat treatment effects on tensile properties in the literature [96, 97] and present study is closely comparable. It is also important to mention that the prolonged normalizing temperature leads to reduction on tensile and work hardening properties of boron added P91 steel. In contrast the duration of tempering temperature is found have nominal influence on tensile properties.


Annexure I

CERTIFICATION ON ACADEMIC INTEGRITY

1. I D PRASADARAO PALAPARTI (name of the student) HBNI Enrolment No. ENGGO2201505017 hereby undertake that, the Thesis titled "TENSILE PROPERTIES AND WORK HARDENING BEHAVIOUR OF BORON ADDED PSI STEEL" (***bold & italics***) is prepared by me and is the original work undertaken by me and free of any plagiarism. That the document has been duly checked through a plagiarism detection tool and the document is plagiarism free.
2. I am aware and undertake that if plagiarism is detected in my thesis at any stage in future, suitable penalty will be imposed as per the applicable guidelines of the Institute / UGC.

 29.07.2019
Signature of the Student
(with date)

Endorsed by the Thesis Supervisor: ✓
(I certify that the work done by the Researcher is plagiarism free)


29/7/2019
Signature (with date)

Name: V. S. SRINIVASAN
Designation: SO / G
Department/ Centre: RMG, IGCAR
Name of the CI/ OCC IGCAR

SYNOPSIS

Boron added P91 steel (P91B) is considered to be futuristic candidate structural material for Commercial Liquid Metal Fast Breeder Reactor (CLMFBR) Steam Generator (SG) applications. Boron is an important interstitial element, having extremely low solubility in α -solid solution ($<0.003\%$). In general, boron addition to heat treatable low carbon steels improves its hardenability, strength and subsequently make the steels less susceptible to quench cracking and distortion during conventional as well as post heat treatment conditions. The beneficial effect of boron addition to the 9% Cr steels is to reduce the coarsening kinetics of $M_{23}C_6$ carbides by enrichment of boron in carbides. This in turn is reported to improve the creep rupture properties and type-IV crack resistance in weld-joints.

Tensile stress-strain and work hardening analysis for engineering materials attract continued scientific and technological interest in understanding deformation and work hardening behaviour of materials for high temperature applications in order to ensure the safe performance of material in working environment. In the present investigation, tensile flow and work hardening behaviour of boron added P91 steel is examined in normalized and tempered condition. Tensile tests were carried out at different temperatures ranging from 300 to 873 K employing three different strain rates of 1.26×10^{-3} , 3.16×10^{-4} and $3.16 \times 10^{-5} \text{ s}^{-1}$. The microstructure and fracture surface examination were carried out by using Optical and Scanning Electron Microscopy (SEM) for all tested samples. The microstructure of as-received samples consists of transformed tempered lath martensite with high dislocation density along with distribution of fine precipitates on lath, packet and prior austenite grain boundaries. The fracture surface of tensile tested specimens showed typical cup and cone fracture with significant shear lip in peripheral region followed by appearance of fibrous surface fracture at the center of the fractured specimens. The width of the shear lip and the size of central fibrous area decreased with increase the test temperature. The overall fracture

appearance showed ductile fracture from surface followed by brittle fibrous nature at the center of samples.

The variation of true stress and true plastic strain behaviour as function of temperature and strain rate was discussed. It was observed that the true stress and true plastic strain decreased with increase in temperature. The decrease in stress and strain values is nominal at room (300 K) temperature and more rapid at high temperature (698–873 K). At intermediate temperature regime (473–698 K) the variations in true stress–strain behaviour is insignificant and data has been appeared to be a narrow band. The variation of shear modulus normalized yield strength and ultimate tensile strength with temperature exhibited a decrease in strength with increase the temperature. The decrease in strength is gradual between 300–473 K, followed by peaks/plateau at intermediate temperature (473–698 K), and sudden decrease at high temperature (698–873 K) for all the strain rates. Strain rate dependence yield and ultimate strengths revealed insignificant influence at room temperature (300 K). However, with decrease in strain rate, strength was varied at intermediate temperature regime followed by rapid decrease at high temperature regime. The variation of percentage total elongation with temperature showed gradual decrease from 300 to 473 K, followed by ductility minima at 473–698 K, and rapid increase at high temperatures (723–873 K). The influence of strain rate on percentage total elongation was totally insignificant for all temperature and strain rate conditions. The variation in percentage reduction in area with temperature exhibited insignificant variations at room (300 K), followed by appearance of peaks/plateau at intermediate temperature regime (473–698 K) and rapid increase at temperature regime (723–873 K). The strength parameters such as yield and ultimate tensile strength related to boron added P91 steel was compared with international test data such as, NIMS, and French design code RCC–MR average data. The boron added P91 steel data exhibited reasonably better yield and ultimate tensile strengths than the NIMS and French design code RCC–MR average data.

Constitutive material modeling is carried out on experimental stress–strain data for understanding the tensile deformation and work hardening behaviour of boron added P91 steel by using various tensile flow relationships. The Ludwigson and Voce equations were exclusively used for this study to describe the true stress–true plastic strain data for all test conditions. The variation of experimental true stress as a function of true plastic strain at different temperature and strain rates exhibited a decrease in true stress with increase in temperature from 300 to 473 K, followed by a marginal decrease in the intermediate temperature regime (473–698 K). Further at this temperature range the flow stress data appeared in the form of band of narrow region. At high temperatures a rapid decrease in flow stress is observed. It is also clearly indicated that the level of true plastic strain that the specimens can be deformed uniformly, decreased with increase in temperature. Uniform plastic strain also decreased from temperature 300 to 473 K followed by a marginal decrease at intermediate regime (473–698 K) and a rapid decrease at high temperatures (>698 K). All these observations strongly indicated that the variation of true stress with true plastic strain demonstrated three distinct temperature regimes of room, intermediate and high. At room and intermediate temperatures, the experimental data exhibited curvilinear behaviour and nearly linear behaviour at high strain and temperatures. The experimental true stress–true plastic strain data was fitted with tensile flow relationships proposed by Ludwigson and Voce using Levenberg–Marquardt (L–M) algorithm with unknown constants as adjustable parameters. The goodness of fit was evaluated using lower χ^2 value, i.e., the sum of square of the deviations of the calculated stress values from the experimental stress values obtained for these relationships at different strain rate and temperature conditions. The variations of instantaneous work hardening rate (θ) with true stress (σ) displayed two stage behaviour characterized by initial transition stage (stage–I) followed by stage–III. The θ – σ plots exhibited rapid decrease of stress in transition stage (stage–I) and gradual decrease in stage–III regime. The stress to onset of stage–III, which is determined as a stress for the transition from stage–I to stage–III, when plotted as a function of temperature, exhibited gradual

decrease from room to intermediate followed by rapid decrease at high temperature. The variations of Ludwigson derived work hardening parameters (K_1 , n_1 , K_2 , n_2) with temperature exhibited a gradual decrease from room temperature followed by peaks/plateau at intermediate and rapid decrease at high temperatures. The description of true stress and true plastic strain data by using Voce equation that usually results in improved predictions is another attractive flow relationship. Voce equation has provided significant attention in view of sound interpretation proposed by the Kocks–Mecking.

In this investigation, a detailed analysis has also been performed to study the work hardening behaviour of boron added P91 steel in the framework of Kocks–Mecking approach and subsequently studied the equivalence between Kocks–Mecking and Voce relationships. Analysis indicated that flow behaviour of boron added P91 steel can be adequately described by both Voce and Kocks–Mecking approaches at all the test conditions. The parameters associated with both approaches displayed three distinct temperature regimes as gradual variations from 300 to 473 K followed by peaks/plateaus at intermediate temperature and rapid variations at high temperature. The observed narrow band regions in true stress–true strain data and θ vs. σ , $\theta\sigma$ vs. σ behaviour, peaks/plateau, ductility minima, and negative strain rate sensitivity in tensile properties, work hardening parameters pertaining to Ludwigson, Voce, and Kocks–Mecking ascribed to anomalous behaviour. The observed anomalous variation in flow behaviour at intermediate temperature is attributed to the occurrence of dynamic strain ageing (DSA). The dynamic strain ageing causes an increased rate of dislocation multiplication and delay in recovery of dislocation structure due to reduced propensity to cross–slip leading to uniform distribution of dislocations or poorly defined cell structure.

The activation energy for dynamic recovery is calculated using model proposed by Bergström and Hallén. The dynamic recovery is governed by cross–slip of screw dislocations at low and intermediate temperature, and dislocation climb dominates over cross–slip mechanism at

high temperatures. The average values of activation energy for cross-slip mechanism at room and intermediate temperature as $Q_c = 3.61 \text{ kJ mol}^{-1}$ ($37.5 \times 10^{-3} \text{ eV/atom}$) and for climb mechanism at high temperature as $Q_m = 182.4 \text{ kJ mol}^{-1}$ have been obtained. It can also be observed that the temperature at which transition take place from cross-slip dominated deformation to climb controlled deformation decreased with decrease in the strain rate. The comparison of respective work hardening parameters obtained using K-M approach and Voce equation indicated attractive equivalence between the two approaches for boron added P91 steel. Finally, in order to demonstrate the role of boron and its influence on mechanical properties and work hardening behaviour after alloying to plain P91 steel, a comparative results of tensile and work hardening parameters of boron added P91 steel and P91 steel have been presented for further scope of understanding.